DESIGN AND APPLICATION OF NOVEL MEMBRANE MATERIALS

Thesis by

Orland Bateman

In Partial Fulfillment of the Requirements for
the degree of
Doctor of Philosophy

CALIFORNIA INSTITUTE OF TECHNOLOGY
Pasadena, California

2022
(Defended September 8, 2021)

Orland C. L. Bateman
ORCID: 0000-0002-6985-494X

ACKNOWLEDGEMENTS

As my time at Caltech comes to a close, I admit that I have been looking forward to taking a moment to recognize those who have participated in this journey with me. I am fan of the quote "If you want to go fast, go alone. If you want to go far, go together." I know that much of what I have accomplished, and all of this thesis, was only possible because of the contributions of others. Above all, I thank God for giving me opportunities to work with so many amazing people.

To begin, I would like to thank my advisors. Professor Kornfield was always fond of saying "When you have two advisors telling you to go in opposite directions, you just need to go orthogonal to them both and you'll find something interesting." I thank Professor Kornfield for helping me develop a more analytical mindset, connecting me with scientists around the world, and giving me opportunities to be involved in many different aspects of research. Professor Diallo, thank you for introducing me to the wonderful world of membrane technology. I appreciated the times we were able to discuss new ideas and only regret that we did not have time to pursue them.

I am very grateful to the many other mentors I have had during my time as a student here. Professor Faber, thank you for your listening ear and timely advice on both my academics and career. Professor Brady, thank you for pushing me to continue improving and helping me view my research in different ways. Professor Wang, thank you for helping me develop a better understanding of theory. Professor Vicic, I immensely enjoyed the times I was your TA. You taught me a great deal about science, effective teaching, and adaptability. Doctor Ford, thank you for teaching me about membranes and showing me the ropes in lab. Also, thank you for the fun times at beamtimes, those will definitely be treasured memories.

For the funding that made my thesis research possible, I express my gratitude to: The National Science Foundation (NSF), Joseph J. Jacobs Institute for Molecular Engineering for Medicine, Rothenberg Innovation Initiative, Kanel Scholarship, and Dow Chemical Company. I also express my gratitude to the research facilities I used throughout my research including: Argonne National Laboratory and the Molecular Materials Resource Center of the Beckman Institute.

To the undergraduate students I had the opportunity to work with: Jon Cotler, Amritpal Singh, Forrest & Riley Ramirez, and Julian Peres. I have learned so much from each of you and I am grateful to you for helping me become a better teacher and mentor.

To the other members of the Kornfield lab: thank you for your patience with me and my eccentricities. I'm also very grateful for the willing feedback you have given me over the many presentations and research queries we have weathered.

To my good friend Doctor Noriaki Arai, it was a pleasure to work with you while you were here and I hope we may work together again in the future. You have helped me raise my vision of what is possible. To my good friend Johnny Berjikian, thank you for all the ramen and kbbq visits as well as convincing me to see it through to the end.

To my wonderful parents and my four dedicated sisters. Thank you for a lifetime of help. I know I would not be the man I am today without your persistent love and guidance. Thank you for taking those late night vent calls and taking the time to ask about my work.

Lastly, a big thank you to my wife and sons. Thank you for letting me work the necessary late nights and early mornings as well as reading all those terribly long and dry scientific documents I wrote. It has been a journey to get here for sure, but you three have been a consistent source of happiness and cute pictures.

ABSTRACT

Membrane technology is uniquely suited to meet the growing need for more sustainable processes due to membranes' tailorable selectivity and energy efficiency. Efforts to further improve membrane performance and modify them for new applications have found success in academic studies with a versatile class of membranes known as mixed-matrix membranes (MMM). Mixed-matrix membranes combine the strength and controlled morphology of semicrystalline polymeric membranes with superior functionality of a separate material dispersed in the polymer matrix. The strength and toughness of the resulting membranes depends on polymer morphology, including degree of crystallinity and pore structure. Control of the membrane morphology is achieved by kinetically trapping a partially phase separated state, for example, using Nonsolvent Induced Phase Separation (NIPS) to drive liquid-liquid and solid-liquid demixing. However, the processes used to control the polymer morphology are influenced by the functional particles and can result in novel morphologies. In Chapter 2, we used a promising strategy for stably incorporating functional polymeric particles in a structural polymer matrix to investigate the role of the particles during NIPS. The interplay of functional polymeric particle loading and nonsolvent induced phase separation are examined using x-ray diffraction (to deduce the crystal morph adopted by polyvinylidene difluoride, PVDF) and scanning electron microscopy (to observe membrane morphology and the size and distribution of functional particles). We found that the interaction between nonsolvent and functional particles enables a shift in crystal phase usually not attainable with our solvent.

In addition to studying the fundamentals underlying MMM formation, we investigated two applications for novel membrane materials: purification of therapeutic antibodies and size-selective particle capture. Purification of proteins for medical use requires several chromatographic steps in order to produce solutions of sufficient purity. For many years, the gold standard in the field was resin-based packed bed chromatography; however, more recently membrane chromatography has gained prevalence due to its faster processing time, lower cost, and low operating pressure. With these advantages come the drawbacks of low binding capacity and a sensitivity to the concentration of salt ions in the

solution. To address these two drawbacks, we investigated the chromatographic abilities of a modified MMM, in Chapter 3, and a novel membrane material comprising an MMM-ceramic composite, in Chapter 4. We discovered that the performance of the modified MMM is dependent on crosslinker chemistry and crosslink density. Upon optimization, the modified membrane demonstrated a binding capacity consistent with the upper range of available literature values as well as reduced sensitivity to salt. In addition, the development of the novel MMM-ceramic composite enables the use of a broader range of polymer matrix compositions for membrane chromatography.

Capture of pathogens from complex fluids, such as blood, has received substantial attention due to rising rates of sepsis and antibiotic resistance. In Chapter 5, we pursued the capture of pathogens from model fluids using the size-based separation capabilities of dendritic ceramic membranes. We found that interactions between the ceramic surface and the suspended particles played a significant role in membrane performance.

TABLE OF CONTENTS

LIST OF FIGURES

LIST OF TABLES

Chapter 1

MEMBRANE DESIGN AND APPLICATION - BACKGROUND

1 Introduction

This thesis work focuses on three topics: the interplay between nonsolvent and membrane composition during phase inversion (Chapter 2), the application of mixed-matrix materials to membrane chromatography (Chapters 3&4), and size-based capture of bacteria from complex solutions using dendritic ceramic membranes (Chapter 5).

1.1 Introduction to membrane technology

Membranes are semi-permeable barriers between two phases that allow selective transport from one phase to the other. The inherent selectivity of membranes allows them to perform separations more energy efficiently than competing methods. The improved energy efficiency and tailorable selectivity have facilitated the use of membranes in several fields including water purification[1–4], bioseparations[5–7], catalysis[8,9], and resource recovery[10,11]. The mechanism of selectivity stems from both the membrane's physical structure and its chemical composition.

The morphology of a membrane may be classified as being either symmetric (homogeneous) or asymmetric (heterogeneous)[12]. Symmetric morphologies are further differentiated as porous or dense structures; wherein the mechanisms for mass transfer are pore-flow and solution-diffusion for porous and dense membranes respectively. Asymmetric membranes are characterized by having a dense skin layer supported by a porous sublayer and therefore demonstrate a mixture of pore-flow and solution-diffusion mass transfer. If the skin layer and porous support are not fabricated from the same material, the membrane is considered a composite[13]. Figure 1.1 shows the range of size-based separations that is compatible with the different mechanisms of mass transfer highlighted for each membrane morphology. As the mass transfer transitions from pore-flow to solution-diffusion, the size

of particles that are able to permeate the membrane decreases. In addition to the influence of the membrane structure, selectivity is also impacted by membrane composition including any additional functionalization of the base material.

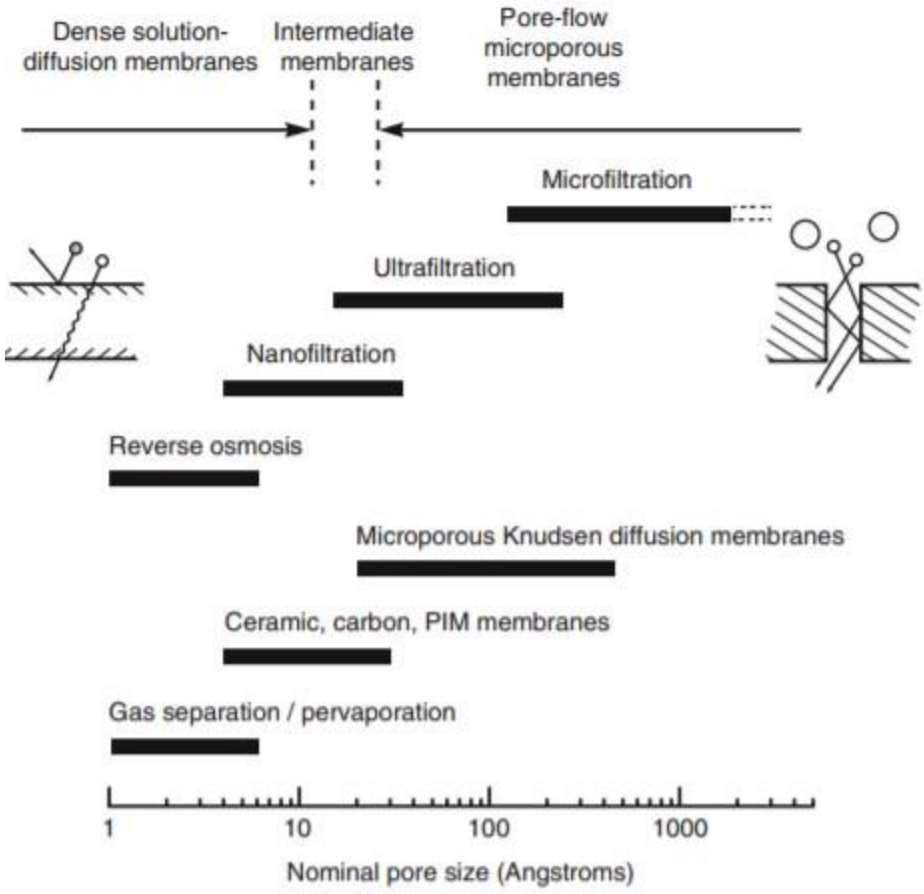

Figure 1.1: Illustration of different membrane regimes and corresponding transport (solution-diffusion and pore-flow)[13]

Membranes may be fabricated using either biological or synthetic materials, with the latter covering both inorganic and organic compounds[12,13]. Of particular interest to the work presented in this thesis are polymeric and ceramic membranes; both materials have been used as membranes in several fields and have corresponding advantages and drawbacks. Considering first the benefits of polymeric membranes: First, literature has demonstrated how to easily fabricate both symmetric and asymmetric membranes with a range of size selectivity from a polymer solution using a method known as Nonsolvent Induced Phase Separation (NIPS)[14–16]. Second, there have been over 100 different types of polymers tested

as membrane materials and of those several have been demonstrated to have – among polymers – great chemical and thermal resistance as well as good mechanical strength. These materials include poly(vinylidene Fluoride) (PVDF), polysulfone (PS), polytetrafluoroethylene (PTFE), polyethylene (PE), polypropylene (PP), and polyimide (PI)[12,17]. Third, several polymeric membranes are amenable to further surface functionalization to tailor properties such as hydrophilicity, surface charge, and fouling resistance[12,18–20]. Fourth, the fabrication of membranes from polymer dope solutions facilitates the inclusion of functional 'additives' that are used to influence morphology[3,18]. Consider next the drawbacks associated with polymeric membranes: First, polymeric membranes used in separation processes frequently suffer from a build-up of unwanted material on the membrane surface through a process known as fouling[19,21]. As the build-up thickness increases the filtration process suffers a decrease in the permeate flux, which eventually requires cleaning of the membrane surface through backwashing or chemical treatments. Second, they are easily degraded in solutions that contain a good solvent for the polymer as well as many cleaning solutions[17]. For example, membranes fabricated using PVDF have been demonstrated to lose mechanical integrity after treatment in caustic or amine rich solutions. Third, polymeric membranes have a lower maximum operating temperature than equivalent inorganic materials[12].

A noteworthy subclass of polymeric membranes known as mixed-matrix membranes (MMM) are identified by the incorporation of functional materials into the matrix of the structural polymer. The inclusion of functional materials has facilitated improved performance in several fields including water purification[3,19], gas separations[22], and resource recovery[10,11]. Figure 1.2 displays two common methods used to incorporate the functional particles into the polymer matrix. The first route adds preformed particles to the dope solution and uses a variety of methods to achieve a homogeneous distribution prior to casting the membrane. However, the methods used to encourage mixing are frequently detrimental to the structural polymer and are often not successful in evenly distributing the functional polymeric particles[23]. In the case when the resulting membrane does have functional particles dispersed throughout, these particles are only bound to the polymer matrix through physical

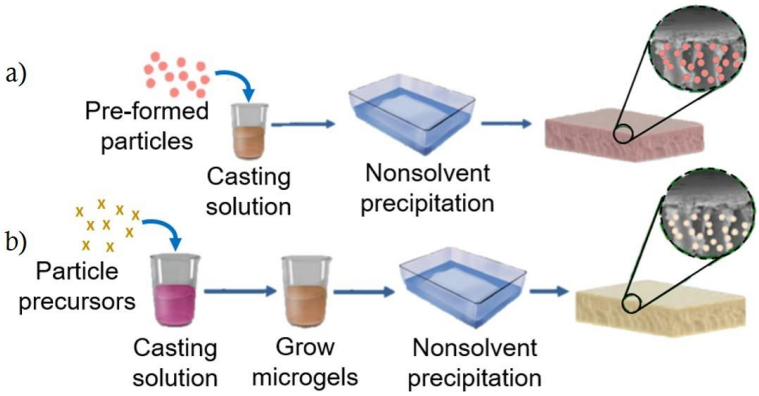

Figure 1.2: Routes to form mixed-matrix membranes using a) preformed particles and b) in situ generated functional particles[23] (Reproduced with permission.)

interactions. As a result, the pre-formed functional particles tend to leach out over time leading to a decrease in membrane performance. The route displayed in Figure 1.2b is an alternative designed to avoid the drawbacks associated with the direct addition of pre-formed particles. By generating the functional particles *in situ,* the particles will be both more evenly distributed and more tightly incorporated into the polymer matrix. Furthermore, a method pioneered by Diallo and coworkers demonstrated the successful inclusion of *in situ* generated polymeric functional particles into a MMM. Although mixed-matrix membranes provide several benefits in the form of improved performance and novel applications, they still share the drawbacks of sensitivity to tough cleaning solutions and lower operating temperatures with the neat polymer membranes[23].

Ceramic membranes are in many ways a natural counter to polymeric membranes. Consider the advantages of ceramic membranes: First, ceramic membranes have demonstrated a lower propensity to fouling in water purification and bioseparations. Second, they exhibit excellent chemical resistivity and retention of mechanical integrity in a variety of extreme environments such as caustic, bleach, and concentrated acidic solutions[24,25]. Third, they are compatible with operations at temperatures over 200 ºC, a temperature range in which most polymeric membranes would be in the melt state[12]. Fourth, there are well documented methods to further functionalize the ceramic surfaces as required[26]. The following are considered the key drawbacks to ceramic membranes: First, they are significantly more expensive – anywhere from 3 to 5 times – to produce than polymeric

membranes[12]. Second, it is more difficult to obtain an asymmetric ceramic structure with a dense selective layer than it is to form an asymmetric polymer membrane. This drawback is somewhat mitigated by the use of ceramic membranes as the support for an asymmetric composite. Third, the selection of additives that may be incorporated into the ceramic structure is limited by the harsh processing conditions used during fabrication. Ceramic and polymeric membranes have different advantages that tailor their capabilities towards different applications.

1.2 Nonsolvent Induced Phase Separation – Literature review

1.2.1 Brief history of synthetic membranes

The first synthetic membrane was fabricated using nitrocellulose by Adolph Fick in 1855[27]. The introduction of cellulose based synthetic membranes provided a level of reproducibility that was unobtainable with animal-based membranes. The field was further advanced by Bechhold in 1907, who introduced a method to control pore size and measure pore diameters as well as coining the term 'ultrafiltration'. By the 1940s commercial cellulose membranes were used to determine the safety of drinking water as well as the removal of contaminants in research applications. Over the next couple of decades, several additional polymers were tested, but the applications of synthetic membranes were limited due to difficulty in fabrication and low fluxes. Then, in 1963 Sourirajan and Loeb published their discovery of 'immersion precipitation' – a novel precipitation method that produced defect free asymmetric membranes[17]. The unique morphology of the asymmetric membrane enabled both high selectivity and high flux. The selectivity stems from the dense skin layer, while the porous sublayer facilitates higher fluxes by reducing the mass transfer resistance across the majority of the membrane. Following the Loeb-Sourirajan discovery, the field of membrane technology underwent a revolution and grew rapidly through the 1980s. In the 1970s there was a transition from cellulose based membranes to a composite membrane comprised of polysulfone and polyamide, which demonstrated better thermal and chemical resistance. Since the 1970s, there has been extensive literature research done on 'immersion

precipitation' with a variety of different polymers[27]. This thesis will focus on systems that use PVDF as the structural polymer.

1.2.2 Overview of NIPS mechanism

Phase inversion is the process of solidifying a homogeneous liquid polymer solution under controlled conditions. There are several methods to induce the phase separation

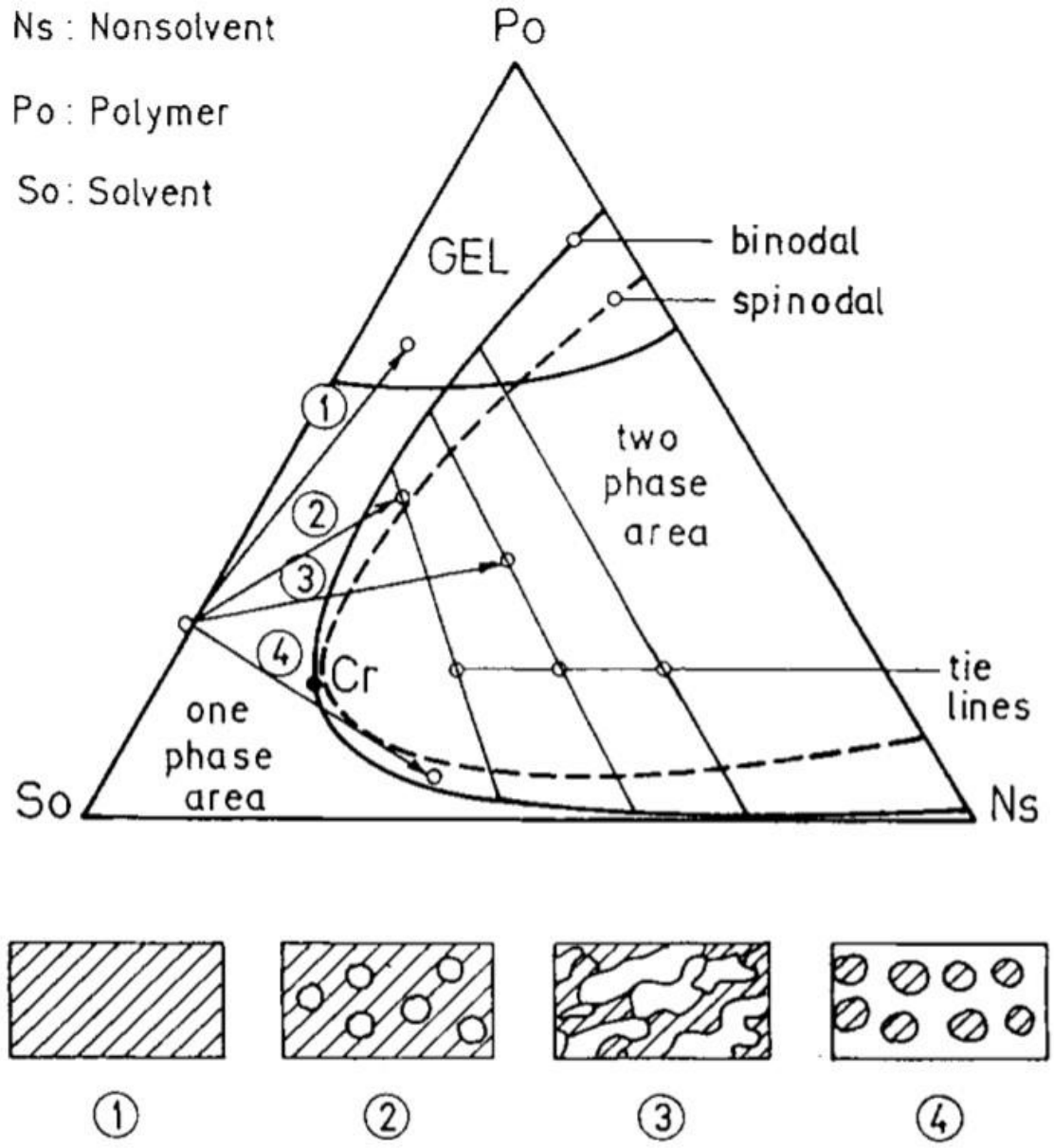

Figure 1.3: Ternary phase diagram representing the states in during nonsolvent induced phase separation for a Polymer/Solvent/Nonsolvent system[28] (Reproduced with permission).

leading to polymer solidification including nonsolvent induced phase separation (NIPS), thermally induced phase separation (TIPS), polymerization induced phase separation (PIPS), and vapor induced phase separation (VIPS). NIPS and its derivatives are the most commonly used methods in the literature and commercially.

The NIPS process begins when the homogeneous liquid polymer solution is immersed in a liquid that is incompatible with the polymer, known as a nonsolvent. As the solvent and nonsolvent interdiffuse, the composition of the casting solution changes and depending upon the rates of mass transfer follows one of the 4 routes shown in Figure 1.3[28]. Along the four routes there are two types of demixing processes to consider: liquid-liquid demixing – wherein the ternary solution starts as a homogeneous solution in the one phase area and then crosses the binodal into an unstable regime that induces phase separation into two liquid phases, and solid-liquid demixing – wherein a ternary solution in either the one phase or two phase area cross into the gel region producing a solid polymer crystal phase in equilibrium with a liquid polymer-lean phase[17]. In other words, in liquid-liquid demixing the solution phase separates as a liquid and then the polymer-rich region solidifies and crystallizes. In solid-liquid demixing the polymer crystallization and solidification drives phase separation and as a result is a slower process that is seen mostly in semi-crystalline polymers such as PVDF.

In route 1, the rate of solvent leaving the dope solution is faster than the rate of nonsolvent entering. This imbalance in fluxes results in the polymer concentration increasing until it surpasses the gelation concentration. Once the ternary system has entered the gelation concentration regime the polymer undergoes solid-liquid demixing and solidifies via gelation and/or crystallization into a dense and compact structure[12].

In route 2, the interdiffusion of solvent and nonsolvent produces a ternary solution that is in a metastable region in-between the spinodal and binodal lines. In the metastable region concentration fluctuations lead to the nucleation and growth of the polymer-lean phase via liquid-liquid demixing. If the growth of the polymer-lean phase reaches the point of phase coalescence (the droplets of polymer-lean phase begin coalescing) the resulting membrane

will have an open-cellular morphology. When the growth is interrupted by solidification of the polymer-rich matrix before reaching domain coalescence the resulting membrane will have a closed-cell morphology[12].

For route 3, the interdiffusion of solvent and nonsolvent results in a ternary solution that passes the metastable region and enters the two phase region. Upon reaching the two phase region, even small concentration fluctuations motivate the solution to separate via spinodal decomposition into two continuous phases with concentrations determined by the tie-lines depicted in Figure 1.3. The spinodal decomposition is very fast and so the final morphology is determined by the competition between phase coalescence of polymer solidification. Therefore, rapid solidification results in a membrane with high pore interconnectivity being produced; whereas, slower solidification of the polymer-rich phase produces a membrane analogous to a nucleation and growth mechanism.

Route 4 has several similarities with route 2 in that the ternary solution enters a metastable region and growing concentration fluctuations leads to the formation of nuclei and growth. However, in the case of route 4, the nonsolvent diffuses into the membrane faster than solvent leaves resulting in a decreasing polymer concentration. As the ternary solution moves into the metastable region, liquid-liquid demixing motivates the nucleation and growth of the polymer-rich, thereby producing a nodular morphology consisting of loosely connected polymer aggregates.

The brief explanation above provides an introduction to the thermodynamics behind NIPS, but it is important to note that different sections across the thickness of the casting solution are at different points on the ternary phase diagram[17]. For example, while the top surface of the casting solution may already be undergoing spinodal decomposition, the middle of the polymer solution may just be reaching the binodal line, with the bottom layer still being comfortably in the one phase region. The path to phase separation of the lower sections in the polymer solution will be influenced by the changes in solvent and nonsolvent mass transfer arising from the phase separation and polymer solidification higher up in the membrane[14]. As a result, the driving forces behind phase separation at the nonsolvent-dope

solution interface and the bottom of the membrane could be completely different; indeed, this is the very phenomenon that gives rise to asymmetric membranes.

1.2.3 Effect of nonsolvent

As shown in Figure 1.4a, using different nonsolvents shifts the placement of the binodal line in the ternary phase diagram. The placement of the binodal line correlates to the time required for the nonsolvent to diffuse and reach a high enough concentration to induce

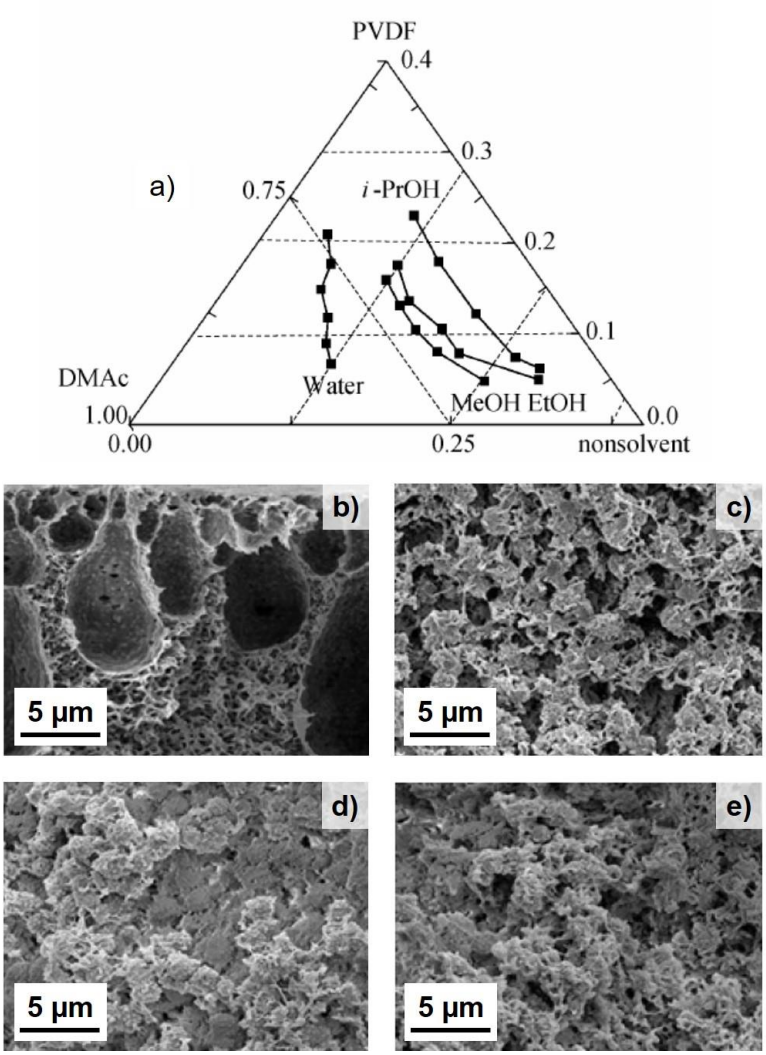

Figure 1.4: The a) ternary phase diagram for DMAc/PVDF/nonsolvent with corresponding cross-sectional SEM micrographs for nonsolvent of b) water, c) methanol, d) ethanol, and e) isopropanol. Modified from reference 15.

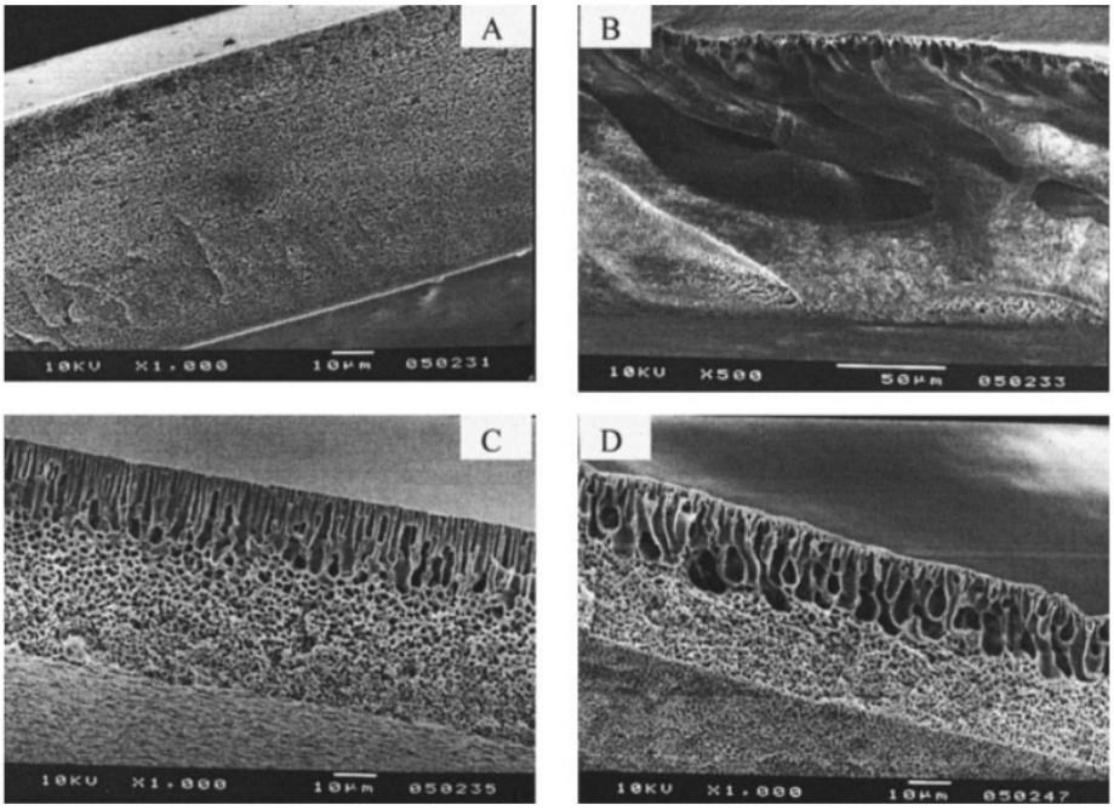

Figure 1.5: SEM micrographs of the cross-sections of membranes cast from a polymer dope solution containing 15 wt.% PVDF in a) TEP, b) NMP, c) DMF, d) DMAc[29] (Reproduced with permission).

phase separation. Nonsolvents with binodal lines that are closer to the left side of the diagram, such as water in Figure 1.4a, are known as hard nonsolvents because they are not tolerated by the casting solution resulting in instantaneous demixing of the ternary solution[15]. The speed of the phase separation favors liquid-liquid demixing, which leads to the formation of asymmetric membranes. The morphology of the porous sublayer changes depending on the solvent used. Bottino et al. published an excellent study on the role of different solvents in determining membrane morphology when using water as the nonsolvent[14]. They reported a good correlation between solvent-nonsolvent mutual diffusivity and membrane morphology. Figure 1.5 presents the different morphologies obtained from polymer solutions of four common solvents for PVDF[29]. Of particular interest to the work presented in this thesis, was the behavior of membranes prepared using Triethyl phosphate (TEP). The TEP-water mutual diffusivity is low, producing asymmetric membranes with sponge-like layers that do not contain macorvoids[14].

Nonsolvents with binodal lines towards the right of the phase diagram (such as ethanol and isopropanol in Figure 1.4a) are known as soft nonsolvents because they require a higher concentration to induce phase separation. The system requires a longer diffusion time to reach the necessary concentrations to induce phase separation resulting in delayed demixing of the ternary solution. The delay in demixing has several critical impacts on membrane structure[15]. First, the slower demixing at the surface changes the dynamics of skin layer formation. For example, when membranes are cast in reaction grade isopropanol or ethanol the skin layer formation is completely disrupted producing a symmetric membrane with a surface morphology consistent with the bulk structure. Second, the longer time required to initiate phase separation increases the contribution of solid-liquid demixing, thereby suppressing the formation of macrovoids and producing a sponge-like structure. Both of these effects are influenced by the 'softness' of the nonsolvent. Nonsolvent 'softness' may be tailored by making either water-soft nonsolvent or water-solvent mixtures. Sukitpaneenit et al. investigated the changes in membrane structure and performance when prepared using nonsolvents comprising mixtures of water and ethanol[30]. As the ethanol concentration increased, the formation of the skin layer was disrupted and the bulk membrane structure transitioned from fingerlike pores and macrovoids to a globular sponge-like morphology (Fig. 1.6)[30].

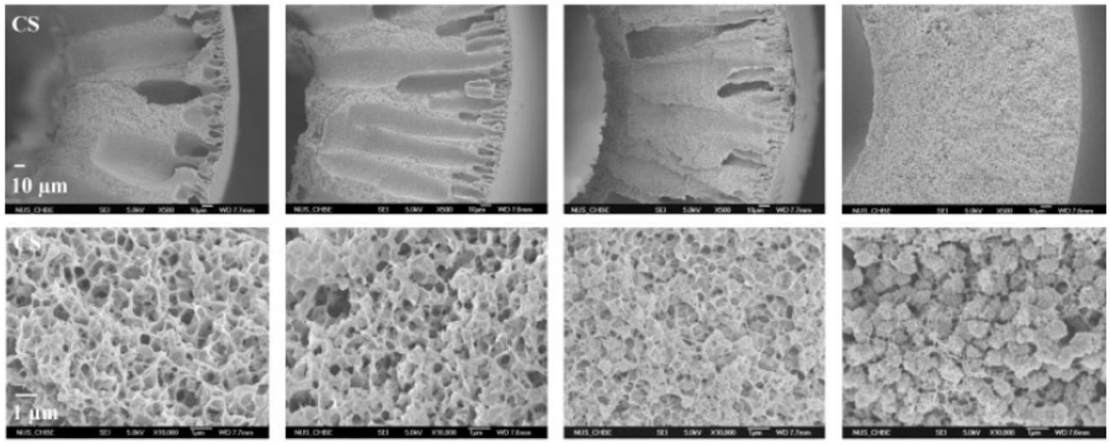

Figure 1.6: Cross-sectional SEM micrographs of PVDF membranes prepared using the indicated nonsolvent. Bottom row micrographs are higher magnification images of top row (Reproduced with permission)[30].

1.2.4 Effect of additives

Up to this point the NIPS process has only been considered in the context of a polymer solution comprising a single polymer dissolved in a solvent. However, one of the focuses of this work is to determine how *in situ* generated functional microparticles interact with the other components of the polymer solution and nonsolvent to influence membrane morphology. This section summarizes the current literature on incorporating different additives into PVDF casting solutions and their influence on membrane structure. These additives fall within 3 categories: low molecular weight (MW) compounds including inorganic salts and small molecules, high molecular weight polymers, and inorganic particles.

Membranes prepared using additives in the first category are not considered MMMs because the low MW compounds are not incorporated into the polymer matrix, but rather diffuse into the nonsolvent bath upon casting. Although they do not contribute to the long term functionality of the membrane, these compounds have been demonstrated to facilitate distinctive changes to membrane morphology and performance. For example, work by Bottino et al. demonstrated that inclusion of low concentrations of lithium chloride (LiCl) into the dope solution produced a more porous polymer structure with larger cavities[31]. As the concentrations of LiCl are increased, macrovoid formation is suppressed and the support layer becomes more sponge-like. The change in morphology was attributed to a higher rate of polymer precipitation driven by the casting solution being less thermodynamically stable and LiCl mixing with water[18,31]. Another common low MW additive studied by Yeow et al. is lithium perchlorate ($LiClO_4$), which at concentrations of 1% - 3% increase the mean pore size and narrow the pore size distribution. However, they demonstrated that increasing the concentration of $LiClO_4$ above 3% lead to the formation of macrovoids when using N,N-Dimethylacetamide as solvent[32]. They concluded that the changes in morphology rose from a reduction in nonsolvent tolerance upon the addition of the salt leading to faster phase separation. In addition to the ionic additives, several small molecules have also been used as

pore forming additives. One such example is glycerol, which was shown by Shih et al. to increase the mean pore size of PVDF membranes with increasing concentration[33].

The influence of additives in the second category changes both with polymer chemistry and molecular weight. Typically, the higher MW polymers are trapped in the membrane during phase inversion, while the lower MW polymers are able to diffuse out. The entrapment of the higher MW polymers influences the flux of nonsolvent into the membrane, thereby changing the morphology. Wang et al. demonstrated this phenomenon by comparing membranes prepared using the same concentrations of polyvinyl pyrrolidone (PVP) at molecular weights of 10 kg/mol and 340 kg/mol[34]. The higher molecular weight PVP produced a membrane with a thicker skin layer and larger pores. The thicker skin layer was ascribed to the entrapped hydrophilic PVP polymers facilitating faster diffusion of water into the casting solution. They also investigated the influence of different concentrations of low MW PVP in the range of 2% and 5%, but did not observe a noticeable change in morphology.

The MMMs produced using inorganic functional particles have been demonstrated to improve performance with minimal changes to the physical structure of the membrane[24,35–37]. Work reported by Cao et al. added <2 wt.% TiO_2 nanoparticles to the casting solution. The resulting mixed-matrix membrane demonstrated an improved water flux and fouling resistance, with a minor change in pore size determined by the size of the TiO_2 nanoparticle[37]. Another study demonstrated the incorporation of silica particles into the casting solution, which increased the viscosity of the casting solution enabling the formation of membranes with lower polymer concentrations. Membranes prepared using silica demonstrated comparable water flux and improved retention of Dextran 40k, with no significant changes in membrane morphology reported[35]. In an investigation conducted by Yan et al., MMMs were fabricated through the inclusion of nano-sized alumina (Al_2O_3) particles. Membranes with a concentration of 2 wt.% alumina particles showed improvements to both fouling resistance and tensile strength with no observable changes to membrane morphology or pore size.

Although the work discussed in the preceding paragraph focuses on several different types of particles, all of them are at low particle loadings (≤ 5 wt.%) and only use water as the nonsolvent. At these particle loadings there are negligible changes to the membrane structure due to the low concentration of functional particles having a minimal impact on the interactions of the NIPS process.

1.3 Membrane chromatography

Chromatographic materials are distinguished by their separation chemistries, which belong to one of three classes: affinity, ion-exchange (IEX), and hydrophobic interaction & reverse phase (HI & RP). This work will focus on IEX chromatography, which is further divided into cation exchange (CEX) and anion exchange (AEX) chromatography. The binding behavior of IEX materials are characterized using a variety of well documented model proteins including: bovine serum albumin (BSA), lysozyme, myoglobin, ovalbumin, and conalbumin[5].

1.3.1 Resin and membrane protein chromatography

Prior to the late 1990s, the gold standard in high-resolution protein separation and analysis was resin-based packed beds[5]. Although packed beds demonstrate excellent selectivity, they also suffer from a few major limitations that make scale-up of chromatographic processes challenging. First, packed beds rely on diffusive mass transport to bring the solute in contact with the binding sites within the resin pores as seen in Figure 1.7a. Transport via diffusion is quite slow and necessitates longer processing times to fully use the bed's binding capabilities. Second, the pressure drop across packed beds is frequently high and often increases during operation as the functional media deforms and induces bed consolidation[38]. Third, defects in the packing of the bed – such as cracking – produce flow passages that lead to channeling of the material flow resulting in poor bed utilization. Some research has been done to investigate the use of rigid, monodisperse, nonporous media in packed beds to address the drawbacks identified here[5]. Although the newer media does

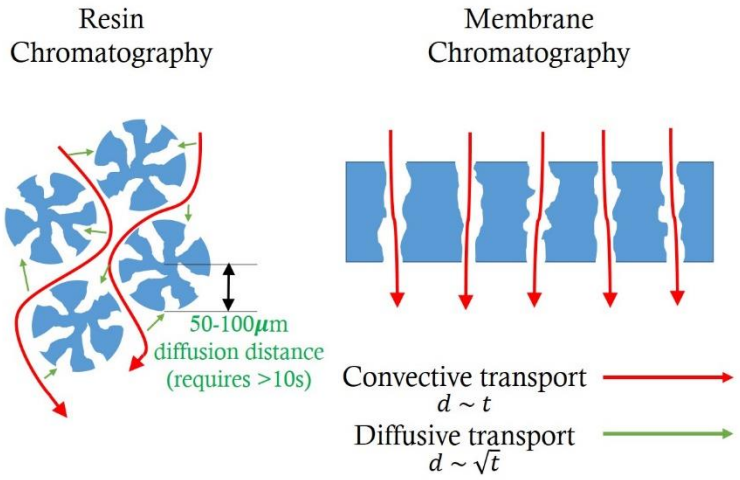

Figure 1.7: Illustration comparing mass transport mechanisms between packed beds (resins) and membrane chromatography.

resolve several of the limitations of packed beds, it retains the high pressure drop across the column while also showing a reduction in protein binding capacity[39].

The leading method to circumvent the limitations outlined above is the use of microporous membranes as the base of the chromatographic material[5,7,38,40]. Membrane-based chromatography relies primarily on convective mass transport, Figure 1.7b, to convey molecules of interest to available binding sites. The reliance on convection enables faster processing time and decouples operating flow rate and binding capacity. The use of microporous membranes also reduces the pressure drop across the column as the total membrane volume may be spread out over a large area with a small thickness – while still maintaining uniform fluid flow. Membrane adsorbers also have the added advantage of frequently being faster and cheaper to produce. Although the use of microporous membranes in protein separations have addressed the limitations of packed beds, they have also introduced a new set of drawbacks related to binding capacity. Due to the fluid flow being restricted to the pores of the membrane, the only surfaces available to interact with the solutes are the pore walls. The limited surface area leads to a reduction in the binding capacity, similar to what was seen when using nonporous media in packed beds[5,39]. Membrane-based chromatography was also shown to lose its binding efficacy at lower salt concentrations in comparison to resin-based systems. Sections 1.3.2 and 1.3.3 summarize the advances in

membrane chromatography related to increasing binding capacity and improving salt tolerance respectively.

1.3.2 Efforts to increase binding capacity

Recent work on improving the binding capacity of membrane chromatography materials has focused on overcoming the limited pore surface area through functionalization of the porous support with polymer chains, polymer electrolytes, or polymer brushes[41–43]. The added polymers extend into the protein solution and enable the formation of a 3-dimensional 'scaffold' that facilitates protein adsorption, thereby increasing the binding capacity of the membrane[7]. To further increase the density of available binding sites requires tailoring of the various functionalization methods to maximize the density of available binding sites. For example, a study by Bhut et al. functionalized the surface of regenerated cellulose membranes using surface-initiated atom transfer radical polymerization (ATRP) of 2-(dimethylamino)ethyl methacrylate (DMAEMA). The density and MW of the resulting poly(DMAEMA) chains were controlled independently using the initiator grafting density and polymerization time respectively[7]. The binding behavior of the functionalized membranes was investigated using BSA. They demonstrated that, at short polymerization times and low initiator grafting densities, the modified membranes had low binding capacities (~20 mg/mL). As the polymerization time and/or the initiator grafting densities increased, the static binding capacities increased as well until reaching a plateau at ~140 mg/mL. Furthermore, surface initiated ATRP has been shown to be a versatile method that is effective in functionalizing porous ceramic membranes in work by Sun et al. The resulting affinity chromatography membrane was reported to have a static BSA binding capacity of 150 mg/mL[40].

Surface initiated graft copolymerization, a derivative of UV-initiated graft copolymerization, is an alternative method used by Ulbricht and coworkers to functionalize the pore surface of polypropylene membranes for protein bining[41]. They used benzophenone (BP) as the initiator and acrylic acid (AA) as the functional monomer and investigated copolymerization with acryl amide (AAm). The resulting CEX membranes were

characterized using lysozyme as the model protein. The highest dynamic lysozyme binding of 20 mg/mL was observed in the membrane with the highest grafting density of acrylic acid.

In addition to the standard polymerization techniques discussed above, there have been other methods developed to improve the functionality of the pore surface. Work by Nova et al. reported the development of a chitosan/ceramic hybrid membrane for affinity chromatography[42]. The hybrid was fabricated by deposition of chitosan onto a ceramic support followed by a crosslinking reaction to immobilize the chitosan layer. The chitosan was then further functionalized with iminodiacetic acid, a carboxylic ligand that binds Cu^{2+}. The hybrid demonstrated a BSA binding capacity more than double that of the ceramic support alone. Liu et al. investigated the fabrication of IEX membranes using layer-by-layer deposition of polyelectrolytes onto a porous regenerated cellulose support[43]. They reported an increase from 11 mg/mL to 16 mg/mL in the dynamic lysozyme binding capacity as the number of polyelectrolyte layers was increased from 3 to 7. They also noted that using polyelectrolyte layers led to a higher permeability than commercially available membranes.

1.3.3 Efforts to improve salt tolerance

The ligands used in IEX chromatography are often classified into strong and weak ion exchangers. A strong IEX has the same charge over the 0-14 pH range, with strong anion exchangers (such as quaternary amines) being positively charged and strong cation exchangers (such as sulfonates and sulfopropyls) being negatively charged. In contrast, weak ion exchangers are pH dependent and only demonstrate optimal performance over a small pH range. Weak anion exchangers (such as primary and secondary amines) begin to lose their ionization above a pH of 9, while weak cation exchangers (such as carboxymethyl) perform poorly below a pH of 6.

For many years, strong ion exchangers were the recommended functional groups for both resin and membrane chromatography because their electrostatic charges were not dependent on pH. However, one of the consistent shortcomings of strong IEX chemistries was their sensitivity to salt in the protein solution. This limitation was illustrated in a study

by Fischer-Frühholz and coworkers, which revealed that adding 150 mM of NaCl reduced the binding capacity of a strong AEX membrane by 90%[44]. The sharp drop in binding capacity in the presence of salt motivated the inclusion of costly buffer exchange steps in commercial protein separations. Removing the buffer exchange steps would require a membrane that demonstrated consistent binding capacities across a range of solution conductivities. In the same study, Fischer-Frühholz and coworkers demonstrated that using a weak anion exchange ligand comprising mostly primary amines on the same porous support enabled consistent binding at both 0 mM and 150 mM added NaCl corresponding to conductivities of 1.8 mS/cm and 16.8 mS/cm respectively[44].

Work by Riordan et al. screened several ligands as alternatives to quaternary amines in strong AEX membranes[45]. They reported four ligands that demonstrated better salt tolerance than the quaternary amine ligand they used as a control. They concluded that ligand performance was determined by three factors: the ligand density of the membrane, the net charge of the ligand molecule, and the molecular structure of the ligand with an emphasis on the presence of available hydrogens. The third factor was shown to be critical in achieving high salt tolerance by testing derivatives of the four ligands that replaced the hydrogens on primary amines with methyl groups. The derivatives had a reduced salt tolerance, with the extent of the reduction depending on the number of primary amine hydrogens that were replaced. It was determined that primary and, to a lesser extent, secondary amines are able to interact with the solutes using both electrostatic interactions and hydrogen bonding; whereas, both quaternary and tertiary amines are only able to interact via electrostatic interactions[45]. Therefore, as the concentration of salt goes up, the electrostatic interactions are screened leading to poor binding capacities of quaternary and tertiary amines. In contrast, the primary and secondary amines are still able to effectively bind proteins through hydrogen bonding over a range of salt concentrations.

1.4 Size-based separations

1.4.1 Size based separation membranes

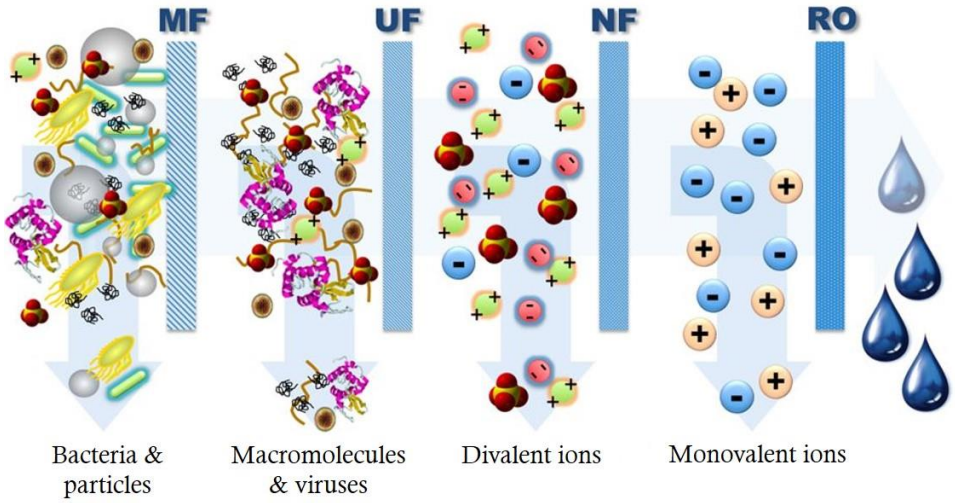

Figure 1.8: Illustration depicting the rejection capabilities of microfiltration (MF), ultrafiltration (UF), nanofiltration (NF), and reverse osmosis (RO)[46]

A classic example of size separation using membrane technology is water purification, as demonstrated in Figure 1.8. Membrane materials in the microfiltration (MF), ultrafiltration (UF), and nanofiltration (NF) regimes operate at least partially on a basis of rejecting particles that are too large to pass through the membrane pores[46]. However, one of the major drawbacks of size separations using membrane technology is fouling, the process of unwanted material building up on the membrane surface[23]. Fouling reduces membrane performance and can even lead to membrane failure if not treated properly. Furthermore, fouling becomes an increasingly difficult problem to address as the solution being separated becomes more complex. While much of the prior literature in membrane science focuses on designing membranes with improved anti-fouling capabilities[21,23,47,48], recent work in microfluidics has revealed several techniques to avoid fouling altogether and still achieve high efficiency size based separation[49–51].

1.4.2 Size based separations using inertial microfluidics

Although microfluidic devices are not membranes, they are discussed here due to the relevance of their applications in size based separations in complex fluids. In a review article by Professor Di Carlo, he summarizes two effects of inertial microfluidics that may be used in size based separations[51]. The first is secondary flows (also called Dean flow or dean

vortices) in curved channels which arise from a velocity mismatch between fluid in the center and near-wall regions in the downstream direction. Due to the velocity difference, the fluid elements near the channel centerline have greater inertia than the fluid near the walls and tend to flow outward. The outward movement creates a pressure gradient in the radial direction of the curved channel. However, the channel is enclosed and so the fluid near the walls is re-circulated inwards by the pressure gradient resulting in two symmetric vortices[51]. Work by Seo et al. demonstrated the efficacy of using Dean flow to separate particles from a mixture containing 10 µm and 6 µm particles into two outlet streams, with an over 80% efficiency for both particle sizes. When the experiment was repeated using a mixture of 10 µm and 3 µm particles, the 3 µm particles were evenly distributed between the two outlet streams indicating that this separation method is only effective for larger particles[52]. Another study by Warkiani et al. used dean vortices to isolate circulating tumor cells and achieved a capture efficiency of 80%, while significantly reducing the concentrations of unwanted cells (white blood cells).

The second effect discussed by Professor Di Carlo is inertial migration of particles, wherein particles in flow within a bounded channel experience a lift force from the fluid shear gradient as well as a lift force from the wall[51]. These forces move the particles across undisturbed streamlines until the particles reach an 'equilibrium' position where the two forces are equal. A study by Che et al. demonstrated selective capture of cancer cells using inertial migration of particles in a straight channel followed by the fluid flowing past a reservoir with vortices[53]. An imbalance between the wall lift and shear lift forces that scales with particle diameter led to the larger cancer cells being captured by the vortices while the smaller white and red blood cells are allowed to flow past. Their technique demonstrated a capture efficiency of 83% at a processing speed of 800 µL/min whole blood[53]. The formation of vortices by fluid flowing past a reservoir or cavity will be discussed further in the next section.

1.4.3 Vortices in confined cavities

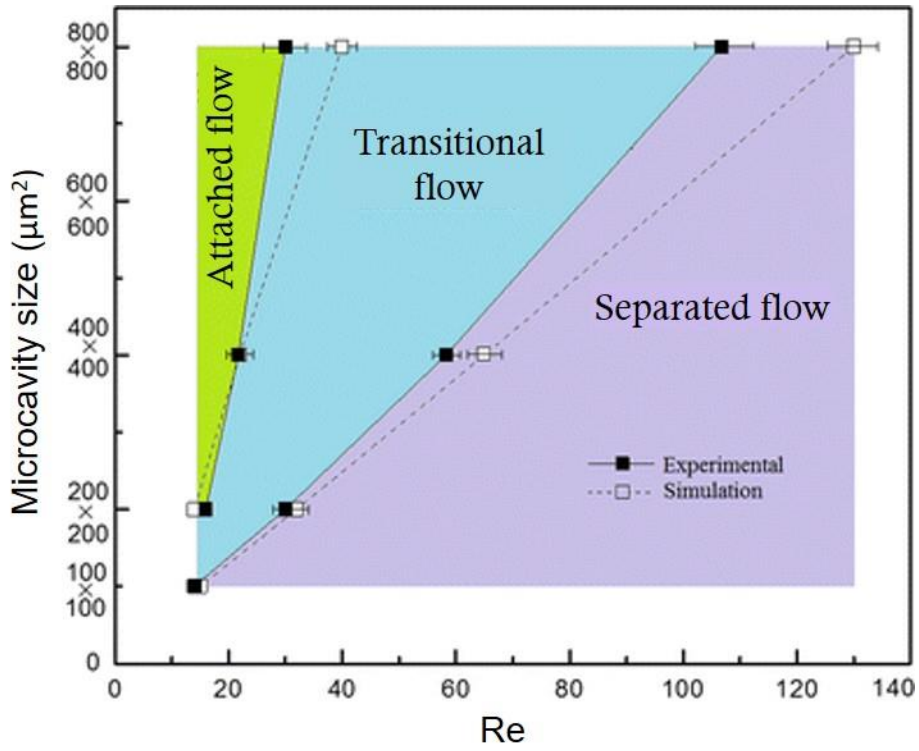

Figure 1.9: Flow regime map for different flow patterns based on Re and microcavity size[55].

Prior literature has shown that when a fluid flowing in a channel with finite inertia encounters a microcavity (a bounded volume with cross-sectional dimension larger than the channel) a region of recirculating flow may form dependent on the fluid inertia represented by the Reynolds number (Re)[54,55]. As seen in Figure 1.9, at very low Re the fluid is in a regime called attached flow where there is no recirculation in the microcavity. As Re increases, the fluid encounters a transitory regime where the recirculating flow is not fully formed. Once Re passes a critical value, determined by the dimensions of the cavity, the fluid

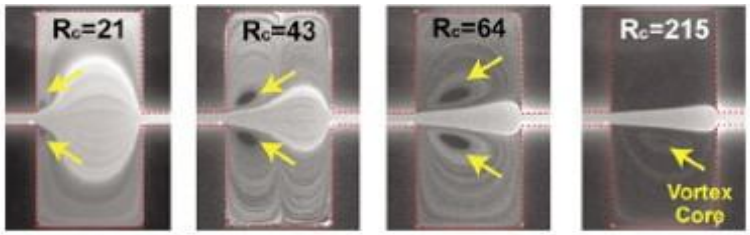

Figure 1.10: Fluorescent microscopic images using dilute fluorescent particles (d = 1 μm) to illustrate growth of the microvortices with increasing Re[56] (Reproduced with permission).

is in a separated flow regime and the microcavity shows signs of recirculating flow. As Re continues to increase the recirculating flow will eventually expand to fill the entire microcavity (Fig. 1.10)[56]. Microvortices have been shown to be a versatile and powerful tool in the literature[55] and it is important to understand the conditions required to form them in novel geometries, such as a dendritic ceramic membrane.

1.5 The purpose of this work

1.5.1 Influence of *in situ* generated microparticles and nonsolvent on membrane morphology

In the literature, investigation of the influence of incorporated functional materials on MMM structure has been limited to low particle concentrations and/or using water as the only nonsolvent[24,35–37]. Due to their low concentration in these studies, the functional particles have little influence on the phase inversion process as seen by the minimal changes to membrane structure. However, the low concentrations are necessary to avoid particle aggregation during casting and leaching during operation[37]. Similarly, if a softer nonsolvent than water was used, the functional materials would not be as tightly entrapped within the polymer matrix leading to leaching and loss of membrane functionality. In chapter 2, we use a promising strategy for stably incorporating functional polymer particles in a structural polymer matrix to investigate a wider range of functional particle loadings (6 wt.% - 60 wt.%). Furthermore, with the functional particles being stably incorporated into the polymer matrix we are able to use different nonsolvents to help unravel the interactions between the solvent, structural polymer, functional particles, and nonsolvent that govern phase separation and subsequent membrane morphology.

1.5.2 Mixed-matrix membrane chromatography

Prior to this work, the majority of published studies improved binding capacity by adding functional polymers to the porous support surface[7,40,41]. An alternative method that has received limited attention is to incorporate materials with IEX capabilities into mixed-

matrix membranes[57]. Using mixed-matrix membranes with *in situ* generated functional particles provides several advantages over pore surface functionalization including: maintaining polymer matrix integrity, even distribution of functional material, and inherent 3-dimensional binding of proteins. Furthermore, the functional material may be tailored to include a higher concentration of primary and secondary amines, thereby improving the salt tolerance of the resulting mixed-matrix membrane adsorber[44,45]. In this thesis we investigate the design and fabrication of novel AEX membrane adsorbers through modifying MMMs (chapter 3) and developing ceramic-MMM composites (chapter 4).

1.5.3 Size based isolation of bacteria using dendritic ceramics

The rapid isolation and detection of pathogens from blood has received increased attention in the literature over the past two decades due to rising rates of sepsis and antibiotic resistance[56,58,59]. In recent years, the speed of pathogen detection and identification has been improved by several advances in digital quantitative detection[60,61]. In regards to isolation of pathogens from complex fluids, prior literature has demonstrated a variety of microfluidic based techniques for size based separation of pathogens[52,56,58,59]. However, many of these techniques operate at low flow rates and have limited scalability. Thus, the field is still in need of a fast and scalable method to isolate and then concentrate pathogens prior to detection. In chapter 5, we examine the capture efficiency of dendritic freeze-cast ceramic membranes using model particle suspensions and *E. coli* suspended in BSA solutions.

References

(1) Geise, G. M.; Lee, H.-S.; Miller, D. J.; Freeman, B. D.; McGrath, J. E.; Paul, D. R. Water Purification by Membranes: The Role of Polymer Science. Journal of Polymer Science Part B: Polymer Physics 2010, 48 (15), 1685–1718. https://doi.org/10.1002/polb.22037.

(2) Geise, G. M.; Paul, D. R.; Freeman, B. D. Fundamental Water and Salt Transport Properties of Polymeric Materials. Progress in Polymer Science 2014, 39 (1), 1–42. https://doi.org/10.1016/j.progpolymsci.2013.07.001.

(3) Kotte, M. R.; Cho, M.; Diallo, M. S. A Facile Route to the Preparation of Mixed Matrix Polyvinylidene Fluoride Membranes with In-Situ Generated Polyethyleneimine Particles. Journal of Membrane Science 2014, 450, 93–102. https://doi.org/10.1016/j.memsci.2013.08.025.

(4) Werber, J. R.; Osuji, C. O.; Elimelech, M. Materials for Next-Generation Desalination and Water Purification Membranes. Nature Reviews Materials 2016, 1 (5), 1–15.

(5) Ghosh, R. Protein Separation Using Membrane Chromatography: Opportunities and Challenges. Journal of Chromatography A 2002, 952 (1), 13–27. https://doi.org/10.1016/S0021-9673(02)00057-2.

(6) Chen, G.; Umatheva, U.; Alforque, L.; Shirataki, H.; Ogawa, S.; Kato, C.; Ghosh, R. An Annular-Flow, Hollow-Fiber Membrane Chromatography Device for Fast, High-Resolution Protein Separation at Low Pressure. Journal of Membrane Science 2019, 590, 117305. https://doi.org/10.1016/j.memsci.2019.117305.

(7) Bhut, B. V.; Husson, S. M. Dramatic Performance Improvement of Weak Anion-Exchange Membranes for Chromatographic Bioseparations. Journal of Membrane Science 2009, 337 (1), 215–223. https://doi.org/10.1016/j.memsci.2009.03.046.

(8) Kotte, M. R.; Kuvarega, A. T.; Talapaneni, S. N.; Cho, M.; Coskun, A.; Diallo, M. S. A Facile and Scalable Route to the Preparation of Catalytic Membranes with in Situ Synthesized Supramolecular Dendrimer Particle Hosts for Pt(0) Nanoparticles Using a Low-Generation PAMAM Dendrimer (G1-NH 2) as Precursor. ACS Appl. Mater. Interfaces 2018, 10 (39), 33238–33251. https://doi.org/10.1021/acsami.8b11351.

(9) Ghosh, S. K.; Alam, Md. M.; Mandal, D. The in Situ Formation of Platinum Nanoparticles and Their Catalytic Role in Electroactive Phase Formation in Poly(Vinylidene Fluoride): A Simple Preparation of Multifunctional Poly(Vinylidene Fluoride) Films Doped with Platinum Nanoparticles. RSC Adv. 2014, 4 (79), 41886–41894. https://doi.org/10.1039/C4RA06334A.

(10) Kotte, M. R.; Kuvarega, A. T.; Cho, M.; Mamba, B. B.; Diallo, Mamadou. S. Mixed Matrix PVDF Membranes With in Situ Synthesized PAMAM Dendrimer-Like Particles: A New Class of Sorbents for Cu(II) Recovery from Aqueous Solutions by Ultrafiltration. Environ. Sci. Technol. 2015, 49 (16), 9431–9442. https://doi.org/10.1021/acs.est.5b01594.

(11) Park, M. J.; Nisola, G. M.; Vivas, E. L.; Limjuco, L. A.; Lawagon, C. P.; Seo, J. G.; Kim, H.; Shon, H. K.; Chung, W.-J. Mixed Matrix Nanofiber as a Flow-through Membrane Adsorber for Continuous Li+ Recovery from Seawater. Journal of Membrane Science 2016, 510, 141–154. https://doi.org/10.1016/j.memsci.2016.02.062.

(12) Abed, M.; Reza, M. Poly(Vinylidene Fluoride) (PVDF) Based Hydrophilic Hollow Fibre Membranes : Prospects for Wastewater Treatment. Ph.D., Imperial College London, 2012. https://doi.org/10.25560/9830.

(13) Baker, R. W. Membrane Technology and Applications, 3rd ed.; John Wiley & Sons: Chichester, West Sussex ; Hoboken, 2012.

(14) Bottino, A.; Camera-Roda, G.; Capannelli, G.; Munari, S. The Formation of Microporous Polyvinylidene Difluoride Membranes by Phase Separation. Journal of membrane science 1991, 57 (1), 1–20.

(15) Zuo, D.; Zhu, B.; Cao, J.; Xu, Y. Influence of Alcohol-Based Nonsolvents on the Formation and Morphology of PVDF Membranes in Phase Inversion Process. Chinese journal of polymer science 2006, 24 (03), 281–289.

(16) Jung, J. T.; Kim, J. F.; Wang, H. H.; di Nicolo, E.; Drioli, E.; Lee, Y. M. Understanding the Non-Solvent Induced Phase Separation (NIPS) Effect during the Fabrication of Microporous PVDF Membranes via Thermally Induced Phase Separation (TIPS). Journal of Membrane Science 2016, 514, 250–263. https://doi.org/10.1016/j.memsci.2016.04.069.

(17) Sun, C. Poly(Vinylidene Fluoride) Membranes: Preparation, Modification, Characterization and Applications. 2009.

(18) Liu, F.; Hashim, N. A.; Liu, Y.; Abed, M. R. M.; Li, K. Progress in the Production and Modification of PVDF Membranes. Journal of Membrane Science 2011, 375 (1), 1–27. https://doi.org/10.1016/j.memsci.2011.03.014.

(19) Farahani, M. H. D. A.; Vatanpour, V. A Comprehensive Study on the Performance and Antifouling Enhancement of the PVDF Mixed Matrix Membranes by Embedding Different Nanoparticulates: Clay, Functionalized Carbon Nanotube, SiO2 and TiO2. Separation and Purification Technology 2018, 197, 372–381. https://doi.org/10.1016/j.seppur.2018.01.031.

(20) Fontananova, E.; Bahattab, M. A.; Aljlil, S. A.; Alowairdy, M.; Rinaldi, G.; Vuono, D.; Nagy, J. B.; Drioli, E.; Di Profio, G. From Hydrophobic to Hydrophilic Polyvinylidenefluoride (PVDF) Membranes by Gaining New Insight into Material's Properties. RSC Advances 2015, 5 (69), 56219–56231.

(21) Mi, Y.-F.; Xu, G.; Guo, Y.-S.; Wu, B.; An, Q.-F. Development of Antifouling Nanofiltration Membrane with Zwitterionic Functionalized Monomer for Efficient Dye/Salt Selective Separation. Journal of Membrane Science 2020, 601, 117795. https://doi.org/10.1016/j.memsci.2019.117795.

(22) Aroon, M. A.; Ismail, A. F.; Matsuura, T.; Montazer-Rahmati, M. M. Performance Studies of Mixed Matrix Membranes for Gas Separation: A Review. Separation and Purification Technology 2010, 75 (3), 229–242. https://doi.org/10.1016/j.seppur.2010.08.023.

(23) Li, X.; Sotto, A.; Li, J.; Van der Bruggen, B. Progress and Perspectives for Synthesis of Sustainable Antifouling Composite Membranes Containing in Situ Generated Nanoparticles. Journal of Membrane Science 2017, 524, 502–528. https://doi.org/10.1016/j.memsci.2016.11.040.

(24) Yan, L.; Li, Y. S.; Xiang, C. B. Preparation of Poly(Vinylidene Fluoride)(Pvdf) Ultrafiltration Membrane Modified by Nano-Sized Alumina (Al2O3) and Its Antifouling Research. Polymer 2005, 46 (18), 7701–7706. https://doi.org/10.1016/j.polymer.2005.05.155.

(25) Sorarù, G. D.; Modena, S.; Guadagnino, E.; Colombo, P.; Egan, J.; Pantano, C. Chemical Durability of Silicon Oxycarbide Glasses. Journal of the American Ceramic Society 2002, 85 (6), 1529–1536. https://doi.org/10.1111/j.1151-2916.2002.tb00308.x.

(26) Acres, R. G.; Ellis, A. V.; Alvino, J.; Lenahan, C. E.; Khodakov, D. A.; Metha, G. F.; Andersson, G. G. Molecular Structure of 3-Aminopropyltriethoxysilane Layers Formed on Silanol-Terminated Silicon Surfaces. J. Phys. Chem. C 2012, 116 (10), 6289–6297. https://doi.org/10.1021/jp212056s.

(27) Smith, K. Development of Membrane Processes. In Membrane Processing; Tamime, A. Y., Ed.; Blackwell Publishing Ltd.: Oxford, UK, 2012; pp 1–16. https://doi.org/10.1002/9781118457009.ch1.

(28) Stropnik, C.; Germič, L.; Žerjal, B. Morphology Variety and Formation Mechanisms of Polymeric Membranes Prepared by Wet Phase Inversion. Journal of Applied Polymer Science 1996, 61 (10), 1821–1830. https://doi.org/10.1002/(SICI)1097-4628(19960906)61:10<1821::AID-APP24>3.0.CO;2-3.

(29) Yeow, M. L.; Liu, Y. T.; Li, K. Morphological Study of Poly(Vinylidene Fluoride) Asymmetric Membranes: Effects of the Solvent, Additive, and Dope Temperature. Journal of Applied Polymer Science 2004, 92 (3), 1782–1789. https://doi.org/10.1002/app.20141.

(30) Sukitpaneenit, P.; Chung, T.-S. Molecular Elucidation of Morphology and Mechanical Properties of PVDF Hollow Fiber Membranes from Aspects of Phase Inversion,

Crystallization and Rheology. Journal of Membrane Science 2009, 340 (1), 192–205. https://doi.org/10.1016/j.memsci.2009.05.029.

(31) Bottino, A.; Capannelli, G.; Munari, S.; Turturro, A. High Performance Ultrafiltration Membranes Cast from LiCl Doped Solutions. Desalination 1988, 68 (2), 167–177. https://doi.org/10.1016/0011-9164(88)80052-3.

(32) Yeow, M. L.; Liu, Y.; Li, K. Preparation of Porous PVDF Hollow Fibre Membrane via a Phase Inversion Method Using Lithium Perchlorate (LiClO4) as an Additive. Journal of Membrane Science 2005, 258 (1), 16–22. https://doi.org/10.1016/j.memsci.2005.01.015.

(33) Shih, H. C.; Yeh, Y. S.; Yasuda, H. Morphology of Microporous Poly(Vinylidene Fluoride) Membranes Studied by Gas Permeation and Scanning Electron Microscopy. Journal of Membrane Science 1990, 50 (3), 299–317. https://doi.org/10.1016/S0376-7388(00)80627-4.

(34) Wang, D.; Li, K.; Teo, W. K. Preparation and Characterization of Polyvinylidene Fluoride (PVDF) Hollow Fiber Membranes. Journal of Membrane Science 1999, 163 (2), 211–220. https://doi.org/10.1016/S0376-7388(99)00181-7.

(35) Bottino, A.; Capannelli, G.; D'Asti, V.; Piaggio, P. Preparation and Properties of Novel Organic–Inorganic Porous Membranes. Separation and Purification Technology 2001, 22–23, 269–275. https://doi.org/10.1016/S1383-5866(00)00127-1.

(36) Bottino, A.; Capannelli, G.; Comite, A. Preparation and Characterization of Novel Porous PVDF-ZrO2 Composite Membranes. Desalination 2002, 146 (1), 35–40. https://doi.org/10.1016/S0011-9164(02)00469-1.

(37) Cao, X.; Ma, J.; Shi, X.; Ren, Z. Effect of TiO2 Nanoparticle Size on the Performance of PVDF Membrane. Applied Surface Science 2006, 253 (4), 2003–2010. https://doi.org/10.1016/j.apsusc.2006.03.090.

(38) Bhut, B. V.; Wickramasinghe, S. R.; Husson, S. M. Preparation of High-Capacity, Weak Anion-Exchange Membranes for Protein Separations Using Surface-Initiated Atom Transfer Radical Polymerization. Journal of Membrane Science 2008, 325 (1), 176–183. https://doi.org/10.1016/j.memsci.2008.07.028.

(39) Hashimoto, T. Non-Porous Hydrophilic Resin-Based Packings for the Separation of Biopolymers. Journal of Chromatography A 1991, 544, 257–265. https://doi.org/10.1016/S0021-9673(01)83990-X.

(40) Sun, L.; Dai, J.; Baker, G. L.; Bruening, M. L. High-Capacity, Protein-Binding Membranes Based on Polymer Brushes Grown in Porous Substrates. Chem. Mater. 2006, 18 (17), 4033–4039. https://doi.org/10.1021/cm060554m.

(41) Ulbricht, M.; Yang, H. Porous Polypropylene Membranes with Different Carboxyl Polymer Brush Layers for Reversible Protein Binding via Surface-Initiated Graft Copolymerization. Chem. Mater. 2005, 17 (10), 2622–2631. https://doi.org/10.1021/cm0485714.

(42) Nova, C. J. M.; Paolucci-Jeanjean, D.; Belleville, M.-P.; Barboiu, M.; Rivallin, M.; Rios, G. Elaboration, Characterization and Study of a New Hybrid Chitosan/Ceramic Membrane for Affinity Membrane Chromatography. Journal of Membrane Science 2008, 321 (1), 81–89. https://doi.org/10.1016/j.memsci.2007.12.002.

(43) Liu, G.; Dotzauer, D. M.; Bruening, M. L. Ion-Exchange Membranes Prepared Using Layer-by-Layer Polyelectrolyte Deposition. Journal of Membrane Science 2010, 354 (1), 198–205. https://doi.org/10.1016/j.memsci.2010.02.047.

(44) Fischer-Frühholz, S.; Zhou, D.; Hirai, M. Sartobind STIC® Salt-Tolerant Membrane Chromatography. Nature Methods 2010, 7 (12), 12–13.

(45) Riordan, W.; Heilmann, S.; Brorson, K.; Seshadri, K.; He, Y.; Etzel, M. Design of Salt-Tolerant Membrane Adsorbers for Viral Clearance. Biotechnology and Bioengineering 2009, 103 (5), 920–929. https://doi.org/10.1002/bit.22314.

(46) Read "Water Reuse: Potential for Expanding the Nation's Water Supply Through Reuse of Municipal Wastewater" at NAP.Edu. https://doi.org/10.17226/13303.

(47) Akthakul, A.; Salinaro, R. F.; Mayes, A. M. Antifouling Polymer Membranes with Subnanometer Size Selectivity. Macromolecules 2004, 37 (20), 7663–7668. https://doi.org/10.1021/ma048837s.

(48) Su, Y. P.; Sim, L. N.; Li, X.; Coster, H. G. L.; Chong, T. H. Anti-Fouling Piezoelectric PVDF Membrane: Effect of Morphology on Dielectric and Piezoelectric Properties. Journal of Membrane Science 2021, 620, 118818. https://doi.org/10.1016/j.memsci.2020.118818.

(49) Ebrahimi Warkiani, M.; Guan, G.; Bee Luan, K.; Cheng Lee, W.; S. Bhagat, A. A.; Chaudhuri, P. K.; Shao-Weng Tan, D.; Teck Lim, W.; Chin Lee, S.; Y. Chen, P. C.; Teck Lim, C.; Han, J. Slanted Spiral Microfluidics for the Ultra-Fast, Label-Free Isolation of Circulating Tumor Cells. Lab on a Chip 2014, 14 (1), 128–137. https://doi.org/10.1039/C3LC50617G.

(50) Wu, Z.; Willing, B.; Bjerketorp, J.; K. Jansson, J.; Hjort, K. Soft Inertial Microfluidics for High Throughput Separation of Bacteria from Human Blood Cells. Lab on a Chip 2009, 9 (9), 1193–1199. https://doi.org/10.1039/B817611F.

(51) Carlo, D. D. Inertial Microfluidics. Lab on a Chip 2009, 9 (21), 3038–3046. https://doi.org/10.1039/B912547G.

(52) Seo, J.; Lean, M. H.; Kole, A. Membraneless Microseparation by Asymmetry in Curvilinear Laminar Flows. Journal of Chromatography A 2007, 1162 (2), 126–131. https://doi.org/10.1016/j.chroma.2007.05.110.

(53) Che, J.; Yu, V.; Dhar, M.; Renier, C.; Matsumoto, M.; Heirich, K.; Garon, E. B.; Goldman, J.; Rao, J.; Sledge, G. W.; Pegram, M. D.; Sheth, S.; Jeffrey, S. S.; Kulkarni, R. P.; Sollier, E.; Di Carlo, D. Classification of Large Circulating Tumor Cells Isolated with Ultra-High Throughput Microfluidic Vortex Technology. Oncotarget 2016, 7 (11), 12748–12760. https://doi.org/10.18632/oncotarget.7220.

(54) Khojah, R.; Lo, D.; Tang, F.; Di Carlo, D. The Evolution of Flow and Mass Transport in 3D Confined Cavities. arXiv:2101.07242 [physics] 2021.

(55) Shen, F.; Xu, M.; Zhou, B.; Wang, Z.; Liu, Z. Effects of Geometry Factors on Microvortices Evolution in Confined Square Microcavities. Microfluid Nanofluid 2018, 22 (4), 36. https://doi.org/10.1007/s10404-018-2056-2.

(56) Hur, S. C.; Mach, A. J.; Di Carlo, D. High-Throughput Size-Based Rare Cell Enrichment Using Microscale Vortices. Biomicrofluidics 2011, 5 (2), 022206. https://doi.org/10.1063/1.3576780.

(57) Avramescu, M.-E.; Borneman, Z.; Wessling, M. Mixed-Matrix Membrane Adsorbers for Protein Separation. Journal of Chromatography A 2003, 1006 (1), 171–183. https://doi.org/10.1016/S0021-9673(03)00562-4.

(58) Ohlsson, P.; Evander, M.; Petersson, K.; Mellhammar, L.; Lehmusvuori, A.; Karhunen, U.; Soikkeli, M.; Seppä, T.; Tuunainen, E.; Spangar, A.; von Lode, P.; Rantakokko-Jalava, K.;

Otto, G.; Scheding, S.; Soukka, T.; Wittfooth, S.; Laurell, T. Integrated Acoustic Separation, Enrichment, and Microchip Polymerase Chain Reaction Detection of Bacteria from Blood for Rapid Sepsis Diagnostics. Anal. Chem. 2016, 88 (19), 9403–9411. https://doi.org/10.1021/acs.analchem.6b00323.

(59) Faridi, M. A.; Ramachandraiah, H.; Banerjee, I.; Ardabili, S.; Zelenin, S.; Russom, A. Elasto-Inertial Microfluidics for Bacteria Separation from Whole Blood for Sepsis Diagnostics. J Nanobiotechnol 2017, 15 (1), 3. https://doi.org/10.1186/s12951-016-0235-4.

(60) Schoepp, N. G.; Khorosheva, E. M.; Schlappi, T. S.; Curtis, M. S.; Humphries, R. M.; Hindler, J. A.; Ismagilov, R. F. Digital Quantification of DNA Replication and Chromosome Segregation Enables Determination of Antimicrobial Susceptibility after Only 15 Minutes of Antibiotic Exposure. Angewandte Chemie International Edition 2016, 55 (33), 9557–9561. https://doi.org/10.1002/anie.201602763.

(61) Schlappi, T. S.; McCalla, S. E.; Schoepp, N. G.; Ismagilov, R. F. Flow-through Capture and in Situ Amplification Can Enable Rapid Detection of a Few Single Molecules of Nucleic Acids from Several Milliliters of Solution. Anal. Chem. 2016, 88 (15), 7647–7653. https://doi.org/10.1021/acs.analchem.6b01485.

Chapter 2

INFLUENCE OF NONSOLVENT AND MIXED-MATRIX COMPOSITION ON MEMBRANE MORPHOLOGY

The work presented in this chapter was done in collaboration with Andy Ylitalo and Tiziana Di Luccio. O. Bateman designed the systems for study, fabricated and characterized mixed-matrix membranes using SEM imaging and flux measurements. A. Ylitalo and T. Di Luccio performed the x-ray scattering measurements and assisted with initial analysis of the x-ray scattering patterns.

2.1 Introduction

Mixed-matrix membranes (MMM) are a versatile class of membranes that combine the structural and flow properties of polymeric membranes with the functionality of a separate material dispersed in the polymer matrix. The improved functionality enables MMMs in academic studies to surpass performance of neat polymeric membranes in several fields including gas separations[1–4], water purification[5–11], catalysis[12–14], and resource recovery[15–17]. One complication associated with this type of multicomponent membrane is the behavior of the functional particles when they are not properly incorporated into the polymer matrix. Insufficiently integrating the functional material into the polymer matrix frequently leads to an inhomogeneous distribution and in extreme cases complete expulsion of the particles from the membrane during processing. Various methods have been developed to resolve this issue for both *ex situ* and *in situ* generated functional particles providing several routes to a homogeneous distribution throughout the membrane[11,15,18].

To capitalize upon the benefits of MMMs, it is necessary to control and tailor membrane morphology to meet requirements of the end application[1,10]. For example, polyvinylidene fluoride (PVDF) is a commonly used polymer in many membrane applications due to its excellent chemical robustness, mechanical strength, and electrical properties[19]. The chemical robustness is an inherent property of PVDF and is therefore

consistent for any PVDF membrane that has not been chemically modified. In contrast, both the mechanical strength and piezoelectric character depend on the morphology of the membrane. In the case of mechanical strength, features such as macrovoids and fingerlike pores are detrimental to the membrane's mechanical properties. As a result, suppressing the formation of these features is an integral part of membrane fabrication for applications that operate at higher pressures such as water purification[18–20]. In other applications, the porosity of these features are beneficial and outweigh the detriment to the mechanical properties leading to the development of methods that promote their formation[21]. PVDF's piezoelectric character depends on both the microscopic morphology and the crystal phase, with the β-phase being electroactive and the α being electrically inert. To optimize the piezoelectric behavior, it is necessary to increase the concentration of β-phase PVDF and align the electrical dipoles across the membrane often done through a process known as poling. Whether it be to optimize mechanical strength or electrical performance, having the capability to tailor and control membrane morphology is essential.

Morphology control in polymeric membranes, including the degree of crystallinity, crystalline phase, and pore structure, is achieved by manipulating the kinetic trapping of a partially-phase separated state. For example, using different nonsolvents to drive liquid-liquid and solid-liquid demixing during Nonsolvent Induced Phase Separation (NIPS) enables the formation of distinct morphologies[5,22–25]. In MMMs the presence of the functional particles increases the complexity of the phase separation process by adding new interactions with the solvent, nonsolvent, and structural polymer[11,16].

Here, we use a method pioneered by Professor Diallo to stably incorporate functional polymer particles in a structural polymer matrix and investigate the role of the particles and nonsolvent chemistry during NIPS. The interplay of functional polymer particle loading and nonsolvent induced phase separation are examined using x-ray diffraction (to deduce the crystal phase adopted by polyvinylidene difluoride, PVDF) and scanning electron microscopy (to observe membrane morphology and the size and distribution of functional particles). We discover that the interaction between nonsolvent and functional particles

enables a shift in crystal phase and the formation of a unique morphology usually not attainable with our solvent.

2.2 Experimental methods

2.2.1 Materials

Polyvinylidene Fluoride (PVDF; Kynar 761, 400 kg/mol) was donated by Arkema. Hyperbranched polyethylenimine (PEI; 600 g/mol) was purchased from Polysciences. The following chemicals were purchased from Sigma Aldrich: Epichlorohydrin (ECH), Isopropanol (IPA), Triethyl phosphate (TEP), and N-methylpyrrolidone (NMP). Nonwoven PET support was purchased from Hollytex. All chemicals were used as received.

2.2.2 Membrane Synthesis

To begin a typical membrane synthesis, 5.91 g of PVDF was added to an empty 3-neck flask. The flask was then outfitted with an overhead mechanical stirrer and the necessary greased connectors. Next, 30 mL of TEP was added to the flask and then the remaining openings were sealed using rubber septa. The PVDF/TEP mixture was heated to 80 ºC for an hour with no mixing before the mixing speed was set to 60 rpm. The resulting solution was mixed overnight at 60 rpm and 80 ºC. During the heating of the PVDF/TEP mixture, the PEI/TEP solution was prepared by adding the desired mass of PEI (Table 2.1) to a scintillation vial followed by 5 mL of TEP. The mixture was vortexed until the solution was homogeneous and clear, and then it was left to equilibrate overnight at room temperature.

Once the solutions were equilibrated, the flask was purged with N_2 for 7 minutes, and the mixing speed was increased to 250 rpm. With the N_2 flow still on, the PEI solution was added dropwise to the flask using a glass Pasteur pipette over the course of 4 minutes. The resulting solution was left to mix for 5 minutes before adding 17 drops of concentrated HCl (37% solution), after which the solution turned cloudy. Following the addition of the HCl, the flask was incubated for 15 minutes at 80 ºC with the mixing speed maintained at 250

rpm. The required amount of ECH (Table 2.1) was then added to the flask, the N_2 flow was turned off, and the polymerization reaction was allowed to proceed for 4 hours.

Table 2.1: Membrane formulation for different PEI loadings

Formulation	PVDF (g)	PEI (g)	TEP (mL)	ECH (mL)
Neat	5.66	-	30	-
06	5.91	0.26	35	0.14
21	5.91	1.1	35	0.60
38	5.91	2.6	35	1.4
48	5.91	3.9	35	2.1
54	5.91	5.0	35	2.7
60	5.91	6.5	35	3.5

After the 4-hour reaction time, the flask was put under in-house vacuum for 10 minutes to remove entrapped gas. The dope solution was then cast either on glass to prepare samples for structural characterization (SEM and x-ray scattering) or on a nonwoven PET support for transport measurements. The mixture was spread uniformly using a doctor blade with a blade height of 300 µm. The cast mixture was left at room temperature for 30 seconds before immersion into a coagulation bath at room temperature. The coagulation bath comprised one of the following: distilled water, Isopropanol, or 50 v% N-methylpyrrolidone solution in water (abbreviated as NMP:H_2O here after). After two hours, the solidified membranes were moved to distilled water baths prior to storage in distilled water.

2.2.3 SEM characterization

The membrane top surface and cross-section were imaged using a Field Emission Scanning Electron Microscope (FE SEM – Zeiss 1550 VP). In preparation for imaging, the membrane samples were first dried at room temperature for 24 hours. Next, the samples were dried under house vacuum for 24 hours. To prepare the cross-section view, the chosen samples were immersed in liquid nitrogen for 2 minutes and then fractured. All samples were then coated with a Pt/Pd conductive layer on the surface of interest prior to imaging. The resulting micrographs were used to characterize sample morphology and, for cross-sections, estimate sample thickness. Mean particle size and particle size distribution of each condition was then determined by measuring the diameter of 100 particles in the cross-section images.

2.2.4 X-ray scattering

X-ray scattering measurements were performed at beamline 5-ID-D of the Advanced Photon Source at Argonne National Laboratory. The beamline collects both wide-angle x-ray scattering (WAXS) and small-angle x-ray scattering (SAXS) patterns simultaneously. The optimum exposure time for the samples scanned being 0.5 s and 0.005s, respectively. The membrane samples were cut into coupons approximately 10mm x 10mm and mounted onto a backing board in preparation for the measurements, five point on each sample. The first measurement near the center of the sample, and the next four at points on a circle of radius 2.5 mm about the center in 90º increments, moving clockwise. Background scans as empty sample openings were taken at regular intervals.

2.2.5 Water flux measurements

Samples for flux measurements were prepared by cutting a 45 mm x 90 mm rectangular coupon from a membrane cast on the nonwoven PET support. The samples were then loaded into a cross-flow filtration chamber with an active area of 18.75 cm^2. The membranes were conditioned for 90 minutes at a pressure of 3 bar and a cross-flow rate of 1.7 L/min using distilled water to permit any compaction to occur and stabilize prior to measurement. Following membrane compaction, the operating pressure was changed to 2 bar while the cross-flow rate was maintained constant. The permeate mass was measured every 5 minutes for 90 minutes, and recorded values were used to calculate membrane flux. All samples were tested using distilled water as feed.

2.3 Results and discussion

2.3.1 Morphological characteristics observed in SEM

The SEM micrographs presented in Figures 2.1 & 2.2 provide insight into the influence of particle loading and nonsolvent composition on final membrane morphology. Consider first the average particle size and particle size distribution depicted in Figure 2.1 and summarized in Table 2.2 (particle size data for 6 wt.% PEI and 21 wt.% PEI membranes

prepared in NMP:H_2O are not included due to difficulties in clearly distinguishing between PVDF and PEI particles). In Table 2.2, it is observed that the average particle size and corresponding distribution are independent of nonsolvent indicating that the particle dimensions are determined prior to casting the dope solution. In a second trend it is observed that at low PEI concentrations the particle size increases with increasing PEI loading. This positive correlation continues until reaching a threshold between PEI loadings of 38 wt.% and 48 wt.%, after which the average particle size decreases to 0.9 microns and the particle size distribution (PSD) narrows.

Table 2.2: Mean particle diameter (μm) and standard deviation for membranes with different particle loadings prepared using indicated nonsolvent

Wt. % PEI / Nonsolvent	06	21	38	48	54	60
IPA	1.1±0.4	1.6±0.5	1.8±0.7	0.9±0.2	0.9±0.2	0.9±0.1
H_2O	1.2±0.4	1.5±0.6	1.8±0.8	0.9±0.2	0.9±0.1	0.9±0.2
NMP:H_2O	-	-	1.9±0.7	0.9±0.1	0.9±0.1	0.9±0.2

The trend in particle size is attributed to the coalescence and breakup of phase separated PEI prior to completion of the crosslinking reaction. The phase separation of PEI from the rest of the dope, begins when the catalytic hydrochloric acid is added to the casting solution. The added HCl protonates some of the PEI molecules giving them a positive net charge. The charged PEI is no longer compatible with TEP (Appendix A) leading the casting solution to phase separate and form PEI rich droplets. Early during the crosslinking reaction the PEI rich droplets are free to breakup or coalesce as the solution is stirred. At low PEI concentrations this process is transitory leading to the formation of a broad distribution of particle sizes. At high PEI concentrations, droplet coalescence and breakup is at a dynamic steady-state resulting in a narrower size distribution. As the crosslinking continues, the polymerization of PEI eventually leads to the formation of stable particles that are covalently bound and no longer undergo coalescence or breakup.

Next, consider aspects of membrane morphology that are affected by both the nonsolvent and PEI particle loading. The top row of images in Figures 2.1 and 2.2 are for

IPA as nonsolvent. These show PVDF adopting "spherulitic" morphology: although their appearance differs from spherulites grown in polymer melts, they share the features of growth of lamellar PVDF crystals outwards from a nucleating site, giving a relatively spherical shape. In view of the change in scale from Figure 2.1 to Figure 2.2, the size of the spherulites observed o the surface that was exposed to the IPA (particularly for panels a and b of Fig. 2.2) is similar to that observed in the bulk (corresponding images in Figure 2.1). As discussed below, matching morphologies at the surface and in the bulk of the membrane is a signature of a nonsolvent that gradually produces sufficient supersaturation for nucleation of polymer crystals[22-23]. At the highest PEI loading, the bulk morphology is completely hidden beneath PEI particles.

In contrast to IPA, when water is the nonsolvent, there is a dramatically different morphology at the surface (Fig. 2.2 second row) then inn the bulk (Fig. 2.1 second row). The surface is covered by a thin, dense layer of PVDF; the bulk contains PVDF spherulites. This disparity is characteristic of a nonsolvent that abruptly quenches the solution at the surface into a deeply supersaturated state in which PVDF crystallizes "everywhere at once". The resulting PVDF skin slows the penetration of H_2O into the bulk, such that H_2O gradually produces sufficient supersaturation for nucleation of polymer crystals – which enables spherulites to form[23,24].

In the case of the mixed nonsolvent, 50:50 v/v NMP:H_2O, we see a morphology that, to or knowledge, has not been reported in the prior literature. In the bulk (third row of Figure 2.1), we observe tight porous spheres of PVDF. At intermediate PEI content (38%, Fig. 2.1h), these porous PVDF particles are decorated by PEI spheres or show "birds nest" cavities where PEI seems to have detached. The surface morphology is relatively dense (third row of Figure 2.2), increasingly so as PEI content increases (from panel g to panel i in Fig. 2.2).

Several molecular interactions govern the final morphology of mixed-matrix membranes prepared using the NIPS process. The four interactions addressed within this study are: nonsolvent-solvent, nonsolvent-PVDF, nonsolvent-PEI particles, and PVDF-PEI particles. The interaction between IPA and TEP is relatively minor because the two

molecules are readily miscible and have similar solubility parameters and polarities. Furthermore, IPA exhibits the same behavior as TEP when interacting with polymerized PEI (Fig. 2.3a&b), indicating that the IPA-PEI particles and IPA-TEP interactions do not significantly contribute to the final morphology of the membrane. Continuing to the IPA-PVDF interaction, IPA is well known in the literature as a soft nonsolvent for PVDF[23]. Being a soft nonsolvent indicates that a higher concentration of IPA is required to force PVDF out of solution and therefore the ternary solution formed during NIPS is more likely to undergo solid-liquid demixing. Indeed, the observations in Figures 2.1a-c and 2.2a-c support a solid-liquid demixing mechanism. The presence of ordered PVDF spherulites throughout the membrane indicates that the crystallization of PVDF drove the phase separation into polymer-rich and polymer lean phases. To further support the solid-liquid demixing mechanism, consider the PVDF-PEI particles interaction. If the phase separation was initiated by liquid-liquid demixing with the polymer crystallizing after the phase separation, then there would be no driving force for the PEI particles to be located solely on the edge of the PVDF spherulites. In contrast, the polymer crystallization driving the phase separation would push particles in the polymer-rich phase to the phase boundary.

As noted above, the behavior of the H_2O/TEP/PVDF system during the NIPS process has been studied extensively in the literature[18,19,23–27]. The observations and conclusions drawn from these studies provide a useful framework for addressing the morphology observed at the lowest PEI loading of 6 wt.% due to the similarities in their structures. In the literature, membranes prepared using the H2O/TEP/PVDF system exhibit a PVDF skin layer that is supported on a tight sponge layer that evolves into interconnected spherulites as the distance from the water/dope interface increases. In addition, following the phase inversion process the thicknesses of the membranes were found to be less than the casting height. Each of these observations may be explained using the four abovementioned interactions and the competition between kinetic and thermodynamic forces present in the H_2O -PVDF interaction. The kinetic forces are relevant under these conditions because of water's classification as a hard nonsolvent for PVDF[23]. To begin, consider the formation of the PVDF

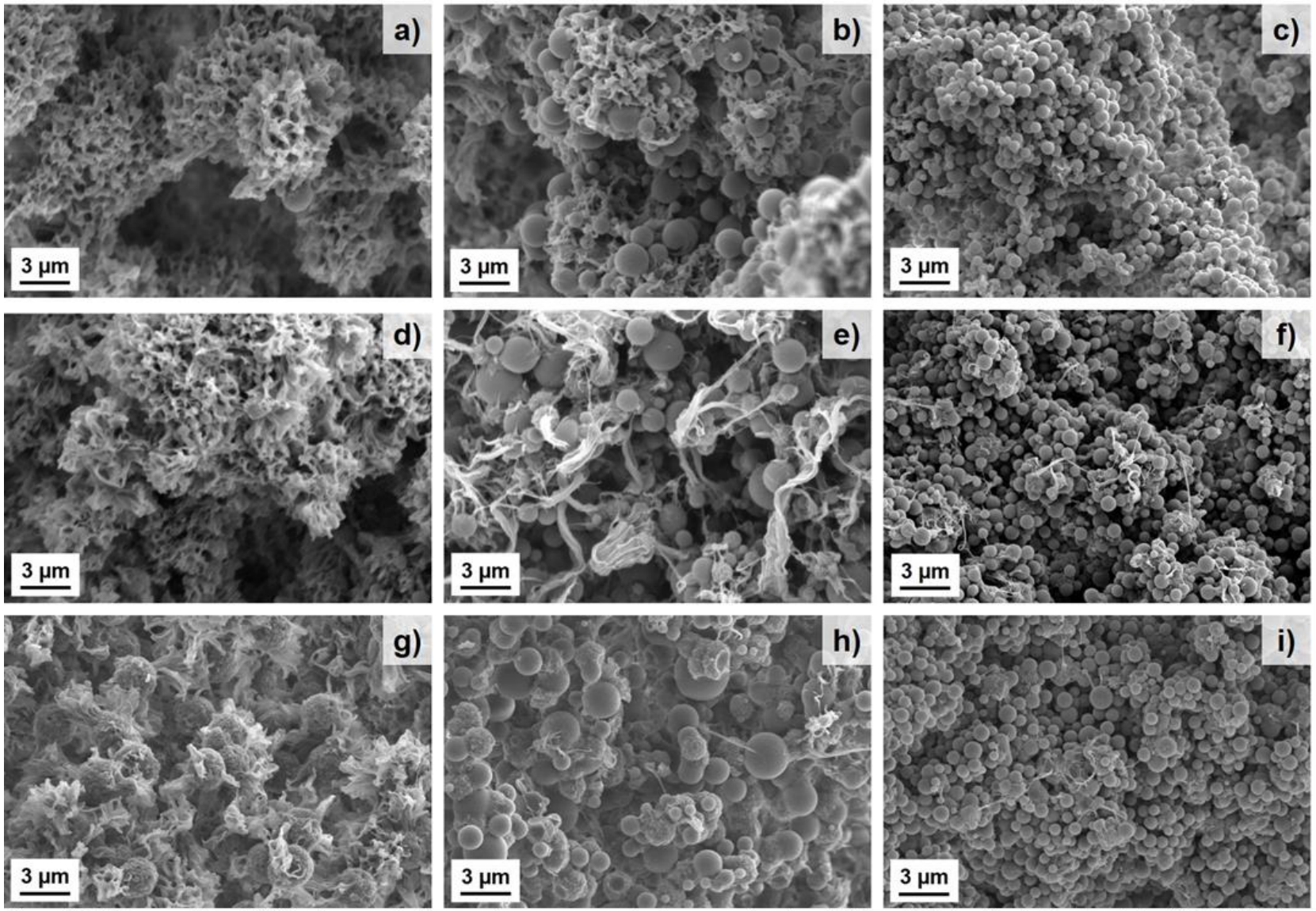

Figure 2.1: Cross-sectional SEM micrographs for membranes prepared using nonsolvent and PEI particle loading in the dry state of a) IPA & 6 wt.%, b) IPA & 38 wt.%, c) IPA & 54 wt.%, d) H_2O & 6 wt.%, e) H_2O & 38 wt.%, f) H_2O & 54 wt.%, g) NMP:H_2O & 6 wt.%, h) NMP:H_2O & 38 wt.%, and i) NMP:H_2O & 54 wt.%, where NMP:H2O is 50:50 by volume.

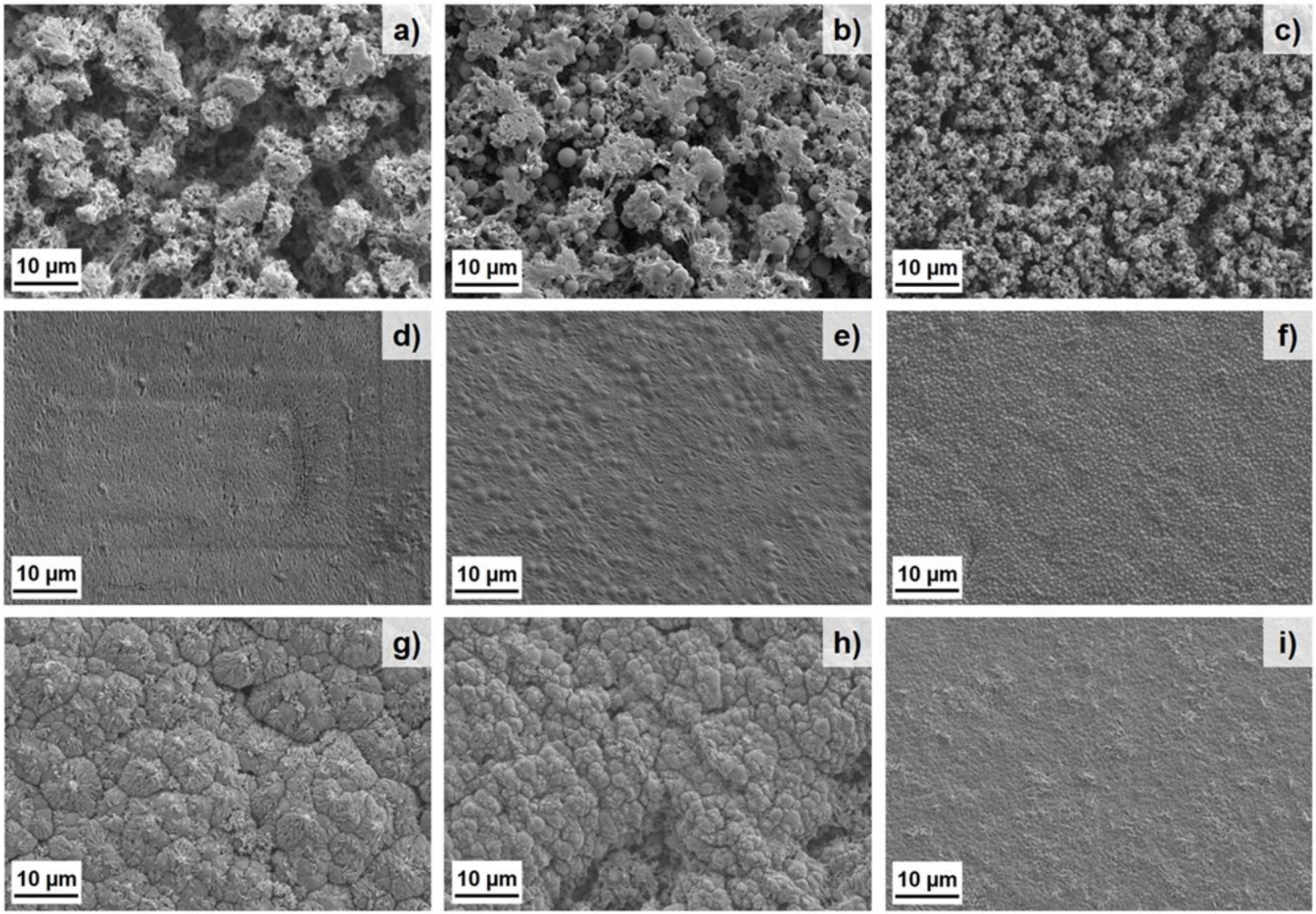

Figure 2.2: Surface SEM micrographs for membranes prepared using nonsolvent and PEI particle loading in the dry state of a) IPA & 6 wt.%, b) IPA & 38 wt.%, c) IPA & 54 wt.%, d) H_2O & 6 wt.%, e) H_2O & 38 wt.%, f) H_2O & 54 wt.%, g) NMP:H_2O & 6 wt.%, h) NMP:H_2O & 38 wt.%, and i) NMP:H_2O & 54 wt.%, where NMP:H2O is 50:50 by volume.

skin layer. Upon initial contact with the water bath, TEP and water rapidly interdiffuse resulting in PVDF precipitating out of solution at the water/dope interface. The rapid kinetics of this process leads to the formation of a tight PVDF skin layer, which then regulates the mass transfer between the dope and the nonsolvent bath[24]. The hydrophobic nature of the PVDF skin layer reduces the diffusion rate of water into the dope solution. The reduced rate gives rise to a transitionary region, the thickness of which scales as $t_{sld}^{1/2}$ or the time required for the skin layer to solidify, where the kinetic forces eventually give way to thermodynamic forces resulting in a shift in morphology.

The morphology of the 6 wt.% membrane cast in water deviates from these observations only in the placement of the PEI particles. It was expected that the hydrophilic nature of the PEI particles would lead to a significant contribution from the H_2O -PEI interaction; however, these observations indicate that a PEI loading of 6 wt.% is not enough to have a noticeable impact. In the spherulitic portion of the membrane the PVDF-PEI particle interaction behaved similarly to that observed when using IPA, which supports the shift to thermodynamic driven phase separation with increasing distance from the dope/water interface.

The literature framework outlining the contribution of the interactions to the final morphology proves to be of limited use at higher PEI loadings. Although the framework still explains how the relevant mechanisms lead to the formation of the PVDF skin layer, it fails to capture the lace-like structure of the PVDF throughout the rest of the membrane. The shift in the PVDF structure indicates that the contributions from the H2O-PEI and PVDF-PEI interactions play a central role in determining the final morphology. In the literature framework, the PVDF skin layer reduced the diffusion of water into the dope solution[24]. The reduced diffusion rate leads to a transition from kinetic (liquid-liquid demixing) to thermodynamic (solid-liquid demixing) forces dictating the polymer structure and subsequent overall membrane morphology.

Conversely, at a higher PEI loading the H_2O-PEI interaction increases the overall hydrophilicity of the skin layer allowing water to diffuse more quickly into the dope solution.

As water diffuses into the membrane, it is attracted to the hydrophilic PEI leading to water-rich regions around the PEI particles (Figure 2.3 c&d). The higher water concentrations near the PEI particles promotes kinetically driven liquid-liquid demixing of the nearby PVDF, producing the lace-like structure. If the concentration of PEI particles is high enough, as seen in the 38 wt.% and 54 wt.% cases, the improved hydrophilicity and subsequent promotion of liquid-liquid demixing may extend throughout the entire thickness of the casting solution. In this situation, the direct PVDF-PEI interaction is replaced by the indirect PEI/H_2O/PVDF interaction that represents a blending of the PVDF-PEI, H_2O-PEI, and H_2O-PVDF interactions. If the PEI loading is not high enough, as seen in the 6 wt.% case, the diffusion

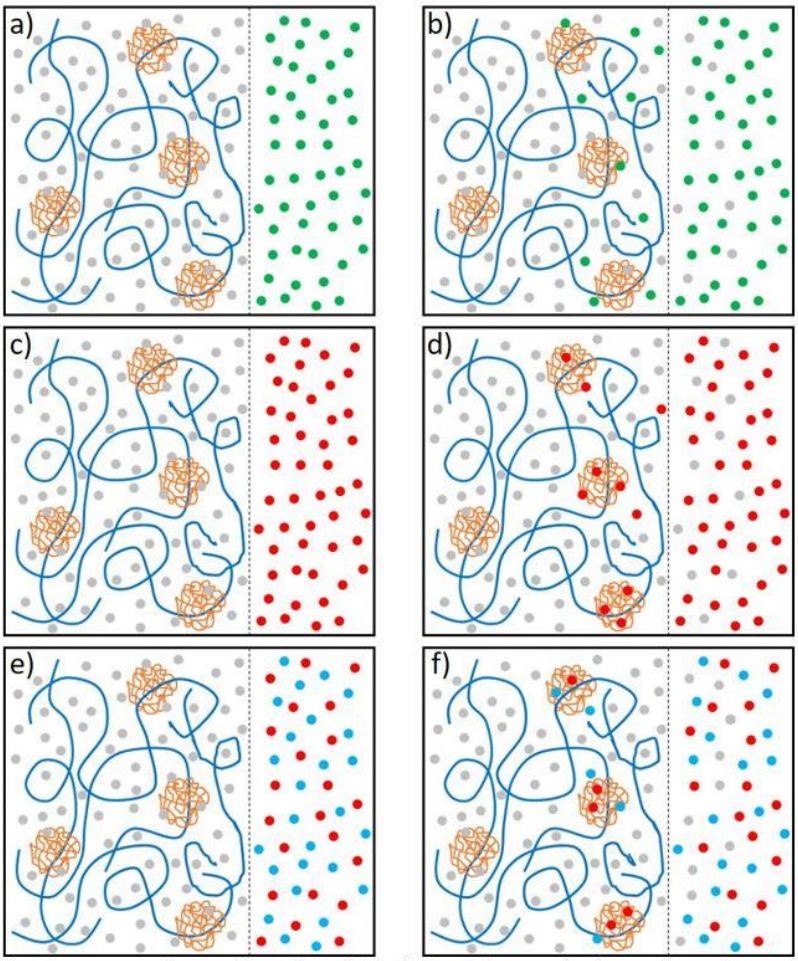

Figure 2.3: Schematics showing the casting solution–nonsolvent interface at t = 0 (panels a,c,&e) and t = t_d, the characteristic length scale for mutual diffusion, (panels b,d,&f). With ● - TEP, ● - IPA, ● - NMP, ● - H_2O, ~ - PVDF, - PEI.

of water into the bulk of the casting solution is too slow to promote liquid-liquid demixing resulting in thermodynamic forces determining the final morphology.

The morphology obtained using the mixed NMP:H_2O nonsolvent is unique and provides an interesting contrast to the morphologies obtained through thermodynamically driven (IPA) and kinetically driven (H_2O) PVDF solidification. Although NMP and H_2O are both polar and fully miscible, their interactions with TEP, PEI, and PVDF range from being similar (both are miscible in TEP) to vastly different (NMP is a solvent and H_2O is a nonsolvent for PVDF). The differences in interactions between the two components of the nonsolvent provide additional interactions to consider, including the separation of the mixed nonsolvent into H_2O and NMP.

Consider the scenario of PVDF dissolved in TEP with no PEI. In the absence of PEI, the two contributing interactions are (NMP:H_2O)-TEP and (NMP:H_2O)-PVDF. With both NMP and water being miscible with TEP, the two components of the nonsolvent diffuse together into the cast solution and initiate the phase separation process. In contrast to the rapid solidification of the PVDF skin layer when using water alone, the mixed nonsolvent slows the NIPS process in two ways. First, NMP is a better solvent for PVDF than TEP[24]; consequently a higher local concentration of water is required to induce PVDF crystallization. Second, the nonsolvent being a 50 v% mixture of water and NMP results in a slower increase in the concentration of water than is achieved when using pure water as the nonsolvent. These combined effects moderate solid-liquid demixing and produce a PVDF membrane morphology similar to that observed when using IPA in the absence of PEI particles.

In the absence of PEI particles, prior studies addressed the fundamental interactions in the context of a mixed nonsolvent that behaved like a single component of intermediate character. The presence of PEI in the dope solution introduces a driving force for the mixed nonsolvent to separate as it diffuses into a two phase mixture. Therefore, this analysis first considers the interactions between the small molecules, PVDF, and polymerized PEI. For PVDF the most favorable interactions are with NMP, followed by TEP, with water being

incompatible. For the PEI microgels the most favorable interactions (and highest swelling ratio) are with water, followed by NMP, with TEP the least favorable.

Upon immersing the dope solution into the mixed nonsolvent, the NMP:H_2O solution is attracted to the PEI particles and readily replaces the remaining TEP. As the concentration of the mixed nonsolvent increases in the PEI microgel, NMP moves to the interface between the PEI-rich and TEP/PVDF-rich regions due to its compatibility with both (Fig. 2.3 e and f). The movement of NMP produces an interfacial region around the PEI microgel with a higher concentration of NMP. The increasing water concentration in the PEI-rich phase drives the phase separation of the PVDF in the interfacial region, but the phase separation process is once again slower than when water alone is used and as a result the morphology is dictated by solid-liquid demixing. The polar influence of the H_2O rich PEI microgels on the adjacent PVDF solution causes nucleation and growth of a form of polar PVDF that appears as a condensed globular structure instead of loose spherulites. As the phase separation proceeds beyond this interfacial area, the polar influence is lost and the remaining PVDF forms loose lamella that grow from the globular structures. As the PEI particle loading increases, the NMP rich regions start to overlap leading to the formation of only globular PVDF as seen in Figures 2.1g&h. Similar to using water alone, there is a unique interplay

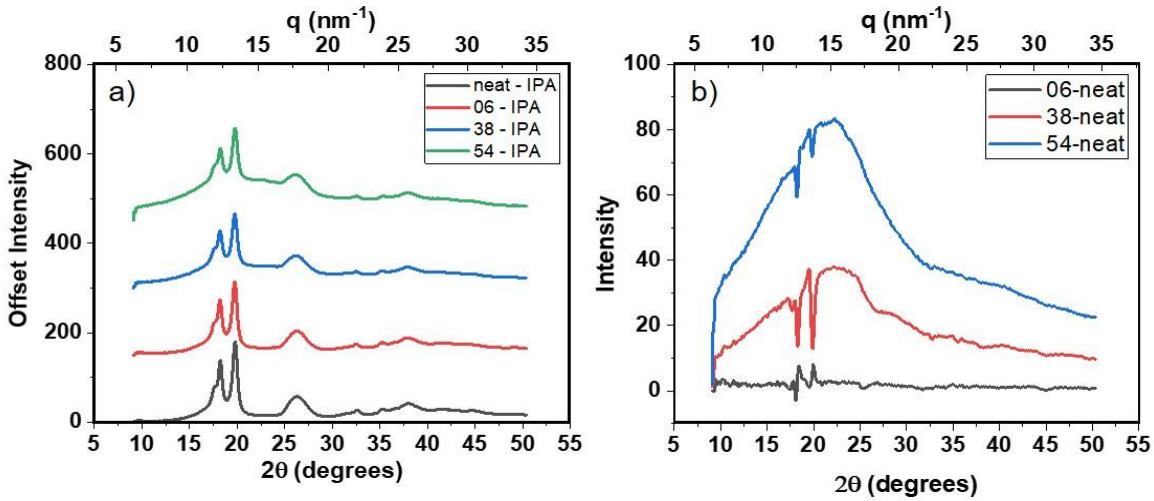

Figure 2.4: Plots showing a) background corrected x-ray scattering patterns for samples cast in IPA (with vertical offsets of 0 – neat, 175 – 06% PEI, 300 – 38% PEI, and 450 – 54% PEI), and b) Intensity obtained from subtracting the neat PVDF cast in IPA scattering from the indicated scattering pattern.

between the four interactions highlighted at the start of this section. The combined influence of the PEI particles and mixed nonsolvent produced a distinct and unique mixed-matrix membrane morphology.

2.3.2 Crystalline behavior of PVDF

An essential component of membrane morphology (and subsequent performance) when using semi-crystalline PVDF is the crystalline phase and degree of crystallinity. All references to x-ray scattering scans or sample intensity signals from this point forward will be referring to WAXS scans that have had the background signal subtracted unless otherwise indicated. Each scan in Figure 2.4a exhibits crystalline peaks associated with the α-phase of PVDF (see Table 2.3 for 2θ values corresponding to the different crystal phases) regardless of the PEI loading, indicating that the crystal phase in membranes prepared using IPA as the nonsolvent is independent of particle loading.

The independence of crystal phase from particle loading when using IPA as the nonsolvent, is in agreement with the observations from the SEM micrographs. As noted above, IPA is a soft nonsolvent for PVDF and does not interact strongly with PEI resulting in solidification through solid-liquid demixing. The subsequent crystallization encourages the formation of the most thermodynamically favored crystal phase – the α-phase. Although the PVDF-PEI interaction does influence the size and spacing of the PVDF spherulites, it does not affect the balance of kinetic and thermodynamic forces. Therefore, the crystalline phase is independent of PEI loading.

Table 2.3: Peaks associated with different crystal phases of PVDF. Peaks provided are obtained using Cu-kα radiation with wavelength 0.154 nm.[22,25,28]

Crystal phase	2θ peaks (degrees)
α	17.6, 18.3, 19.9, & 26.5
β	20.6, 36, & 40

To highlight the amorphous PEI contribution and its effects on PVDF crystallization in IPA, the scattering pattern of the neat sample was subtracted from those of the samples with different PEI loadings. To account for different concentrations of PVDF being present in each sample, the intensities of the neat sample were multiplied by a factor “r” that is the

ratio of the mass fraction of PVDF in the sample casting solution to the mass fraction of PVDF in the neat casting solution (Equation 2.1) before subtracting it from the sample's scattering pattern. The method of subtracting off the PVDF-concentration-corrected neat membrane scan was used to analyze the amorphous PEI contribution because the subtraction removes the bulk of the PVDF contributions (amorphous and crystalline) and any additional environmental background contributions not captured in the background scan. Furthermore, by using the scans of samples cast in IPA any confounding effects from different crystal phases were avoided thereby allowing additional information on changes in percent crystallinity of PVDF (fraction of PVDF that is crystalline) to be obtained. The changes in PVDF crystallinity between the samples were illustrated by the presence of peaks or valleys in the calculated curves at the position of the α-phase peaks.

$$r = \frac{wt\%_{PVDF,sample}}{wt\%_{PVDF,neat}} \tag{2.1}$$

The resulting curves (Fig. 2.4b) are dominated by a broad peak centered around 22º with a tail extending out to higher angles. The curves from the samples with higher PEI loading (38-neat and 54-neat) show valleys at both 18.3º and 19.9º. The curve produced using 6 wt.% PEI composition shows two small peaks at the same angles.The peaks in the IPA-cast 6 wt.% PEI difference pattern indicate an increase in the degree of crystallinity relative to the neat PVDF membrane. Similarly, the presence of valleys in the 38 wt.% and 54 wt.% PEI difference patterns (Fig. 2.4b) indicate that they have a lower degree of crystallinity relative to the neat PVDF case. Two potential ways that PEI microgels might frustrate PVDF crystallization are entrapment and obstruction. At high (≥ 38%) PEI loading, the fraction of PVDF that is entrapped in the PEI particles becomes significant. The entrapped PVDF is unable to crystallize due to the physical constraints of the gel and instead contributes to the amorphous phase. Similarly, as the number and size of particles increases there are fewer opportunities for crystals to grow without running into obstacles. The ability of a PEI microgel to obstruct crystallization depends on its size: the SEM image of the bulk morphology in an IPA-cast 38 wt.% PEI membrane shows that PVDF growth partially engulfs the PEI, indicating that the crystallization front moved faster than the microgels could

be excluded. In contrast, the morphology of IPA-cast 54 wt.% PEI membranes shows the PEI completely covers the growth front. This indicates that crystallization continued even as the PEI particles accumulated at the growth front. Thus, the larger size of PEI microgels in 38 wt.% PEI relative to 54 wt.% PEI is consistent with being more effective in blocking PVDF crystallization (deeper valley in Fig. 2.4b for 38 wt.% than 54 wt.%)

Membranes cast in water show a change in the PVDF crystal morph with increasing PEI concentration (Fig. 2.5a). In the absence of PEI and at low particle loadings the membrane is predominantly in the α-phase, consistent with its spherulitic morphology (Fig. 2.1d). A small shoulder is visible on the 19.9º peak in the scattering pattern of water-cast 6 wt.% PEI. This shoulder stems from the β-phase peak at 20.6º, which continues to grow as the PEI concentration increases and, at a PEI loading of 54%, surpasses the 19.9º α-phase peak.

To highlight the effect of a "hard nonsolvent" (water) relative to a "soft nonsolvent" (IPA), we examine the difference between the scattering pattern of a water-cast sample and that of the same composition membrane cast in IPA. Each of the paired scattering patterns probes the same amount of PVDF and PEI. The amorphous character of PEI ensures that

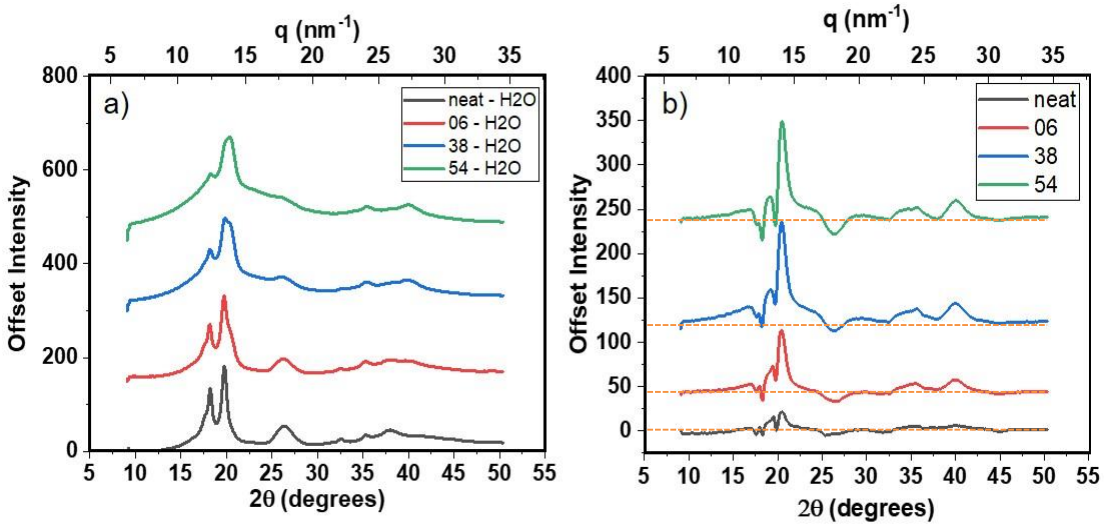

Figure 2.5: Plots showing a) background corrected x-ray scattering patterns for samples cast in H_2O (with vertical offsets of 0 – neat, 175 – 06% PEI, 300 – 38% PEI, and 450 – 54% PEI) b) Signal obtained from subtracting the scattering pattern of an IPA-cast membrane from that of its water-cast counterpart at the indicated particle loading. Orange dashed lines represent '0' for vertical offsets of 0 – neat, 45 – 06% PEI, 120 – 38% PEI, and 240 – 54% PEI

subtraction removes its contribution from the difference pattern. The amount of PVDF in the beam is the same inn both the IPA-cast and water-cast membranes. If the amorphous, α and β content of the PVDF is the same, then the subtraction will yield zero. A non-zero difference pattern reveals differences in PVDF crystallinity between water-cast samples and their IPA-cast counterparts.

In the case of neat PVDF, the difference pattern is weak (Fig. 2.5b), indicating that the ratios of amorphous:α:β are similar in the IPA-cast and water-cast membranes. The "valleys" at 17.6, 18.3, and 19.9º indicate that α-content is lower in the water-cast membrane; and the peak at 20.6º in the difference pattern shows that β-content is greater in the water-cast PVDF membrane, in accord with prior literature[22,25,28]. As little as 6% PEI significantly increases the differences inn PVDF morphology and crystallinity in water-cast relative to IPA-cast membranes: as an indicator of the increase in β-content relative to α –content, we define DPV as the Difference between the Peak at 20.6º and the depth of the Valley at 19.9º. The DPV increases from a value of 20 in the difference pattern of neat PVDF to a value of 47 in that of 6 wt.% PEI membranes. The ability of water to favor the β crystal morph continues to increase with PEI content: DPV increases to 71 and 98 for 38 wt.% and 54 wt.% PEI membranes respectively.

When TEP is used as a solvent, rapid liquid-liquid demixing in the presence of water leads to PVDF being kinetically trapped during solidification producing a mixture of β-phase and α-phase[22]. Without PEI particles present in the membrane, this phenomenon is restricted to the membrane skin layer because of the mass transfer limitations imposed by the formation of said layer. The reduced mass transfer of water slows the phase separation, thereby allowing time for the nucleation and growth of α phase lamella. A similar crystallization pathway occurs during the phase separation of casting solutions with low PEI loadings. The only indication of β-phase PVDF being the shoulder on the α-phase 19.9º peak, indicating that solid-liquid demixing was the dominant driving force during the phase separation. At higher PEI loadings, the hydrophilic microgels facilitate the mass transfer of water into the

casting solution, which promotes the faster liquid-liquid demixing process and subsequent formation of β-phase PVDF crystallites.

The subtraction of the IPA-cast scattering pattern from the water-cast one accomplished three things: First, it removes the contributions of PEI and any other environmental background sources not accounted for in the recorded background scan. Second, the difference pattern facilitates identification of changes in PVDF crystal phase as a function of PEI loading through the location and intensity of local peaks and valleys. Third, using this method to analyze x-ray scattering measurements of complex materials limits operator bias. There are still several opportunities to improve the quantitative capabilities of this method to more fully characterize the x-ray scattering of complex materials.

Membranes prepared using the mixed nonsolvent NMP:H_2O have x-ray scattering patterns that share several similarities with membranes cast in water, such as the α-phase dominated neat membrane and the shift from the α to β crystal phase with increasing PEI content (Fig. 2.6a). However, the shift in crystal phase occurs more abruptly when using the mixed nonsolvent, having already produced a plateau between the 19.9º and 20.6º peaks at a particle loading of 6%. This trend continues until reaching a particle loading of 54 wt.%, at which point the membrane is predominantly in the β crystal phase as seen by the almost complete suppression of the 18.3º and 26.5º α- phase peaks. The difference pattern obtained by subtracting the x-ray scattering pattern of the IPA counterpart is nearly zero for neat PVDF (Fig. 2.6b). In the absence of PEI, the mixed nonsolvent acts like a soft nonsolvent and produces the α crystal morph, which is favored due to the slow phase separation providing time for nucleation and growth. The difference patterns for membranes prepared with PEI have valleys at angles corresponding to diffraction peaks of the α crystal phase as well as local peaks at angles corresponding to the β crystal phase. The DPV (difference between the 20.6º peak and 19.9º valley) for membranes cast using the mixed nonsolvent are 6, 93, 117, and 138 for the neat, 6 wt.%, 38 wt.%, and 54 wt.% compositions respectively.

The strong shift in crystal phase when using the NMP:H_2O mixed nonsolvent (Fig. 2.6a) agrees with the observations and conclusions drawn from the SEM analysis. Once PEI

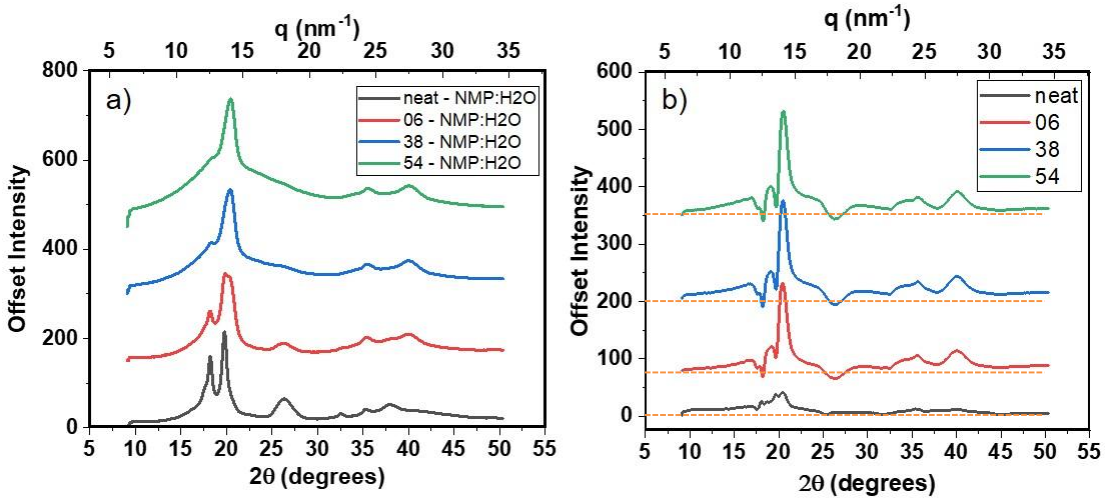

Figure 2.6: Plots showing background corrected x-ray scattering patterns for samples cast in NMP:H_2O (with vertical offsets of 0 – neat, 150 – 06% PEI, 300 – 38% PEI, and 450 – 54% PEI) b) Signal obtained from subtracting the scattering pattern of an IPA-cast membrane from that of its MP:H_2O-cast counterpart at the indicated particle loading. Orange dashed lines represent '0' for vertical offsets of 0 – neat, 75 – 06% PEI, 200 – 38% PEI, and 350 – 54% PEI

is added to the dope solution, PVDF near the PEI microgels form polar globular structures (Fig. 2.1) that are predominantly β-phase crystallites (Fig. 2.6). As the PEI loading and number of PEI particles increase, the NMP-rich interfacial regions start to overlap leading to increased formation of the globular PVDF and higher β-phase crystal content.

A comparison of the DPV for water-cast and NMP:H_2O-cast membranes provides additional insight into the crystallization of PVDF under the two conditions. Starting with the neat membranes, the water-cast membrane has a greater DPV than the mixed-nonsolvent-cast one (DPV of 20 and 6 respectively), indicating that in the absence of PEI the membrane produced by the mixed nonsolvent most closely resembles the IPA cast sample. This accords with the claim in prior literature that the mixed nonsolvent acts like a soft nonsolvent of PVDF. However, including PEI in the membrane "flips the script:" rather than moderating the hard-nonsolvent character of water, the NMP accentuates the changes in morphology seen in water-cast membranes relative to IPA cast counterparts. While water-cast and NMP:H_2O-cast membranes both have increasing concentrations of β-phase, at each composition, the membranes prepared with the mixed nonsolvent have a higher concentration of the β crystal phase. This phenomenon suggests that, relative to water alone,

the mixed nonsolvent increases the gradient at the interface between PEI microgels and the surrounding PVDF-rich dope in such a way that the formation of the β crystal phase is thermodynamically favored near the PEI particles. Therefore, increasing the PEI particle concentration increases the thermodynamically favored β-phase content and suppresses the formation of the α crystal phase such that it is theoretically feasible to have essentially pure β-phase PVDF.

2.3.3 Flux measurements

The flux through the membranes reveals the connection between structure and properties (Fig. 2.7) The open, spherulitic morphology of IPA-cast membranes (Fig. 2.1-2.2) gives high flux (1400 to 4000 $Lm^{-2}hr^{-1}$). Membranes cast in water have a tight skin layer

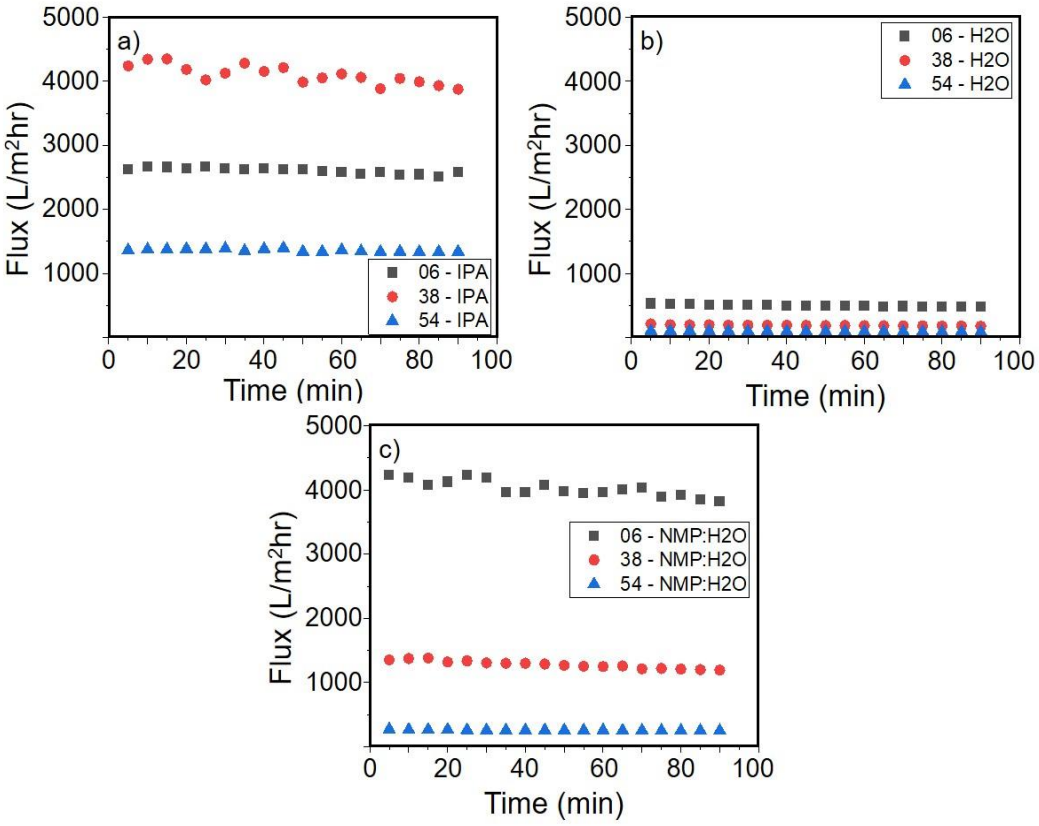

Figure 2.7: Plots of water flux as a function of time and particle loading for membranes prepared using a) IPA, b) H_2O, and c) NMP:H_2O

(Fig. 2.2) that correlates with observing low fluxes relative to their IPA counterparts (Fig. 2.7b) under the same operating conditions. Using the mixed nonsolvent produced membranes with unusual morphologies leading to The membranes prepared using the mixed nonsolvent produced membranes with unusual morphologies, which influenced the flux properties. For the highest PEI loading (45 wt.%), a dense skin forms that, indeed, gives low flux (similar to the water-cast membranes); for the lowest PEI loading, the surface layer is porous and the internal structure appears to consist of porous PVDF shells around PEI microgels. This 6 wt.% PEI membrane cast using NMP:H_2O provides a flux comparable to the 38 wt.% PEI, IPA-cast membranes (Fig. 2.7).

For membranes with different compositions prepared under the same casting conditions, it was initially proposed that higher PEI loadings would lead to higher fluxes due to the increasing hydrophilicity of the membrane. However, the observed fluxes (Fig. 2.7) demonstrate that flux and PEI loading negatively correlate with the notable exception of membranes cast in IPA, which have a maximum flux at the middle PEI loading of 38 wt.%. This maximum is attributed to optimizing the balance between membrane hydrophilicity and available pore volume. At low PEI loadings the MMMs have a higher mass fraction of PVDF that makes the overall membrane less hydrophilic resulting in reduced water flux through the membrane at a set operating pressure. As the mass fraction of PEI is increased to 38 wt.% and 54 wt.% the overall membrane becomes more hydrophilic facilitating improved water transport. Acting in opposition to the higher membrane flux encouraged by improved hydrophilicity, the increasing concentration of PEI microgels impedes mass transfer through the membrane by decreasing the pore volume available for transport. Therefore, at a PEI composition of 38 wt.% the IPA-cast membrane is more hydrophilic than a 6 wt.% membrane while having fewer microgels reducing transport pore volume than a 54 wt.% membrane producing the optimum conditions for a maximum membrane flux. Although the flux of the 54 wt.% PEI membrane is the lowest of the three compositions presented here, it has the highest concentration of functional particles while still being capable of operating in the microfiltration regime. As a result, the 54 wt.% PEI composition membranes cast in IPA

were used as the baseline material for the membrane chromatography experiments discussed in Chapter 3.

At low PEI concentrations – such as the 6 wt.% PEI composition – the mass percent of solids in the dope is low enough (Table 1) to allow defects in the surface layer during casting in mixed NMP:H_2O. These defects enable faster mass transfer through the membrane resulting in higher fluxes despite the lower membrane hydrophilicity. As the PEI loading and mass percent of solids increases to the 38 wt.% PEI composition the surface layer changes such that membranes cast in water demonstrate a continuous tight skin layer and those prepared using the mixed nonsolvent have a more homogeneous surface layer with reduced porosity. These changes in the surface layer result in decreased water fluxes for both sets of membranes.

2.4 Conclusions

In situ synthesis of PEI polymeric microparticles in PVDF dope opens new opportunities for manipulation of mixed-membrane morphology through control of *in situ* particle synthesis and interactions of the solvent and nonsolvent with the functional particles. Three important interactions and their influence on final morphology were reported. First, the correlation between particle size, PSD, and particle loading was attributed to reaching a steady state in droplet coalescence and break-up. Second, for single-component nonsolvents, the interplay between the nonsolvent-solvent, nonsolvent-PVDF, nonsolvent-PEI particles, and PVDF-PEI particles interactions govern the final membrane morphology. Third, using a mixed nonsolvent compromising a harsh nonsolvent and a secondary solvent provided additional interactions that and resulted in novel membrane structures. The structural characterization (SEM and WAXD) gave insight into the properties (flux) of the membranes fabricated in this study. Future work inspired by these results will be discussed in chapter 6.

References

(1) Mahajan, R.; Koros, W. J. Factors Controlling Successful Formation of Mixed-Matrix Gas Separation Materials. *Ind. Eng. Chem. Res.* **2000**, *39* (8), 2692–2696. https://doi.org/10.1021/ie990799r.

(2) Aroon, M. A.; Ismail, A. F.; Matsuura, T.; Montazer-Rahmati, M. M. Performance Studies of Mixed Matrix Membranes for Gas Separation: A Review. *Sep. Purif. Technol.* **2010**, *75* (3), 229–242. https://doi.org/10.1016/j.seppur.2010.08.023.

(3) Shen, Y.; Lua, A. C. Preparation and Characterization of Mixed Matrix Membranes Based on PVDF and Three Inorganic Fillers (Fumed Nonporous Silica, Zeolite 4A and Mesoporous MCM-41) for Gas Separation. *Chem. Eng. J.* **2012**, *192*, 201–210.

(4) Dong, G.; Li, H.; Chen, V. Challenges and Opportunities for Mixed-Matrix Membranes for Gas Separation. *J Mater Chem A* **2013**, *1*, 4610–4630. https://doi.org/10.1039/C3TA00927K.

(5) Geise, G. M.; Lee, H.-S.; Miller, D. J.; Freeman, B. D.; McGrath, J. E.; Paul, D. R. Water Purification by Membranes: The Role of Polymer Science. *J. Polym. Sci. Part B Polym. Phys.* **2010**, *48* (15), 1685–1718. https://doi.org/10.1002/polb.22037.

(6) Geise, G. M.; Paul, D. R.; Freeman, B. D. Fundamental Water and Salt Transport Properties of Polymeric Materials. *Prog. Polym. Sci.* **2014**, *39* (1), 1–42. https://doi.org/10.1016/j.progpolymsci.2013.07.001.

(7) Sagle, A.; Freeman, B. Fundamentals of Membranes for Water Treatment. 17.

(8) Werber, J. R.; Osuji, C. O.; Elimelech, M. Materials for Next-Generation Desalination and Water Purification Membranes. *Nat. Rev. Mater.* **2016**, *1* (5), 1–15.

(9) Werber, J. R.; Deshmukh, A.; Elimelech, M. The Critical Need for Increased Selectivity, Not Increased Water Permeability, for Desalination Membranes. *Environ. Sci. Technol. Lett.* **2016**, *3* (4), 112–120. https://doi.org/10.1021/acs.estlett.6b00050.

(10) Wang, P.; Chung, T.-S. A New-Generation Asymmetric Multi-Bore Hollow Fiber Membrane for Sustainable Water Production via Vacuum Membrane Distillation. *Environ. Sci. Technol.* **2013**, *47* (12), 6272–6278. https://doi.org/10.1021/es400356z.

(11) Li, X.; Sotto, A.; Li, J.; Van der Bruggen, B. Progress and Perspectives for Synthesis of Sustainable Antifouling Composite Membranes Containing in Situ Generated Nanoparticles. *J. Membr. Sci.* **2017**, *524*, 502–528. https://doi.org/10.1016/j.memsci.2016.11.040.

(12) Ghosh, S. K.; Alam, Md. M.; Mandal, D. The in Situ Formation of Platinum Nanoparticles and Their Catalytic Role in Electroactive Phase Formation in Poly(Vinylidene Fluoride): A Simple Preparation of Multifunctional Poly(Vinylidene Fluoride) Films Doped with Platinum Nanoparticles. *RSC Adv* **2014**, *4* (79), 41886–41894. https://doi.org/10.1039/C4RA06334A.

(13) Dai, B.; Yu, Y.; Chen, Y.; Huang, H.; Lu, C.; Kou, J.; Zhao, Y.; Xu, Z. Construction of Self-Healing Internal Electric Field for Sustainably Enhanced Photocatalysis. *Adv. Funct. Mater.* **2019**, *29* (16), 1807934. https://doi.org/10.1002/adfm.201807934.

(14) Liu, Z.; Yu, X.; Li, L. Piezopotential Augmented Photo- and Photoelectro-Catalysis with a Built-in Electric Field. *Chin. J. Catal.* **2020**, *41* (4), 534–549. https://doi.org/10.1016/S1872-2067(19)63431-5.

(15) Kotte, M. R.; Kuvarega, A. T.; Cho, M.; Mamba, B. B.; Diallo, Mamadou. S. Mixed Matrix PVDF Membranes With in Situ Synthesized PAMAM Dendrimer-Like Particles: A New Class of Sorbents for Cu(II) Recovery from Aqueous Solutions by Ultrafiltration. *Environ. Sci. Technol.* **2015**, *49* (16), 9431–9442. https://doi.org/10.1021/acs.est.5b01594.

(16) Liu, G.; Hung, W.-S.; Shen, J.; Li, Q.; Huang, Y.-H.; Jin, W.; Lee, K.-R.; Lai, J.-Y. Mixed Matrix Membranes with Molecular-Interaction-Driven Tunable Free Volumes for Efficient Bio-Fuel Recovery. *J. Mater. Chem. A* **2015**, *3* (8), 4510–4521. https://doi.org/10.1039/C4TA05881J.

(17) Park, M. J.; Nisola, G. M.; Vivas, E. L.; Limjuco, L. A.; Lawagon, C. P.; Seo, J. G.; Kim, H.; Shon, H. K.; Chung, W.-J. Mixed Matrix Nanofiber as a Flow-through Membrane Adsorber for Continuous Li+ Recovery from Seawater. *J. Membr. Sci.* **2016**, *510*, 141–154. https://doi.org/10.1016/j.memsci.2016.02.062.

(18) Rao Kotte, M.; Hwang, T.; Han, J.-I.; Diallo, M. S. A One-Pot Method for the Preparation of Mixed Matrix Polyvinylidene Fluoride Membranes with in Situ Synthesized and PEGylated Polyethyleneimine Particles. *J. Membr. Sci.* **2015**, *474*, 277–287. https://doi.org/10.1016/j.memsci.2014.09.044.

(19) Sun, C. Poly (Vinylidene Fluoride) Membranes: Preparation, Modification, Characterization and Applications. **2009**.

(20) Zuo, D. Y.; Li, H. J. Membrane Formation Mechanism for Water-Solvent-PVDF Systems and Membrane Structure for Ultrafiltration Application. *Adv. Mater. Res.* **2012**, *578*, 129–132. https://doi.org/10.4028/www.scientific.net/AMR.578.129.

(21) Zuo, J.; Chung, T.-S. PVDF Hollow Fibers with Novel Sandwich Structure and Superior Wetting Resistance for Vacuum Membrane Distillation. *Desalination* **2017**, *417*, 94–101. https://doi.org/10.1016/j.desal.2017.05.022.

(22) Buonomenna, M. G.; Macchi, P.; Davoli, M.; Drioli, E. Poly(Vinylidene Fluoride) Membranes by Phase Inversion: The Role the Casting and Coagulation Conditions Play in Their Morphology, Crystalline Structure and Properties. *Eur. Polym. J.* **2007**, *43* (4), 1557–1572. https://doi.org/10.1016/j.eurpolymj.2006.12.033.

(23) Zuo, D.; Zhu, B.; Cao, J.; Xu, Y. Influence of Alcohol-Based Nonsolvents on the Formation and Morphology of PVDF Membranes in Phase Inversion Process. *Chin. J. Polym. Sci.* **2006**, *24* (03), 281–289.

(24) Bottino, A.; Camera-Roda, G.; Capannelli, G.; Munari, S. The Formation of Microporous Polyvinylidene Difluoride Membranes by Phase Separation. *J. Membr. Sci.* **1991**, *57* (1), 1–20.

(25) Tao, M.; Liu, F.; Ma, B.; Xue, L. Effect of Solvent Power on PVDF Membrane Polymorphism during Phase Inversion. *Desalination* **2013**, *316*, 137–145.

(26) Su, Y. P.; Sim, L. N.; Li, X.; Coster, H. G. L.; Chong, T. H. Anti-Fouling Piezoelectric PVDF Membrane: Effect of Morphology on Dielectric and Piezoelectric Properties. *J. Membr. Sci.* **2021**, *620*, 118818. https://doi.org/10.1016/j.memsci.2020.118818.

(27) Lin, D.-J.; Chang, H.-H.; Chen, T.-C.; Lee, Y.-C.; Cheng, L.-P. Formation of Porous Poly(Vinylidene Fluoride) Membranes with Symmetric or Asymmetric Morphology by Immersion Precipitation in the Water/TEP/PVDF System. *Eur. Polym. J.* **2006**, *42* (7), 1581–1594. https://doi.org/10.1016/j.eurpolymj.2006.01.027.

(28) Gregorio Jr, R. Determination of the α, β, and γ Crystalline Phases of Poly (Vinylidene Fluoride) Films Prepared at Different Conditions. *J. Appl. Polym. Sci.* **2006**, *100* (4), 3272–3279.

Chapter 3

MIXED-MATRIX MEMBRANE CHROMATOGRAPHY

3.1 Introduction

The field of membrane chromatography has expanded rapidly as an alternative to the conventional packed bed chromatography in pharmaceutical separations[1–4]. The shift in technology has been motivated by a need to reduce downstream bioprocessing costs associated with long processing times and high operating pressures. Membrane chromatography reduces the processing time and operating pressure by utilizing convective, as opposed to diffusive, mechanisms to transport molecules of interest to the associated binding sites. The change in transport mechanism enables the system to operate at faster flow rates while maintaining a low operating pressure. In addition, the use of convective transportation allows for processing to be operated at a wide range of flow rates with minimal impact on the binding capacity of the membrane. These flow properties are amenable to the scale-up of the separation processes and complement the easy mass production of membrane-based materials thereby further reducing downstream costs[1,2]. The adoption of membrane chromatography has also benefited from drawing on the experience of related fields in membrane science, i.e., identification of porous polymeric membranes with good chemical and physical stability to act as supports. As a result, many membrane adsorbers are derivatives of membranes used in other separation processes[1–4].

In order to capitalize on the advantages of fast flow rates and low operating pressures outlined above, recent work has focused on addressing the key drawbacks of membrane chromatography. Two such drawbacks are the low volumetric binding capacity of membrane adsorbers in comparison to resins and limited salt tolerance[1,3–7]. While resins have a high binding surface area per volume ratio due to the tortuosity of the resin beads, early membrane adsorbers rely solely on the pore surface area as the active binding area resulting in low volumetric binding capacity. A promising method to overcome this barrier is to use various

polymerization techniques to graft polyelectrolyte chains or polymer brushes with appropriate functionalities onto the porous membrane supports[3–5,8]. The resulting membranes benefit from the porosity of the support while increasing the available binding surface area to improve volumetric binding capacity. However, the improvement in volumetric binding capacity has only been shown for solutions with low (<100 mM) salt concentrations[3–5].

Operating pharmaceutical separations in solutions with low ionic strength requires a buffer exchange step which increases processing costs[7]. In order to reduce the extent of the buffer exchange step, it has been necessary to develop membranes which demonstrate consistent binding over a range of salt concentrations. The improvement of the salt tolerance of membrane adsorbers requires a reduction in the ionic sensitivity of the binding ligand through manipulation of the ligand chemistry. Recent work replacing ligands with quaternary amine-based chemistry with those containing predominantly primary amine chemistry demonstrated volumetric binding capacities which were essentially constant over the conductivity range 1.8 mS/cm to 16.8 mS/cm[6,9–12]. Although these membranes achieved high salt tolerance, the reported volumetric binding capacities were low. While recent work in the field reliably addresses one of the drawbacks mentioned above, there is still a need for a membrane adsorber which provides a consistently high volumetric binding capacity over a wide range of salt concentrations.

In this study we build upon results from chapter 2 and investigate the relationship between crosslinker chemistry, crosslinker density, and volumetric binding capacity. We chose three unique crosslinkers with different reactive groups, connecting chain chemistry, and lengths to characterize the influence of crosslinker chemistry in diverse conditions. Epichlorohydrin (ECH) is the shortest crosslinker and provides only an alcohol functionality post-reaction, Bis(2-chloroethyl)amine hydrochloride (BCAH) has a medium length and provides an additional secondary amine post-reaction, and Di(ethylene glycol) diacrylate (EGA) is the longest crosslinker and provides glycol functionality post-reaction. All three crosslinkers were used in varying concentrations to obtain information on the interplay between crosslinker chemistry and crosslink density and the resulting impact on volumetric

binding capacity. The binding capacity was measured in both static and dynamic configurations to demonstrate the capabilities of mixed-matrix membranes adsorbers.

3.2 Experimental Methods

3.2.1 Materials

Polyvinylidene Fluoride (PVDF; Kynar 761, 400 kg/mol) was donated by Arkema. Hyperbranched polyethylenimine (PEI; 600 g/mol) was purchased from Polysciences. The following chemicals were purchased from Sigma Aldrich: Epichlorohydrin (ECH), Di(ethylene glycol) diacrylate (EGA), Bis(2-chloroethyl)amine hydrochloride (BCAH), Isopropanol (IPA), Triethyl phosphate (TEP), Dimethyl sulfoxide (DMSO), TRIShydrochloride (TRIS), Glycerol, and Bovine Serum Albumin (BSA). The 1x PBS solution (Corning 21-040-CV) was purchased from VWR. All chemicals and materials were used as received. All buffers were prepared using indicated chemicals and distilled water.

3.2.2 Membrane Synthesis

To begin a typical membrane synthesis, 5.91 g of PVDF was added to an empty 3-neck round bottom flask. The flask was fitted with an overhead mechanical stirrer and the necessary greased connectors. Thirty mL of TEP was then added to the flask and the remaining openings were sealed using rubber septa. The PVDF/TEP mixture was heated to 80 ºC for an hour before the mixing speed was set to 60 rpm. The resulting solution was left to equilibrate overnight. A PEI/TEP solution was prepared by adding 5 g of PEI to a scintillation vial followed by 5 mL of TEP. The mixture was vortexed until a homogeneous clear solution was obtained and then it was left to equilibrate overnight at room temperature. For membranes with BCAH as the crosslinker, the crosslinker solution was prepared by weighing the required amount of BCAH into a scintillation vial and then adding the corresponding volume of DMSO (Table 3.1). DMSO was chosen as the solvent due to its compatibility with the other components of the dope solution and TEP’s inability to dissolve

BCAH. The resulting mixture was incubated overnight at room temperature to fully dissolve the BCAH.

$$NCD = \frac{\frac{[crosslinker]}{[PEI]}}{\frac{[crosslinker]_{ref}}{[PEI]_{ref}}} \quad (3.1)$$

Once the solutions were equilibrated, the flask was purged with N_2 for 7 minutes and the mixing speed was increased to 250 rpm. With the N_2 flow still on, the PEI solution was then added dropwise to the flask using a glass Pasteur pipette over the course of 4 minutes. The resulting solution was left to mix for 5 minutes before adding 0.43 mL of concentrated HCl (37% solution). Following the addition of the HCl, the flask was incubated for 15 minutes at 80 ºC with the mixing speed maintained at 250 rpm. The crosslinker solution corresponding to the desired normalized crosslink density (NCD) in Table 3.1, calculated using equation 3.1, was then added to the flask and the polymerization reaction was allowed to proceed for 4 hours. After the 4-hour reaction time, the flask was put under in-house vacuum for 10 minutes to remove entrapped air. The membranes were then cast on glass plates using a doctor blade with a blade height of 300 µm. The cast membranes were left at room temperature for 30 seconds before being immersed in an Isopropanol coagulation bath. After two hours, the solidified membranes were moved to distilled water baths prior to storage.

Table 3.1: Crosslinker solution composition with the corresponding Normalized Crosslink Density and membrane formulation.

Formulation	Crosslinker	Crosslinker mass(g)	NCD	Volume of DMSO (mL)
54A	ECH	3.2	1	-
54B	ECH	1.6	0.5	-
54C	ECH	0.8	0.25	-
54D	EGA	7.4	1	-
54E	EGA	3.7	0.5	-
54F	EGA	1.8	0.25	-
54G	BCAH	6.2	1	8
54H	BCAH	3.1	0.5	5
54I	BCAH	1.6	0.25	2.5

3.2.3 SEM characterization

Please see the corresponding section in Chapter 2 for detailed description on SEM characterization method.

3.2.4 Protein binding experiments

Static protein binding experiments were performed for all formulations in Table 3.1. The two formulations with the highest binding (54E & 54H) were then used to test salt tolerance in water and the buffers listed in Table 3.2. The static binding capacity (SBC) experiment operated as follows. A 2 mg BSA/mL solution was prepared by dissolving BSA in the appropriate solvent as outlined in Table 3.2. A 12mm x 12mm sample token was then cut out of the membrane of interest and immersed in 5 mL of the BSA solution. The solution was rocked gently for 48 hours before the absorbance at 280 nm was measured using an Agilent 8453 UV/vis spectrometer. The concentration of BSA in the solution was then estimated using an absorbance/concentration calibration curve. The mass of BSA bound was then determined using a mass balance, while the membrane volume was calculated using the sample thickness determined via SEM imaging. Replicates of each formulation were tested with the average binding capacity and standard deviations reported in Figure 3.3.

Dynamic protein binding experiments used membranes with formulation 54H because they demonstrated the best binding capacity in the presence of salt. The dynamic binding measurements were performed using a precision adsorption flow-through cell with operating volume of 80 μL from Hellmanex and the UV-vis' time resolved module. The measurements were performed as follows.

A 2 mg/mL BSA solution was prepared by dissolving BSA in 50 mM TRIS buffer with varying salt concentrations (0, 50, 100, 150, and 200 mM respectively). Flat sheet membranes were cut into circle tokens with a diameter of 25.4 mm, hereafter referred to as samples, while they were still wet. The prepared samples were stored in 50 mM TRIS buffer.

A nonwoven PET support was also cut into circles with a diameter of 25.4 mm. A control measurement was taken by loading one layer of the PET support into the sample holder and then introducing the BSA feed solution at a constant flowrate. The time-resolved absorbance at 280 nm was captured using a UV-vis spectrometer. The sample was then loaded into the sample holder on top of a fresh PET support to account for any nonspecific binding to the nonwoven support. The sample was equilibrated to the feed solution using the appropriate buffer. Once the sample was equilibrated, the BSA feed solution was introduced at a constant flowrate using a syringe pump. The flowrates investigated in these experiments were 0.3, 0.6, 1.2, & 1.5 mL/min, corresponding to 2, 4, 8, & 10 membrane volumes/minute, respectively. The lowest flowrate (0.3 mL/min, 2 MV/min) was only measured in TRIS buffer with 0 mM NaCl. The mass of BSA bound by the membrane was then calculated by taking the difference in the mass of BSA loaded between the sample and the control at 10% breakthrough.

3.3 Results and Discussion

3.3.1 Changes in morphology

Figure 3.1 shows SEM micrographs of the membrane cross-sections prepared with different crosslinkers at NCD 0.5. Using ECH as the crosslinker, 3.1a, produces microgels that form distinct spheres with a large size distribution (0.5-3 microns) when dried. This is a notable deviation from the tight size distribution of the spherical microgels when ECH has an NCD of 1.0 (Fig. 2.2c). In contrast to the regular spheres obtained with ECH, using EGA as the crosslinker produces microgels that are interconnected thereby losing the distinct spherical shape. The tightest distribution of microgel sizes in the dry state is seen in Figure

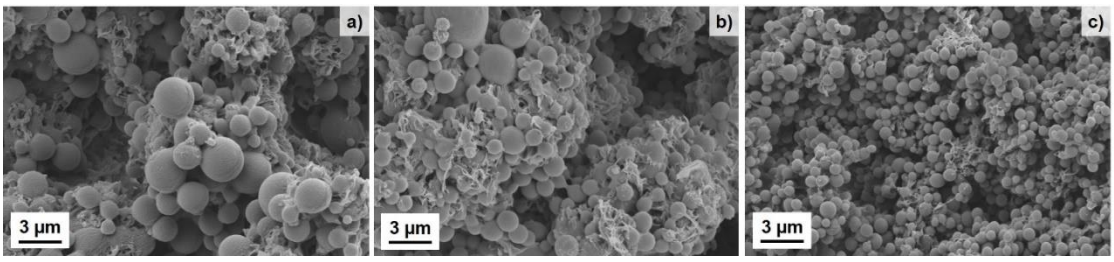

Figure 3.1: SEM micrographs of membrane cross-sections showing change in microgel shape and distribution using NCD of 0.5 and crosslinker chemistry of a) ECH, b) EGA, c) BCAH

3.1c, when BCAH is used as the crosslinker. The tight size distribution and smaller average particle size is equivalent to those produced when using ECH at an NCD of 1. This finding is particularly interesting for two reasons: First, EGA does not produce a similar morphology at any of the NCDs investigated in these experiments. Second, the concentration of halide bonds in the crosslinker is the same for ECH at NCD of 1 and BCAH at NCD of 0.5. These two observations seem to indicate that the halide concentration plays an essential role in determining particle morphology.

Figure 3.2 displays SEM micrographs of membrane cross-sections prepared using BCAH at NCDs of 0.25, 0.5, and 1 (a-c respectively). At a low BCAH concentration few functional particles are visible indicating that formation of the microgels is suppressed at low NCD. The microgel suppression is attributed to PEI which is not entangled with PVDF escaping the gel during casting. At a high BCAH concentration, NCD of 1, the functional microgels exhibit a structure consistent with a collapsed hollow sphere in the dry state. The transition to forming hollow spheres at high crosslink densities has not been fully investigated at this time, but one documented contribution is the interaction between dissolved PEI and droplets of BCAH/DMSO. The change in particle morphology is also accompanied by a shift in PVDF structure. The membranes prepared at NCDs of 0.25 and 0.5 both show PVDF structures consistent with using IPA as the nonsolvent (Ch. 2.3.1), while the membrane with NCD of 1 shows PVDF structures more consistent with using H_2O:NMP as nonsolvent. The change in PVDF morphology stems from the addition of DMSO, which at high enough concentrations influences the PVDF structure in a similar way as NMP does when using the mixed nonsolvent.

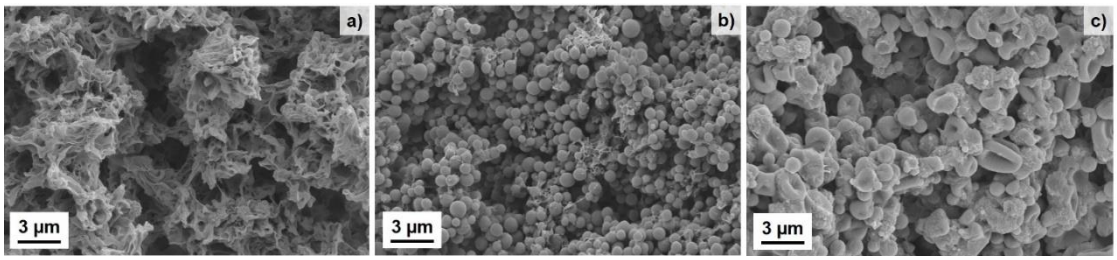

Figure 3.2: SEM micrographs of membrane cross-sections showing changes in microgel distribution and structural polymer morphology with changing crosslink density a) NCD - 0.25, b) NCD - 0.5, c) NCD - 1.0

3.3.2 Static binding

The static binding capacities depicted in Figure 3.3 provide key insights to the relationship between crosslinker chemistry, crosslink density, and SBC. For instance, the SBC of membranes prepared with EGA and BCAH both have a local maximum at NCD of 0.5, which is significantly higher than the binding capacities at NCDs of 1 or 0.25. Noting that BCAH and EGA are both homofunctional molecules, the local maximum is attributed to the influence of crosslink density on gel tightness and cohesion. At high crosslinker concentrations the gel is tightly crosslinked, which limits its ability to swell in water. The limited swelling leads to a low SBC because only a portion of the BSA binding sites are available to interact (due to the binding sites being dispersed throughout the entire gel and not just located on the surface). In contrast, low crosslinker concentrations negatively influences both gel cohesiveness and microgel concentration resulting in a lower binding capacity. At an NCD of 0.25 there are few enough crosslinks such that an uneven distribution of crosslinks per PEI leads to several PEI molecules which are not covalently bound to the gel prior to casting the membrane. The non-crosslinked PEI molecules get removed during the coagulation and washing steps, leading to a lower number of binding sites in the

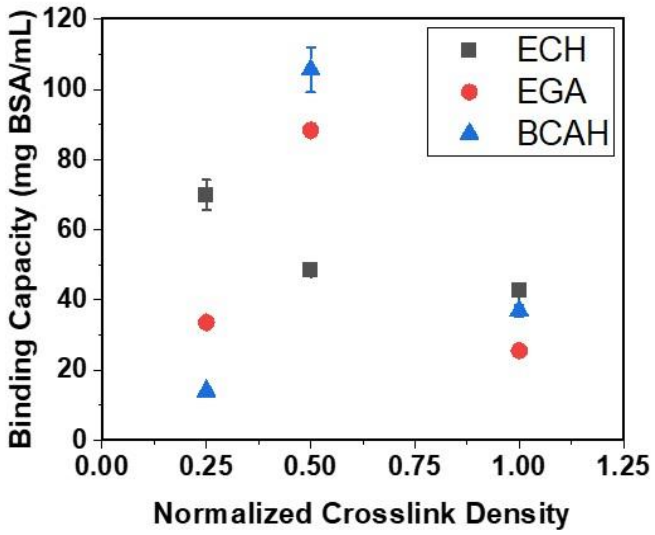

Figure 3.3: Static binding measurements depicting differences in binding capacity as a function of crosslinker chemistry and crosslink density in H_2O.

membrane and a lower overall binding capacity. At NCD 0.5 the gel is open enough to maximize availability of functional sites while having sufficient crosslinks to maintain gel cohesion and PEI concentration. The balance of these two contributions gives rise to the observed maximums corresponding to membranes 54E and 54H. These observations are also validated by the reduction in particle size and change in particle shape observed in the SEM micrographs of Figure 3.2.

Changes in crosslink density provides a feasible explanation for the observed trends in membranes prepared using both EGA and BCAH, but consideration of crosslinker chemistry is needed to account for the differences between these membranes at a given crosslink density. Membranes synthesized with BCAH have higher binding capacities at NCDs≥0.5, while at an NCD of 0.25 using EGA results in higher BSA binding. The higher binding when using BCAH is attributed to the additional secondary amine incorporated into the gel during the PEI polymerization reaction. The higher binding of membranes prepared with EGA at NCD 0.25 has not yet been fully explored but may be explained by using BCAH leading to a lower gel cohesion because of its slower reaction kinetics and short length. Crosslinker chemistry also plays a critical role in explaining why membranes prepared with ECH exhibit a decreasing SBC with increasing NCD. In contrast to BCAH and EGA, ECH is a short heterofunctional molecule with one functional group (epoxide) that reacts significantly more quickly than the other (halide). The difference in reaction rates could lead to a more even distribution of crosslinks at lower NCD thereby reducing the percentage of the PEI which escapes the membrane. As the crosslink density increases the even distribution of crosslinks and shorter length of ECH results in a tighter gel leading to a low BSA binding.

3.3.3 Salt tolerance

As discussed in the previous section, membranes 54H and 54E were used for the salt tolerance measurements due to their high BSA binding capacity in water. The static binding capacities for 54H and 54E, depicted in Figure 3.4, demonstrate that both crosslinker chemistry and buffer composition (excluding added salts) influence membrane salt tolerance. The influence of crosslinker chemistry is demonstrated by comparing the percent decrease

in binding capacity with increasing buffer conductivity. Using the BSA binding capacity in water as the reference, membranes prepared with EGA, 54E, have a reduction in binding capacity of 25%, 40%, & 80% when using buffers T-05, T-10, and T-20. In comparison, membranes prepared using BCAH, 54H, have binding capacities within error of the reference when using T-05 and T-10 buffers. In the T-20 buffer, membrane 54H demonstrates a BC reduction of 40%. Similar behavior is observed when the PBS buffers are used. However, a comparison between binding capacities in different buffers with similar conductivities reveals that using a PBS based buffer has a detrimental effect on SBC. While this trend holds true for both 54H and 54E membranes, the effect is more pronounced when using EGA as the crosslinker. For example, the percent reduction from T-05 to P-05 is 5% when 54H is used and 37% when using 54E. Figure 3.4 also demonstrates that incorporating glycerol (P-1G) at the same concentration as the TRIS buffer improves the SBC in the PBS buffer.

Table 3.2: Composition of buffers used during salt tolerance measurements. Each buffer had a pH of 7.4 and the following concentrations of the buffer chemistry: 1 – 50 mM TRIS, 2 – 0.5x PBS, and 3 – 1x PBS.

	T-00	T-05	T-10	T-15	T-20	P-05	P-10	P-1G
Buffer chemistry	TRIS[1]	TRIS[1]	TRIS[1]	TRIS[1]	TRIS[1]	PBS[2]	PBS[3]	PBS[3]
Added NaCl (mM)	0	50	100	150	200	-	-	-
Glycerol (mM)	-	-	-	-	-	-	-	50
Conductivity (mS/cm)	4.6	9.8	15	19.5	24.7	9.1	17.6	18

The divergence in SBC of membranes 54E and 54H at higher conductivities (using the same base buffer) indicates that there is a contribution to the binding mechanism that is more pronounced when using BCAH as the crosslinker. Prior literature has explained the source of this contribution by demonstrating that incorporating primary and secondary amines enables binding in high salt environments through alternative binding mechanisms, such as hydrogen bonding[6,9]. It is also noted in both studies that tertiary and quaternary amines do not demonstrate binding in solutions with higher conductivities because they only use electrostatic interactions, which are increasingly screened by salt ions as the conductivity

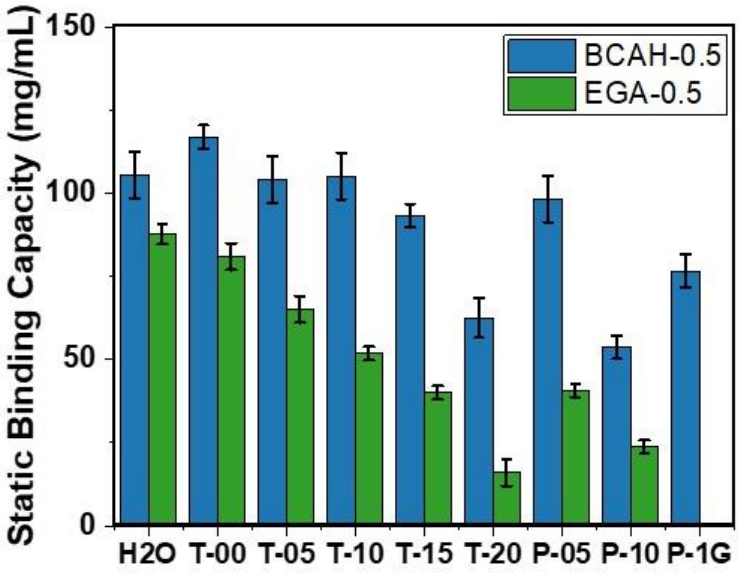

Figure 3.4: Static binding capacity of BSA dissolved in water and TRIS/PBS buffers with varying conductivities.

rises. During the PEI polymerization reaction primary and secondary amines are consumed by the crosslinkers producing secondary and tertiary amines respectively. Therefore, when EGA and ECH are used as crosslinkers some of the secondary amines of PEI will be consumed and turned into tertiary amines. Due to each tertiary amine being a site that can only bond through electrostatic interactions, the tertiary amines produced may be considered a loss of binding capability at higher salt concentrations. Similarly, using BCAH as the crosslinker produces new tertiary amines during the PEI crosslinking; however, each BCAH molecule also adds a new secondary amine to the polymerized PEI gel. As a result, BCAH has significantly more sites capable of hydrogen bonding for a given crosslinker molar concentration.

Prior literature has provided several examples of salt tolerance in TRIS[6,9,11–14] and PBS[3,4,15] based buffers, but to our knowledge no study has compared binding performance between the two buffers to determine buffer sensitivity of a given membrane. The buffer sensitivity revealed in Figure 3.4 highlights the importance of identifying a suitable buffer for a given pairing of membrane material and protein of interest. Under these specific conditions, the observed behavior is a result of differences in buffer chemistry that leads to changes in the interactions between the buffer, PEI microgels, and BSA. TRIS, being an

organic molecule consisting of an amine group and three hydroxyl groups, can interact with the binding ligand and BSA through both electrostatic interactions and hydrogen bonding. The ability of TRIS buffer to form hydrogen bonds may magnify the PEI microgel's hydrogen bonding contribution, thereby reducing the effects of electrostatic screening at higher conductivities. In contrast, PBS is composed of monohydrogen and dihydrogen phosphate salts as well as NaCl and KCl. As a result, the PBS buffer has little impact on the hydrogen bonding contribution and predominantly screens the electrostatic binding interactions leading to a lower volumetric binding capacity. In order to confirm that hydrogen bonding of the buffer makes a significant contribution to SBC, static measurements were conducted using 1xPBS with 50mM glycerol. Glycerol was chosen both for its propensity to form hydrogen bonds and its property of remaining neutral in water. The combination of these two properties verifies that any improvement in BSA binding between P-10 and P-1G is solely due to hydrogen bonding form glycerol. The improvement of over 40% supports the claim that hydrogen bonding of the buffer makes a significant contribution to SBC. The difference in capacity between P-1G and T-15 has still not been fully determined, but there is feasibly a synergistic effect between charge and hydrogen bonding on TRIS that facilitates higher BSA binding.

3.3.4 Dynamic binding

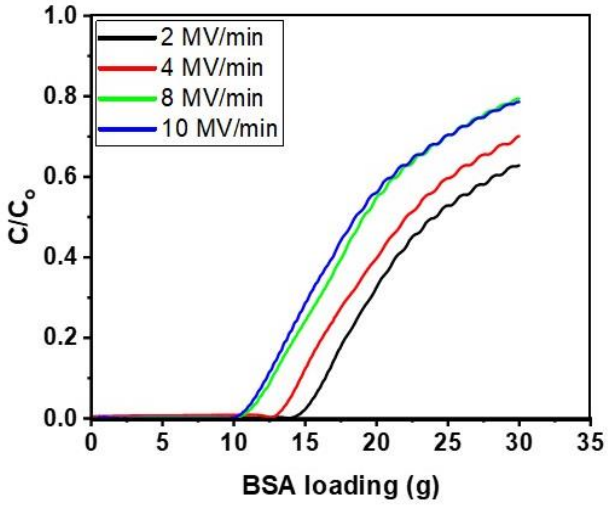

Figure 3.5: Breakthrough curves for membrane 54H in 50 mM TRIS at various flowrates to demonstrate regime of flowrate dependence at low volumetric flows.

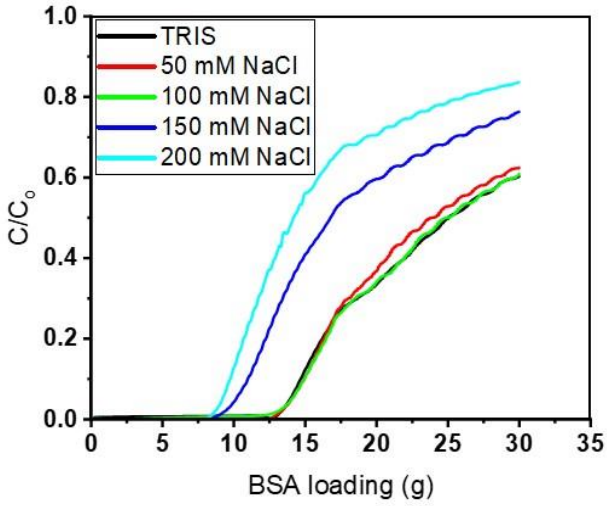

Figure 3.6: Breakthrough curves for membrane 54H at 0.6 mL/min (4 MV/min) in TRIS buffer with varying amounts of added salt demonstrating salt tolerance under flow.

One of the key advantages of traditional membrane chromatography is independence from flowrate that allows membranes to be used at high flowrates without sacrificing binding capacity[1–5,9]. As seen in Figure 3.5, the combination of resin and membrane properties exhibited by mixed-matrix membranes introduces a regime of flowrate dependence. At low flowrates (Fig. 3.5, 2 and 4 Membrane Volumes/min) the additional time BSA has to penetrate and bind with the functional microgel is inversely proportional to the volumetric flow rate leading to decreasing binding capacity as the flowrate is increased. As the flowrate continues to increase (Fig. 3.5, 8 & 10 Membrane Volumes/min) the binding capacity plateaus and is no longer flowrate dependent indicating that the mass transfer to binding is dominated by convective forces similar to other membrane-based adsorbers.

The modified mixed-matrix membrane's salt tolerance under flow agrees with the trend observed in the static binding measurements. As seen in Figure 3.6, the BSA breakthrough curves are essentially constant in the presence of TRIS buffers with up to 100 mM NaCl added. As the salt concentration increases past 100 mM NaCl, the curves shift to the left indicating that the DBC decreases. Noting how the trend in DBC with respect to salt concentrations changes across the different flowrates tested (Fig. 3.7) is important to characterizing the binding behavior of the PEI microgels. As noted above, at low flowrates

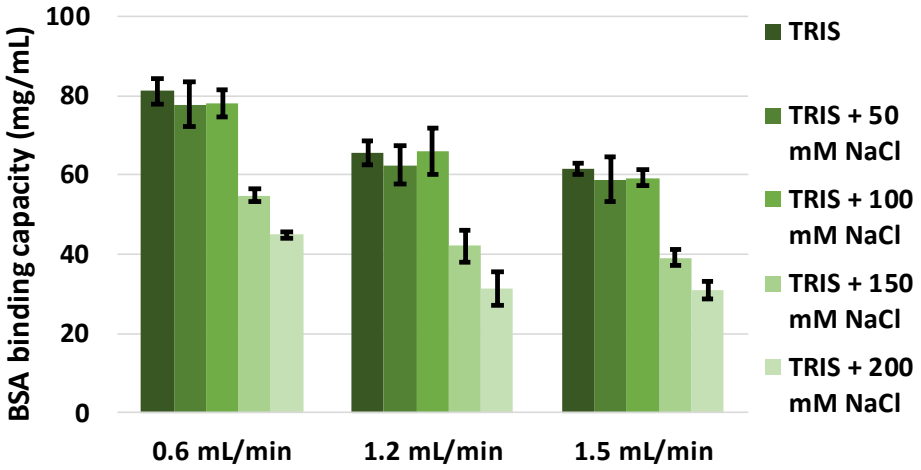

Figure 3.7: Dynamic binding capacities for membrane 54H at three different flowrates and 5 different buffer conditions, highlighting trends in salt tolerance behavior.

BSA is able to more fully penetrate the functional microgels leading to a higher binding capacity. In contrast, at high flowrates BSA diffuses a shorter distance and therefore interacts with a smaller portion of the various microgels. By comparing how the DBC reacts to salt concentration at different flowrates, it is possible to draw qualitative comparisons to the binding interactions of different portions of the microgels. For example, if the salt tolerance at lower flowrates showed a smaller percentage reduction between binding in TRIS buffer alone and TRIS buffer with 200 mM NaCl than the difference at a higher flowrate, it would suggest that the edges of the microgel have a lower salt tolerance than the interior of the microgels. Comparing the percent reduction in DBC of the flowrates presented in Figure 3.7 provides the following: 0.6 mL/min – 45±3%, 1.2 mL/min – 52±9%, and 1.5 mL/min – 50±5%. There is not a statistically significant difference between the three flowrates suggesting that the binding interactions across the microgel are equivalent (p-value ≤ 0.05).

3.4 Conclusions

The influence of crosslinker chemistry and crosslink density on volumetric binding capacity and salt tolerance was investigated during this study. It was determined that the volumetric binding capacity has a nonlinear relationship to crosslink density that is a function of the crosslinker chemistry. It was demonstrated that by changing the crosslinker chemistry from

heterofunctional to homofunctional a maximum binding capacity of >100 mg/mL could be achieved at an NCD of 0.5. In contrast, the heterofunctional crosslinker demonstrated a decrease in binding capacity as the NCD increases. The optimum membrane formulation was then used for the salt tolerance and dynamic binding measurements. In these measurements, membrane 54H demonstrated consistent binding (>90% of maximum binding) up to 100 mM added salt in 50 mM TRIS buffer. The dynamic binding measurements revealed a flowrate dependent regime while operating at low flowrates (2-4 MV/min). Once the flowrate surpassed 8 MV/min the DBC plateaued and the dependence on flowrate was lost. The first regime at low flowrates demonstrated a flowrate dependence similar to that seen in resin chromatography. In addition, the DBC measurements validated membrane salt tolerance under flow with >90% of the binding capacity maintained up to 100 mM NaCl added at all flowrates tested. Recommendation for future research are discussed in chapter 6.

References

(1) Ghosh, R. Protein Separation Using Membrane Chromatography: Opportunities and Challenges. J. Chromatogr. A 2002, 952 (1), 13–27. https://doi.org/10.1016/S0021-9673(02)00057-2.

(2) Madadkar, P.; Wu, Q.; Ghosh, R. A Laterally-Fed Membrane Chromatography Module. J. Membr. Sci. 2015, 487, 173–179. https://doi.org/10.1016/j.memsci.2015.03.056.

(3) Bhut, B. V.; Wickramasinghe, S. R.; Husson, S. M. Preparation of High-Capacity, Weak Anion-Exchange Membranes for Protein Separations Using Surface-Initiated Atom Transfer Radical Polymerization. J. Membr. Sci. 2008, 325 (1), 176–183. https://doi.org/10.1016/j.memsci.2008.07.028.

(4) Bhut, B. V.; Husson, S. M. Dramatic Performance Improvement of Weak Anion-Exchange Membranes for Chromatographic Bioseparations. J. Membr. Sci. 2009, 337 (1), 215–223. https://doi.org/10.1016/j.memsci.2009.03.046.

(5) Sun, L.; Dai, J.; Baker, G. L.; Bruening, M. L. High-Capacity, Protein-Binding Membranes Based on Polymer Brushes Grown in Porous Substrates. Chem. Mater. 2006, 18 (17), 4033–4039. https://doi.org/10.1021/cm060554m.

(6) Fischer-Frühholz, S.; Zhou, D.; Hirai, M. Sartobind STIC® Salt-Tolerant Membrane Chromatography. Nat. Methods 2010, 7 (12), 12–13.

(7) Orr, V.; Zhong, L.; Moo-Young, M.; Chou, C. P. Recent Advances in Bioprocessing Application of Membrane Chromatography. Biotechnol. Adv. 2013, 31 (4), 450–465. https://doi.org/10.1016/j.biotechadv.2013.01.007.

(8) Keating, J. J.; Imbrogno, J.; Belfort, G. Polymer Brushes for Membrane Separations: A Review. ACS Appl. Mater. Interfaces 2016, 8 (42), 28383–28399. https://doi.org/10.1021/acsami.6b09068.

(9) Riordan, W.; Heilmann, S.; Brorson, K.; Seshadri, K.; He, Y.; Etzel, M. Design of Salt-Tolerant Membrane Adsorbers for Viral Clearance. Biotechnol. Bioeng. 2009, 103 (5), 920–929. https://doi.org/10.1002/bit.22314.

(10) Fan, J.; Luo, J.; Chen, X.; Wan, Y. Facile Preparation of Salt-Tolerant Anion-Exchange Membrane Adsorber Using Hydrophobic Membrane as Substrate. J. Chromatogr. A 2017, 1490, 54–62. https://doi.org/10.1016/j.chroma.2017.02.016.

(11) Han, X.; Hong, T.; Lutz, H.; Becerra-Arteaga, A.; Blanchard, M.; Zhao, X.; Hewig, A.; Natarajan, V. Performance of a Salt-Tolerant Membrane Adsorber in Flow-through Mode. BioProcess Int 2013, 11 (2), 28–39.

(12) Champagne, J.; Balluet, G.; Gantier, R.; Toueille, M. "Salt Tolerant" Anion Exchange Chromatography for Direct Capture of an Acidic Protein from CHO Cell Culture. Protein Expr. Purif. 2013, 89 (2), 117–123. https://doi.org/10.1016/j.pep.2013.03.005.

(13) Woo, M.; Khan, N. Z.; Royce, J.; Mehta, U.; Gagnon, B.; Ramaswamy, S.; Soice, N.; Morelli, M.; Cheng, K.-S. A Novel Primary Amine-Based Anion Exchange Membrane Adsorber. J. Chromatogr. A 2011, 1218 (32), 5386–5392. https://doi.org/10.1016/j.chroma.2011.03.068.

(14) Chen, G.; Umatheva, U.; Alforque, L.; Shirataki, H.; Ogawa, S.; Kato, C.; Ghosh, R. An Annular-Flow, Hollow-Fiber Membrane Chromatography Device for Fast, High-Resolution Protein Separation at Low Pressure. J. Membr. Sci. 2019, 590, 117305. https://doi.org/10.1016/j.memsci.2019.117305.

(15) Qian, X.; Fan, H.; Wang, C.; Wei, Y. Preparation of High-Capacity, Weak Anion-Exchange Membranes by Surface-Initiated Atom Transfer Radical Polymerization of Poly(Glycidyl Methacrylate) and Subsequent Derivatization with Diethylamine. Appl. Surf. Sci. 2013, 271, 240–247. https://doi.org/10.1016/j.apsusc.2013.01.167.

Chapter 4

DESIGN OF POLYMER-CERAMIC COMPOSITES FOR MEMBRANE CHROMATOGRAPHY

The work presented in this chapter was done in collaboration with Noriaki Arai and Laura Quinn. N. Arai and L. Quinn fabricated and analyzed freeze-cast ceramics. O. Bateman synthesized the polymer solution with *in situ* generated functional particles, performed the phase separation micromoulding, and conducted the BSA binding experiments. N. Arai and O. Bateman performed SEM imaging. N. Arai also carried out the permeability measurements.

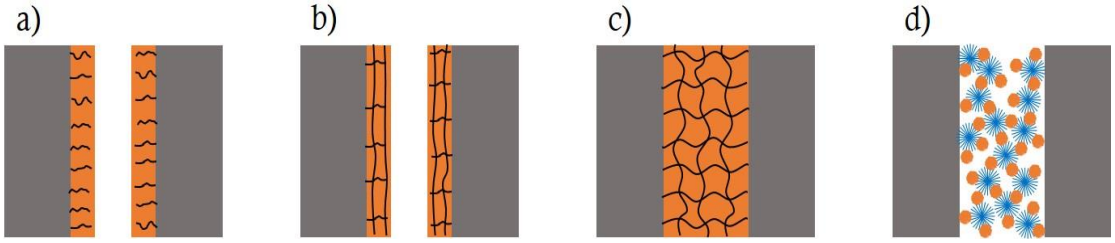

Figure 4.1: Composite membranes consisting of a porous support and a hydrogel comprised of a) linear or b) crosslinked polymer chains, c) pore-filling polymer network, and d) microgels supported by structural polymer. This is a modified figure from Reference 1.

4.1 Introduction

Up to this point we have considered the mixed-matrix membranes with *in situ* generated functional particles as free standing or on top of a nonwoven support. However, as we have investigated higher particle loadings and lower crosslinker concentrations, the material has shown signs of losing its mechanical stability and uniformity on length scales >1 mm. The decreasing mechanical integrity stems from the intrinsic properties of the functional microgels. The PEI microgels are a subset of hydrogels, a class of soft matter materials that are comprised of hydrophilic polymer networks that swell, but do not dissolve, in the presence of water. The intrinsic properties of hydrogels stemming from their unique composition provide both improved functionality and reduced mechanical robustness. As a

result of this dichotomy, several methods have been developed to incorporate hydrogels into composites with ceramics and stiff porous polymers.

Figure 4.1a-c depicts three methods of incorporating functional hydrogels into a porous scaffold that have been well documented in the literature[1–7]. For example, Anuraj and coworkers disclosed a route to integrate a functional hydrogel layer into a porous ceramic using polymer brushes, thereby producing a structure similar to Figure 4.1a. The resulting composite demonstrated efficient capture and purification of proteins from complex mixtures[2]. In another example, Yang et al. investigated the role of crosslink density on the performance of crosslinked polymer chain hydrogels (Fig. 4.1b). They discovered that a lower concentration of crosslinks between polymer chains improved the reaction time of environmentally responsive hydrogels[3]. An example of the pore-filling method shown in Figure 4.1c was demonstrated by Adrus et al. using an *in situ* photopolymerization to grow a hydrogel inside a porous support. The resulting hydrogel mesh size was temperature sensitive, which provided tunable control over the size selectivity of the composite membrane.

Both functionalizing the pore wall and pore-filling are effective methods in combining the mechanical strength of porous supports with the functionality of hydrogels. However, there has been a growing trend in the field emphasizing the use of hydrogel particles, instead of layers, on both the micro and nano scale[8]. The shift in focus stems from the hydrogel particles having faster swelling and stimuli responsive kinetics as well as a 3D porous structure useful in biosensing and bioseparations[9]. Here we discuss a novel method to form composite membranes with stably incorporated microgels as depicted in Figure 4.1d. The composite membrane is fabricated by infiltrating a silicon oxycarbide (SiOC) ceramic scaffold with the polymer dope solution used to fabricate the mixed-matrix membranes in chapters 2 and 3. Following infiltration, the structural polymer in the dope solution is solidified using phase inversion micromoulding. The morphology of the solidified polymer matrix was tailored using the conclusions of chapter 2. The ceramic scaffold, developed by Dr. Arai, is fabricated via freeze casting techniques that provide both mechanical robustness

and a plurality of oriented pores[10]. The composite membrane was characterized using SEM to demonstrate process feasibility. Static and dynamic BSA binding experiments were conducted to probe performance of the composite membranes in bioseparations.

4.2 Experimental methods

4.2.1 Chemicals and materials

Polyvinylidene Fluoride (PVDF) [Kynar 761] was provided by Arkema (King of Prussia, PA). Hyperbranched polyethylenimine (PEI) was procured from Polysciences. Cyclohexane (C6H12), Epichlorohydrin (ECH), 3-Aminopropyltrimethoxysilane (ATMS), Bovine Serum Albumin (BSA), Bis(2-chloroethyl)amine hydrochloride (BCAH), Triethyl Phosphate (TEP), Isopropanol (IPA), Dimethyl sulfoxide (DMSO), and TRIS hydrochloride (TRIS) were purchased from Millipore Sigma. Hydrochloric acid was purchased from EMD Millipore. Polysiloxane (CH3-SiO1.5, Silres® MK Powder) and Geniosil® GF 91 were purchased from Wacker Chemie. All chemicals and materials were used as received. Buffers were prepared using indicated chemicals and distilled water.

4.2.2 Ceramic fabrication

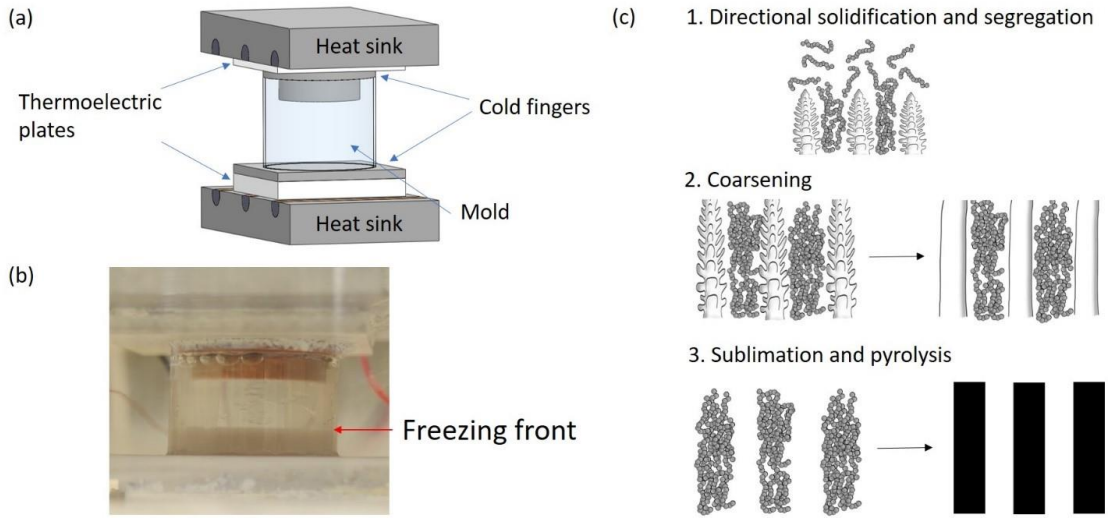

Figure 4.2: Schematic depicting a) freeze casting apparatus, b) sample being freeze cast, c) freeze casting procedure and associated structures.

A polymer solution was prepared by dissolving the polysiloxane preceramic polymer in cyclohexane, with concentration of preceramic polymer of 20 wt.%. Once a homogenized solution was obtained, a cross-linking agent (Geniosil® GF 91) was added in concentrations of 1 wt.% and stirred for 5 minutes and then degassed for 10 min to avoid air bubbles during solidification. The freeze-casting was done by pouring the polymer solution into a glass mold (h = 20 mm, Ø = 25 mm) that was located on a PID-controlled thermoelectric plate. Another thermoelectric was placed on top of the mold to control both freezing front velocity and temperature gradient, a similar configuration as the work by Zeng et al. [11] (Fig. 1). A cold finger with smaller diameter than the mold was inserted into the glass mold such that the created spaces act as reservoir for the solution as the solution shrunk by solidification. The freezing front velocity and temperature gradient were measured by taking pictures every 30 seconds using a camera and intervalometer. The temperature gradient, G was defined by the following equation:

$$G = \frac{T_t - T_f}{d} \tag{4.1}$$

where T_t is the temperature of top cold finger, T_f is the temperature of freezing front and d is the distance between the top cold finger and the freezing front. The temperature of the freezing front was assumed to be at the liquidus temperature of the solution, and the value was taken from the work by Naviroj [12]. All samples were frozen at freezing front velocities of 15 μm/s, and temperature gradients of 2.5 K/mm to maintain homogeneous pore structures.

Once the structure was completely frozen, the isothermal coarsening was initiated by setting the top and bottom thermoelectrics to 4°C. After the structure was coarsened for 3 hours, the sample was re-froze[13]. After the sample was completely frozen, the sample was sublimated in a freeze drier (VirTis AdVantage 2.0) where the solvent crystals were completely removed. After freeze drying, the polymer scaffold was pyrolyzed in argon at 1100 °C for four hours to convert the preceramic polymer into silicon oxycarbide (SiOC).

This resulted in a porosity of ~77%. The pyrolyzed sample was machined into a disk with thickness of ~1.6 mm and diameter of ~13mm prior to infiltration.

Table 4.1: Composition of polymer dope solution and associated Normalized Crosslink Density (NCD). Naming scheme goes as wt.% PEI in the dry polymeric membrane – NCD.

Dope solution	PVDF (g)	PEI (g)	BCAH (g)	DMSO (mL)	NCD
54-0.5	5.91	5	3.1	5	0.5
54-0.25	5.91	5	1.55	2.5	0.25
54-0.125	5.91	5	0.78	1.25	0.125
54-0.0625	5.91	5	0.39	0.625	0.0625
54-0.4	5.91	5	2.5	4	0.4
38-0.4	5.91	2.58	1.28	2	0.4

4.2.3 Polymer Dope Synthesis

The polymer dope synthesis was initiated by adding 5.91 g of PVDF to an empty 3-neck round bottom flask. The flask was then outfitted with an overhead mechanical stirrer and the necessary greased connectors. Next, 30 mL of TEP was added to the flask and then the remaining openings were sealed using rubber septa. The PVDF/TEP mixture was heated to 80 ºC and incubated for 1 hour before the mixing speed was set to 60 rpm. The resulting solution was left to equilibrate overnight. A PEI solution was prepared by adding the mass of PEI indicated in Table 4.1 to a scintillation vial followed by 5 mL of TEP. The mixture was vortexed and shaken until no concentration gradients were visible and then it was left to equilibrate overnight at room temperature. The crosslinker solution was prepared by weighing the required amount of BCAH into a scintillation vial and then adding the corresponding volume of DMSO (Table 4.1). The resulting mixture was incubated overnight at room temperature to fully dissolve the BCAH.

The next day, the reaction flask was purged with N_2 for 7 minutes and the mixing speed was increased to 250 rpm. With the N_2 flow still on, the PEI solution was then added dropwise to the flask using a glass Pasteur pipette over the course of 4 minutes. The resulting solution was left to mix for 5 minutes before adding 0.43 mL of concentrated HCl (37% solution). Following the addition of the HCl, the flask was incubated for 15 minutes at 80 ºC

with the mixing speed maintained at 250 rpm. The crosslinker solution was then added to the flask and the polymerization reaction was allowed to proceed for 4 hours. After the 4-hour reaction time, the flask was put under in-house vacuum for 10 minutes to remove entrapped air. The resulting dope solution was then added to the ceramic using the steps outlined in 4.2.5.

Several polymeric membranes were prepared at wt.% PEI in the dry polymeric membrane – NCD compositions of 54-0.5, 54-0.25, 54-0.125, 54-0.0625 as controls for the static binding measurements. The same steps outlined above were followed until completing the incubation under vacuum. The resulting dope solution was then cast on glass plates at a blade height of 300 μm. The cast membranes were left at room temperature for 30 seconds before being immersed in an isopropanol coagulation bath. After two hours, the solidified membranes were moved to distilled water baths prior to storage.

4.2.4 Surface Functionalization of Ceramic

Prior to adding the polymer dope solution, the ceramic surface was activated and functionalized (Fig. 4.3a) using a procedure derived from prior literature[14–17]. The SiOC scaffold was first immersed and incubated in 1 M NaOH for 90 minutes. It was then washed in water before being incubated in a 0.1 M HCl solution for 30 minutes. The ceramic was then washed in water again, before being dried at 110 ºC for 1 hour. Once the ceramic was dried, it was added to a 2 v% solution of ATMS in isopropanol and incubated for 3 hours at 60 ºC. The sample was then washed thoroughly in water and isopropanol before being cured at 110 ºC for 30 minutes.

Following the curing of the aminosilane layer, the ceramic surface was further functionalized following the two reaction schemes presented in Figure 4.3b. Ceramics prepared using the top route were incubated in an IPA/ECH solution overnight. Following the overnight incubation, the samples were thoroughly washed with IPA and then left to dry at room temperature before the addition of the polymer solution. The resulting surface was

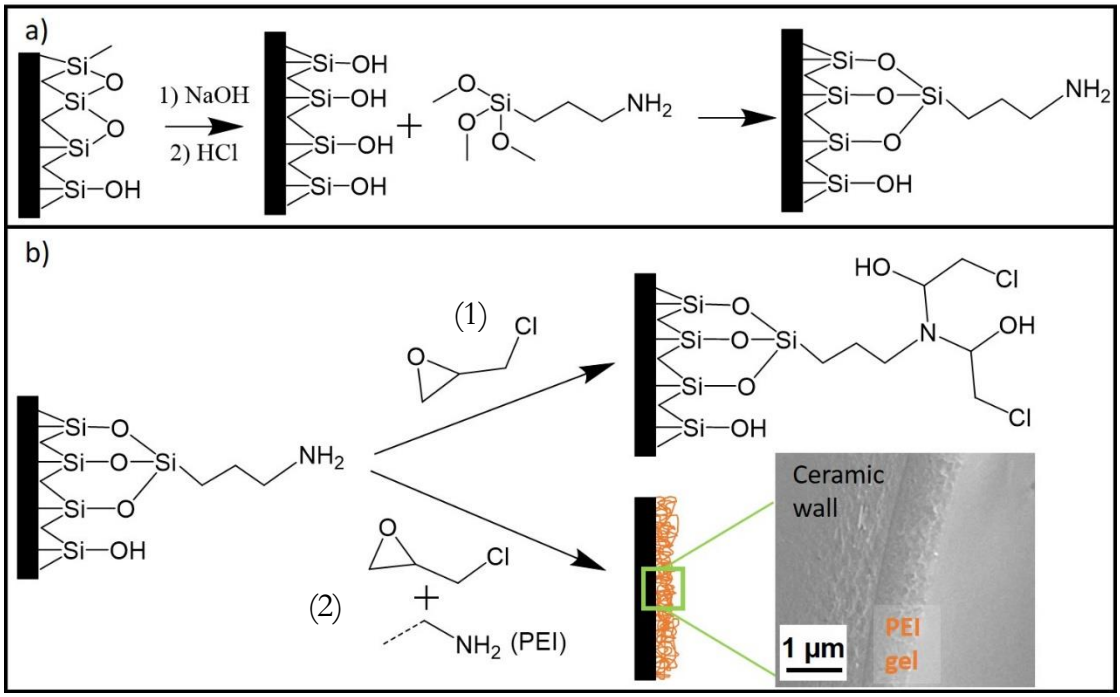

Figure 4.3: Reaction schemes for a) initial functionalization of amine surface terminating with aminosilane linker, b) further surface functionalization using (1) ECH in IPA and (2) ECH+PEI in IPA

expected to be terminated in chloride groups, which would react readily with the primary and secondary amines in the polymer solution.

The second further functionalization route was designed to increase the number of functional groups on the wall available to interact with amines in the PEI microgels. The functionalization proceeded as follows: the functionalization solution was prepared by dissolving PEI with IPA at a molar ratio of 1:37.4, respectively. Ten minutes before adding the solution to the ceramic, ECH was added to the solution at a molar ratio of 1 mole PEI for 16.5 moles ECH – corresponding to 1.1 ECH molecules for every available amine. This ratio was chosen to minimize the crosslinking between PEI molecules and thereby maximize the number of reactive sites. The ceramic was incubated in the IPA/PEI/EHC solution overnight at room temperature. After the overnight incubation, DMSO was added to the vial and the resulting solution was heated to 80 ºC for 1 hour to remove the leftover reactants and unbound products. The sample was then washed with IPA and dried at room temperature for one hour prior to the addition of the polymer dope solution.

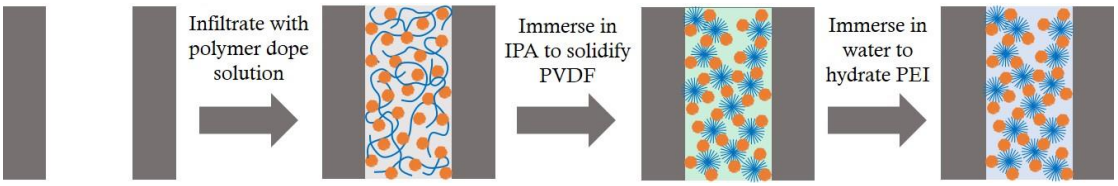

Figure 4.4: A visual depiction of the phase inversion micromoulding process.

4.2.5 Phase Inversion Micromoulding

The phase inversion micromoulding process shown in Figure 4.4 was used for both neat ceramic samples and ceramics functionalized using the pathways described above. The ceramic scaffold was loaded into the infiltration device and the polymer dope solution was injected using a syringe pump. The solution was pumped at a rate of 100 µL/min until the ceramic and infiltration device were filled. The device was then incubated at 80 ºC for 1 hour for both the functionalized and the neat ceramic samples. Following the incubation, the samples were removed from the infiltration device and placed in IPA for an overnight incubation. The following day, the samples were moved to water baths to remove trace solvent and IPA in preparation for BSA binding characterization.

4.2.6 Membrane properties characterization

4.2.6.1 SEM

The microstructure of ceramic scaffolds and polymer/ceramic composites were observed using a field emission scanning electron microscope (FE SEM – Zeiss 1550 VP). In preparation for imaging, the samples were dried at 70°C overnight. To prepare the cross-sectional view, the membranes were broken by hand at ambient conditions. The surfaces and cross-sections of interest were then coated with a Pt/Pd conductive layer (10 nm) using a sputter coater and then imaged.

4.2.6.2 Protein adsorption studies

BSA was used as the model protein in both static and dynamic binding measurements. Initial tests were done using BSA in distilled water at a concentration of 2

mg/mL. To measure the static binding of the polymeric membrane references, a membrane with a known volume was immersed in a 2 mg/mL BSA solution and gently mixed for 48 hours. The absorbance of the solution was then measured using an Agilent 8453 *UV/vis* and the reported absorbance at 280 nm was used to determine the concentration of BSA in the solution. The mass of BSA bound was then determined using a mass balance.

A similar process was used to measure the static binding capacity (SBC) of the composite membranes. The samples were immersed in a 2 mg/mL BSA solution and gently rocked for 48 hours. The absorbance was then measured and the binding capacity calculated before the samples were rocked for another 72 hours. The absorbance was then measured again and the binding capacity calculated. The addition of the second absorbance measurement was to account for the increased thickness and reduced mass transfer in the composites. The initial experiments for comparison to the polymeric membranes used BSA dissolved in H_2O, all subsequent measurements used BSA dissolved in 50 mM TRIS.

Dynamic binding measurements using 2 mg/mL BSA in 50 mM TRIS buffer were conducted using composites with formulations of 54-0.25 and 38-0.4. To run the measurement, the sample was first loaded into a Swinney filter holder (Pall Corp.) and was equilibrated using 50 mM TRIS buffer. The BSA solution was then introduced via a syringe pump to the device at a rate of 150 µL/min (or 2 membrane volumes/min). The filtrate was analyzed with time-resolved measurements on the Agilent 8453 *UV/vis*. The 10% breakthrough curve method, as described in Ch. 3, was used to determine the dynamic binding capacity.

4.3 Results and discussion

4.3.1 Phase inversion micromoulding feasibility

Figure 4.5 shows SEM micrographs of the cross-section and surfaces of the ceramic scaffold and composite membranes with different surface functionality. The longitudinal cross-sectional image of the neat ceramic scaffold, Fig. 4.5a, shows the highly oriented pores

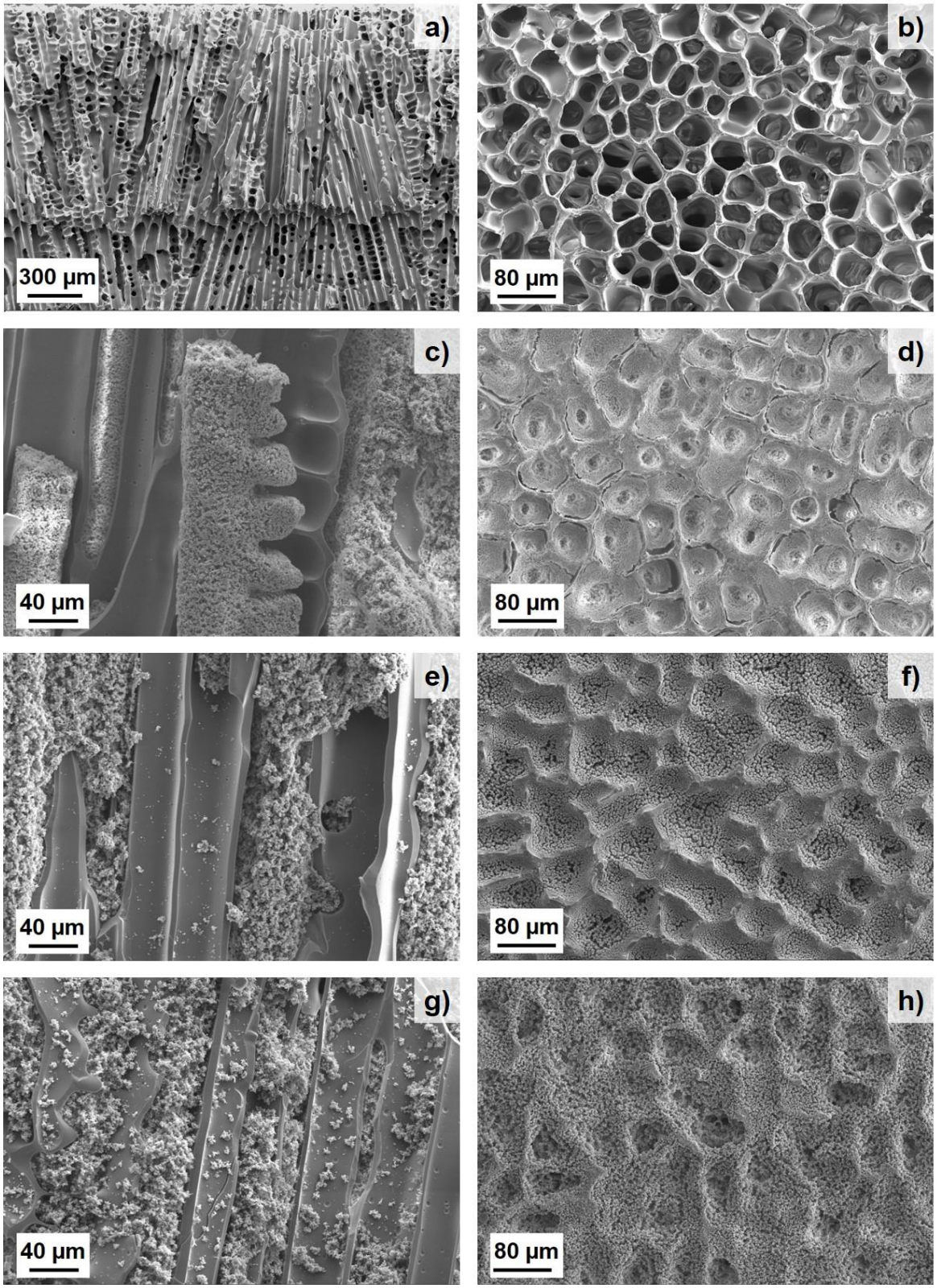

Figure 4.5: SEM micrographs showing the following: neat ceramic a) cross-section & b) surface, composite without surface functionality c) cross-section & d) surface, composite with ECH functionality e) cross-section & f) surface, and composite with PEI gel layer g) cross-section & h) surface.

that transverse the entire membrane. The corresponding surface (perpendicular to the freeze-casting direction), Fig 4.5b, demonstrates the morphology of the oriented pores as well as the average pore diameter of 20 μm. The composite presented in Figure 4.5c&d was infiltrated without modifying the surface of the ceramic. In panel c, there is a segment of the polymer matrix in the middle of the micrograph that has a morphology that closely matches the contours of the nearby ceramic pore wall. It is also noteworthy that the ceramic surfaces that are visible are all bare. In the surface view from panel d the pores are mostly filled with the polymer matrix, but there are many cases where there is a debonded interface between the polymer matrix and one side of the pore.

The composite presented in Figure 4.5e&f had the surface modified using reaction (1) from Figure 4.3b prior to the infiltration and phase inversion micromoulding. The polymer matrix once again fills the pores in panel e and the ceramic walls that are visible are lightly decorated in microparticles from the polymer matrix. Panel f shows that the ceramic pores are completely filled and there are no visible gaps between the polymer matrix and the pore wall. The composite presented in panels g& h of Figure 4.5 had the surface modified using reaction (2) from Figure 4.3b, producing a functional PEI gel layer prior to infiltration and phase inversion micromoulding. The polymer matrix fills the pores in panel g and the ceramic walls that are visible are decorated with a higher density of microparticles/polymer matrix than panel e. Panel h shows that the ceramic pores are once again completely filled and there are no visible gaps between the polymer matrix and the pore wall.

The observations of the behavior of the polymer matrix in panels c and d, provide several key insights on phase inversion micromoulding and how to stably integrate the mixed-matrix membrane with the ceramic scaffold. The match between the morphology of the polymer matrix and the contours of the scaffold wall in panel c indicates that phase inversion micromoulding is capable of replicating features on the order of 10 μm. However, the phase inversion process does not seem to prevent debonding of the polymer matrix from the pore wall as seen in both the bare pore walls in panel c and the gaps in between the polymer matrix and ceramic scaffold in panel d. While there is a significant probability that

the gaps between the polymer matrix and ceramic scaffold in panel d are due to the drying process, the presence of any gaps or debonding in the wet state could lead to channeling and result in poor membrane performance. Therefore, it was decided to covalently bind the polymer matrix to the ceramic scaffold to suppress debonding.

The surfaces in panels f&h show pores that are filled with no indications of gaps or debonding from the ceramic scaffold. Similarly, the cross-sectional images in panels e&g both exhibit ceramic walls that are decorated with PEI particles and small sections of the polymer matrix. However, the density of decorating material on panel e is less than half of what is observed in panel g. It was concluded that the decorating material in panel e stems from functionalizing the surface because of the complete absence of decorating particles when the ceramic surface has not been modified (Fig. 4.5c). The discrepancy in the density of adhered PEI particles and polymer matrix is attributed to the difference in the number of reactive sites available from the surface functionalization.

Consider first a single pore that is assumed to be a perfect cylinder with diameter of 20 μm and height of 1.6 mm. The corresponding surface area and volume are $1 * 10^5$ μm^2 and $5* 10^5$ μm^3, respectively. Assuming a monolayer density of 4 ATMS molecules/nm^2 on silicon dioxide[18] and that only 50% of the SiOC ceramic scaffold is silicon dioxide[19], there are approximately $3 * 10^{-13}$moles of ATMS per pore. Using reaction (1) from Figure 4.3b to further functionalize the surface and assuming any side reactions of ECH may be ignored at room temperature, there are $6 * 10^{-13}$moles of halide per pore in the ceramic scaffold available to react with the amines in the polymer solution. This concentration should be considered an upper bound due to secondary reactions, such as the halide on an already bound ECH molecule reacting with a nearby amine, reducing the actual number of halides.

Using reaction (2) from Figure 4.3b as the second functionalization step produces a conformal PEI gel layer with an average thickness of 500 nm. Following a similar analysis as above, the interface of the gel layer is assumed to form a perfect cylinder with a diameter of 19 microns and height of 1.6 mm. The corresponding surface area and volume are $0.96 * 10^5$ μm^2 and $4.5 * 10^5$ μm^3, respectively. Assuming that the concentration of halides may

be approximated as a monolayer of ECH that covers the entire gel layer, the monolayer density was estimated to be 8 ECH molecules/nm^2 from the topological polar surface area of 0.125 nm^2/ECH molecule[20]. The resulting concentration of halides is approximately $13 * 10^{-13}$ moles of halide per pore. Although the calculated halide concentrations for the two reaction sequences are of the same order of magnitude, the value from reaction (1) is an upper bound that ignores a multitude of side and secondary reactions. In contrast, the value calculated for reaction (2) should be considered a lower bound due to TEP swelling the PEI molecules at the gel interface. The swelling of the interfacial region leads to more reactive sites being accessible further improving the bonding between the gel layer and the PEI microgels in the polymer solution. Due to the superior adhesion between the polymer matrix and ceramic scaffold when using the PEI gel layer, all composites used for BSA binding experiments were fabricated with a PEI gel layer unless otherwise indicated.

4.3.2 Protein binding and the role of the PEI gel layer

Figure 4.6a shows the static binding capacities, in H_2O, of both the composite and polymeric membranes as a function of crosslink density. The composite membranes have little fluctuation in binding capacities for NCDs ≤0.25, with a drop in the reported binding capacity when the NCD is increased to 0.5. The polymeric membranes show the opposite behavior with excellent binding at NCD of 0.5 and very low binding at NCDs ≤0.25. The

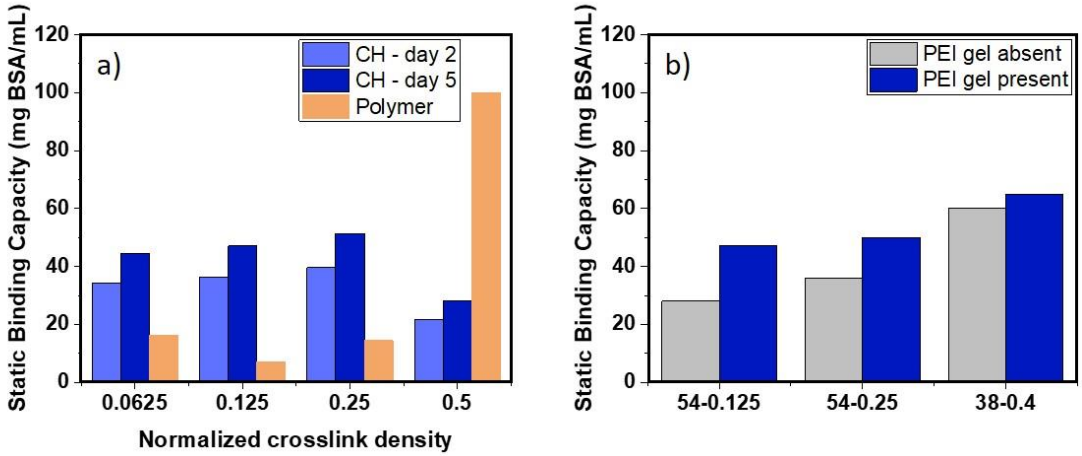

Figure 4.6: Plots of static binding capacities for a) both composite (CH) and polymeric membranes with 54% PEI loading using 2 mg/mL BSA in H_2O and b) composite membranes using 2 mg/mL BSA in 50 mM TRIS at pH 7.4

binding capacities of the composite membranes are also presented at two different time points. The first reported SBC was measured after 48 hours and for all compositions was lower than the second reported SBC measured after 120 hours. Figure 4.6b shows the static binding capacity, in TRIS buffer, of composite membranes with the same polymer composition and different ceramic surface functionality (with PEI gel layer or not functionalized ceramic). The difference in binding capacity between the two conditions decreases as the crosslink density is increased.

The superior performance of the composite membranes at low crosslink densities validated our hypothesis that integrating the dope solution with a ceramic scaffold would broaden our operating space. Surprisingly the benefit of the ceramic did not come from the mechanical failure of PVDF, but rather from the failure to form the PEI microgels. Table 4.2 outlines the average number of bonds (not accounting for the different amine reactivity or steric hindrance) a single PEI molecule would have at each crosslink density. Note that at a crosslink density of 0.0625 there is less than 1 bond per PEI molecule on average, indicating that not all of the PEI that was added to the dope solution initially will be polymerized. As a result, there is a fraction of the PEI molecules that either do not react or form small oligomers. When the solution is cast as a polymeric membrane, the casting solution is immersed in IPA and any unbound PEI – in the form of single molecules or low MW oligomers – is able to diffuse out of the dope solution into the nonsolvent bath, or into the following water bath. The resulting membrane has a lower concentration of amines to interact with BSA and therefore has a lower binding capacity.

Table 4.2: Average number of bonds per PEI molecule not accounting for differences in reactivity of amines or steric hindrance.

NCD	Bonds/PEI molecule
0.5	4.1
0.4	3.3
0.25	2.1
0.125	1.0
0.0625	0.5

Next, consider a membrane composite prepared using the same dope solution as described for the polymeric membrane case. Upon infiltrating the ceramic scaffold with the polymer solution there are a number of low molecular weight PEI molecules in the solution. However, prior to phase inverting the dope solution in the ceramic there is sufficient time

given to react the functional microgels in the dope with the PEI gel layer on the wall. During this time period, the unbound PEI in the dope solution may react with the exposed functional groups on the wall. The newly bound PEI molecules will not be removed during the phase inversion and subsequent washing steps thereby increasing the number of BSA binding sites in comparison to the polymeric membrane. The role of the gel layer in capturing unbound PEI was validated, shown in Figure 4.6b, where a comparison between composite membranes prepared using the same dope solution to infiltrate ceramics both with and without the PEI gel layer. At lower crosslink densities when the concentration of unbound PEI is higher, the composite prepared without the PEI gel layer is 40% lower. At higher crosslink densities where the concentration of unbound PEI should be lower, the composite prepared without the PEI gel layer is only 10% lower.

4.3.3 PEI swelling at high NCD

The BSA binding behavior at NCD of 0.5 in Figure 4.6a was also surprising because the binding capacity of the composite was less than 30% of the capacity of the corresponding polymer membrane. The composite was expected to have approximately 70% of the polymeric membrane SBC at NCD 0.5, with the other 30% accounting for the volume occupied by the ceramic scaffold as well as the amines consumed by covalently bonding the polymer matrix to the ceramic scaffold. The large difference between the predicted and actual SBCs is caused by the swelling of PEI microgels in a constrained volume. Figure 4.7 presents a visual representation of PEI swelling in a constrained volume under three different

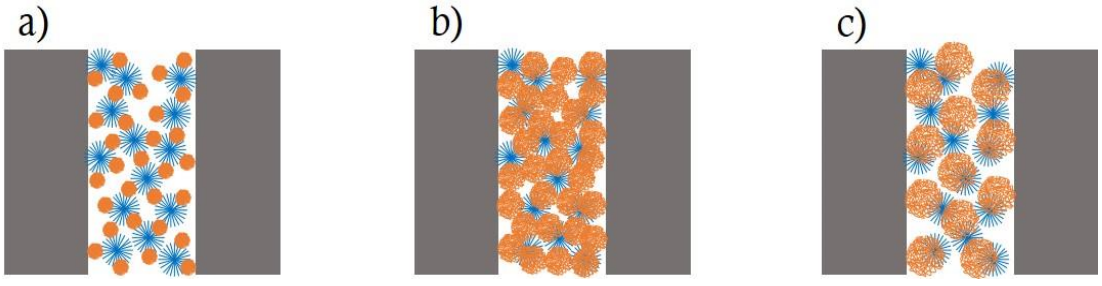

Figure 4.7: Depiction of composite membranes with PEI microgels in a) an unswollen state, b) a semi-swollen state physically restricted by the pore walls and other microgels, c) fully swollen state under with no external restrictions

conditions. Pictures demonstrating the volume change of the polymeric membrane due to microgel swelling are shown in Figure A.8.

In panel a of Figure 4.7, the pore is filled with a nonswelling liquid thereby leaving the PEI microgels in an unswollen state. This condition is reminiscent of the behavior of the PEI particles in IPA following the phase inversion micromoulding. Panel b depicts microgels that are in water, but are only able to reach a semi-swollen state due to physical interference by the pore wall and other nearby microgels. The semi-swollen microgels are detrimental to BSA binding through limiting both the number of available binding sites and the mass transfer through the ceramic pore. Panel c also depicts microgels that are in water; however, these microgels are at a lower concentration and as a result they do not interact with other microgels allowing them to reach the thermodynamic swelling equilibrium. The fully swollen PEI particles have the largest number of available binding sites due to the reduction in interference. As a result, the highest PEI concentration that still enables the microgels to be fully swollen is the optimum condition for BSA binding. The composites with dope compositions of 54-0.4 and 38-0.4 were 54% and 38% PEI with the same crosslink density. The reported SBC of the 54-0.4 and 38-0.4 composites were 35 and 65 mg BSA/mL respectively, with the latter being the highest static binding capacity of the composite membranes investigated in this study.

4.3.4 Dynamic binding measurements

Figure 4.8 presents representative breakthrough curves for an empty SiOC ceramic scaffold, composite membranes prepared using 54 wt.% PEI and NCD of 0.25, and composite membranes prepared using 38 wt.% PEI and NCD of 0.4. Using the 10% breakthrough method described in Ch. 3, BCs of 19 mg/mL and 61 mg/mL were calculated for 54-0.25 and 38-0.4 respectively. The reduction in binding capacity of 54-0.25 between the static (51 mg/mL) and dynamic (19 mg/mL) experiments is 63%, which is higher than the reduction of 25% in binding observed when using just the polymer membranes with 54 wt.% PEI and NCD of 0.5. This discrepancy is ascribed to the contributions of “unbound” PEI in the dope

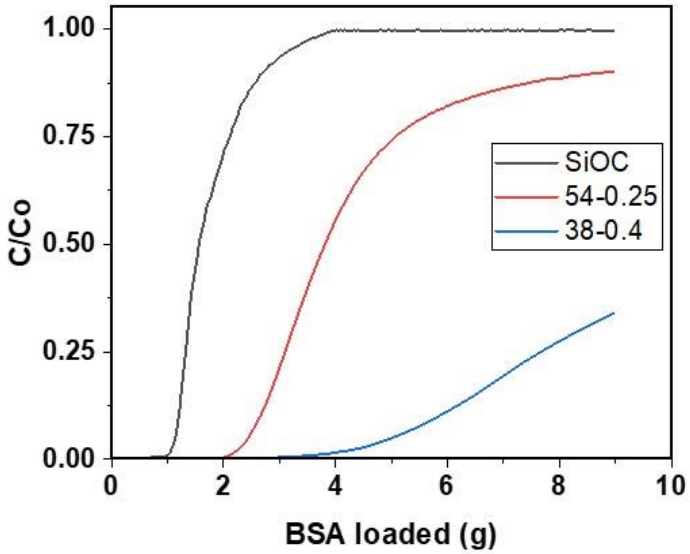

Figure 4.8: BSA binding breakthrough curves of an SiOC scaffold, a 54 wt.% PEI with NCD 0.25 composite membrane, and a 38 wt.% PEI with NCD 0.4 composite membrane.

solution that is captured by the PEI gel layer before it can diffuse out of the ceramic. The PEI molecules captured by the wall readily contribute to the static binding capacity due to the additional time provided for BSA to reach the pore wall. In a dynamic binding setting however, only a small portion of the fluid has time to interact with the wall. The rest of the protein solution flows through the polymer matrix, which has a lower than expected PEI concentration. The lower PEI concentration in the polymer matrix leads to rapid saturation of the available binding sites resulting in a low binding capacity. In contrast, the 38-0.4 composite exhibits a DBC that is only 7% less than its SBC. This small reduction indicates that the method used to test the static binding capacity of the 38-0.4 membrane was most likely insufficient to fully saturate all the available binding sites.

The larger DBC of 38-0.4 stems from the optimization of PEI loading and crosslink density. At higher PEI concentrations the gel swells in water to such an extent that it restricts mass transfer through the composite. At lower PEI concentrations mass transfer through the composite is uninhibited, but there are fewer available binding sites leading to lower binding capacities. Similarly, as outlined previously, at low crosslink densities PEI has a higher

chance to diffuse out of the composite during the casting process. Whereas at high crosslink densities, the PEI microgels are tightly crosslinked leading to various forms of steric hindrance and reduced interactions between the binding sites and the molecules of interest. The 38-0.4 composite sits in a "Goldilocks Zone" where the different interactions balance each other allowing for high binding capacity with uninhibited mass transfer.

4.4 Conclusions

Here we have documented a novel method to incorporate functional microgels into a ceramic scaffold via surface functionalization and phase inversion micromoulding. The resulting composite was characterized using SEM analysis and BSA binding measurements. The SEM characterization demonstrated that functionalizing the ceramic surface with a reactive conformal PEI gel layer improved the adherence of the polymer matrix to the pore wall in the dry state. The PEI gel layer was also shown to have a beneficial impact on BSA binding at low crosslink densities, with the SBCs of the composite membranes being more than double the binding of the corresponding polymeric membrane. The relationship between PEI concentration, swelling, and BSA binding was also investigated. At high PEI concentrations, the swelling of the microgels led to lower SBC and membrane permeability. Reducing the PEI concentration in the dope solution to account for swelling resulted in the highest reported static binding capacity of 65 mg BSA/mL. Suggestions for future experiments are discussed in Chapter 6.

References

(1) Yang, Q.; Adrus, N.; Tomicki, F.; Ulbricht, M. Composites of Functional Polymeric Hydrogels and Porous Membranes. *J. Mater. Chem.* **2011**, *21* (9), 2783–2811. https://doi.org/10.1039/C0JM02234A.

(2) Anuraj, N.; Bhattacharjee, S.; Geiger, J. H.; Baker, G. L.; Bruening, M. L. An All-Aqueous Route to Polymer Brush-Modified Membranes with Remarkable Permeabilites and Protein Capture Rates. *J. Membr. Sci.* **2012**, *389*, 117–125. https://doi.org/10.1016/j.memsci.2011.10.022.

(3) Ulbricht, M.; Yang, H. Porous Polypropylene Membranes with Different Carboxyl Polymer Brush Layers for Reversible Protein Binding via Surface-Initiated Graft Copolymerization. *Chem. Mater.* **2005**, *17* (10), 2622–2631. https://doi.org/10.1021/cm0485714.

(4) Adrus, N.; Ulbricht, M. Novel Hydrogel Pore-Filled Composite Membranes with Tunable and Temperature-Responsive Size-Selectivity. *J. Mater. Chem.* **2012**, *22* (7), 3088–3098. https://doi.org/10.1039/C2JM15022K.

(5) Ulbricht, M. Advanced Functional Polymer Membranes. *Polymer* **2006**, *47* (7), 2217–2262. https://doi.org/10.1016/j.polymer.2006.01.084.

(6) Liu, J.; Qu, S.; Suo, Z.; Yang, W. Functional Hydrogel Coatings. *Natl. Sci. Rev.* **2021**, *8* (2). https://doi.org/10.1093/nsr/nwaa254.

(7) Huang, R.; Kostanski, L. K.; Filipe, C. D. M.; Ghosh, R. Environment-Responsive Hydrogel-Based Ultrafiltration Membranes for Protein Bioseparation. *J. Membr. Sci.* **2009**, *336* (1), 42–49. https://doi.org/10.1016/j.memsci.2009.03.002.

(8) Vermonden, T.; Klumperman, B. The Past, Present and Future of Hydrogels. *Eur. Polym. J.* **2015**, *72*, 341–343. https://doi.org/10.1016/j.eurpolymj.2015.08.032.

(9) Kim, J. J.; Park, K. Smart Hydrogels for Bioseparation. 8.

(10) Arai, N. Freeze Casting of Ceramics: Pore Design from Solidification Principles. PhD Thesis, California Institute of Technology, 2021.

(11) Zeng, X.; Arai, N.; Faber, K. T. Robust Cellular Shape-Memory Ceramics via Gradient-Controlled Freeze Casting. *Adv. Eng. Mater.* **2019**, *21* (12), 1900398. https://doi.org/10.1002/adem.201900398.

(12) Maninpat Naviroj. Silicon-Based Porous Ceramics via Freeze Casting of Preceramic Polymers (Ph.D. Thesis), Northwestern University, 2017.

(13) Arai, N.; Stan, T.; Macfarland, S.; Voorhees, P. W.; Muyanja, N. S.; Shahani, A. J.; Faber, K. T. Coarsening of Dendrites in Solution-Based Freeze-Cast Ceramic Systems. *Acta Mater.* **2021**, *215*, 117039. https://doi.org/10.1016/j.actamat.2021.117039.

(14) Rostami, S.; Talebpour, Z.; Yeganeh, H. Preparation, Optimization and Application of Poly(Ethylene Glycol)Methyl Ether Methacrylate/Urethane Methacrylate as a New Polar Phase for Stir Bar Sorptive Extraction. *Anal. Methods* **2014**, *6* (19), 7722–7732. https://doi.org/10.1039/C4AY01113A.

(15) Acres, R. G.; Ellis, A. V.; Alvino, J.; Lenahan, C. E.; Khodakov, D. A.; Metha, G. F.; Andersson, G. G. Molecular Structure of 3-Aminopropyltriethoxysilane Layers Formed on Silanol-Terminated Silicon Surfaces. *J. Phys. Chem. C* **2012**, *116* (10), 6289–6297. https://doi.org/10.1021/jp212056s.

(16) Chauhan, A. K.; Aswal, D. K.; Koiry, S. P.; Gupta, S. K.; Yakhmi, J. V.; Sürgers, C.; Guerin, D.; Lenfant, S.; Vuillaume, D. Self-Assembly of the 3-Aminopropyltrimethoxysilane Multilayers on Si and Hysteretic Current–Voltage Characteristics. *Appl. Phys. A* **2008**, *90* (3), 581–589. https://doi.org/10.1007/s00339-007-4336-7.

(17) Zhu, M.; Lerum, M. Z.; Chen, W. How To Prepare Reproducible, Homogeneous, and Hydrolytically Stable Aminosilane-Derived Layers on Silica. *Langmuir* **2012**, *28* (1), 416–423. https://doi.org/10.1021/la203638g.

(18) Karade, V. C.; Sharma, A.; Dhavale, R. P.; Dhavale, R. P.; Shingte, S. R.; Patil, P. S.; Kim, J. H.; Zahn, D. R. T.; Chougale, A. D.; Salvan, G.; Patil, P. B. APTES Monolayer Coverage on Self-Assembled Magnetic Nanospheres for Controlled Release of Anticancer Drug Nintedanib. *Sci. Rep.* **2021**, *11* (1), 5674. https://doi.org/10.1038/s41598-021-84770-0.

(19) Saha, A.; Raj, R.; Williamson, D. L. A Model for the Nanodomains in Polymer-Derived SiCO. *J. Am. Ceram. Soc.* **2006**, *89* (7), 2188–2195. https://doi.org/10.1111/j.1551-2916.2006.00920.x.

(20) Khlebtsov, B. N.; Khanadeev, V. A.; Burov, A. M.; Le Ru, E. C.; Khlebtsov, N. G. Reexamination of Surface-Enhanced Raman Scattering from Gold Nanorods as a Function of Aspect Ratio and Shape. J. Phys. Chem. C 2020, 124 (19), 10647–10658.

Chapter 5

SIZE-BASED CAPTURE OF BACTERIA VIA DENDRITIC FREEZE-CAST CERAMIC MEMBRANES

The work presented in this chapter was done in collaboration with Noriaki Arai, Laura Quinn, Katherine Faber, Priya Chittur, and Lealia Xiong. O. Bateman designed the experiments, ran flow-through measurements and analyzed the results. N. Arai and L. Quinn fabricated and characterized the dendritic ceramics. N. Arai and O. Bateman performed SEM imaging of the ceramics following flow-through experiments. P. Chittur provided the protocol for culturing *E. coli* and instructions on appropriate practices when working with biological samples. L. Xiong provided an mWasabi-expressing strain of *E. coli* in glycerol stock solution. Professor Faber co-advised O. Bateman on this project.

5.1 Introduction

Sepsis is a life-threatening medical emergency that arises when the body's response to an infection causes injury to itself. There are more than 18 million diagnosed cases of sepsis a year worldwide with an average of 1,400 patients dying daily. Rapid diagnosis and treatment is essential to a patient's recovery, with very few patients surviving if undiagnosed after 36 hours[1] (Figure 5.1). Typical treatment for sepsis starts with broad-spectrum antibiotics until the pathogen is identified using methods such as blood cultures[2], at which time a more effective treatment plan is put in place. Although the use of broad-spectrum antibiotics is essential to improving patients' survival rate prior to pathogen detection, they also carry the hidden danger of contributing to rising levels of antibiotic-resistant pathogens[3]. Therefore, it is critical for both the patient and the community at large to identify the pathogen causing sepsis quickly. Unfortunately, the current gold standard in pathogen identification, blood cultures, takes anywhere from 16 to 96+ hours – assuming that the pathogen is cultivable[4].

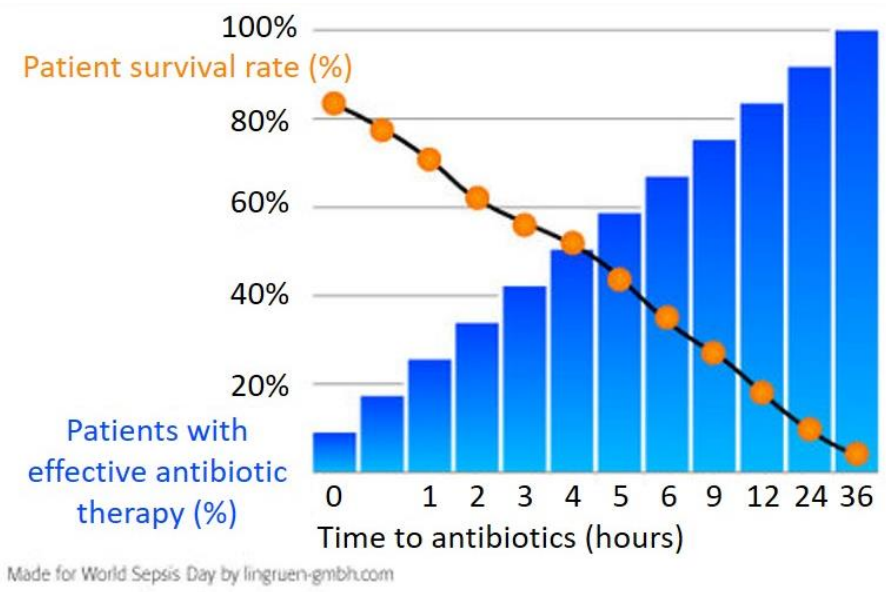

Figure 5.1: Graph showing the patient survival rate and patients with effective antibiotic therapy as a function of time[1]

Although rapid detection of low concentrations of pathogens in a complex fluid such as blood presents many challenges, recent work in point-of-care diagnostics has addressed part of the problem through the development of digital quantitative detection. Schoepp et al. developed a digital antimicrobial susceptibility test (dAST) that determined susceptibility of isolates from urinary tract infections in under 15 minutes[3]. A critical step in dAST was the use of targeted amplification to increase the signal from very low concentrations of pathogen DNA, thereby allowing digital detection. A study by Schlappi et al. used a similar *in situ* amplification technique in combination with flow-through capture to detect zeptomolar concentrations of pathogen DNA from several milliliters of MES (2-(N-morpholino)ethanesulfonic acid) buffer[5]. Both studies demonstrated capabilities for rapid detection of pathogens at low concentrations; however, there is still a need to develop a method that will quickly (<30 minutes) isolate and concentrate pathogens from complex solutions into a small volume for later detection. The method must also demonstrate high capture efficiency in order to have a sensitivity comparable to that of blood cultures, which are able to detect 1-30 colony forming units (CFU) of bacteria per mL of blood[4].

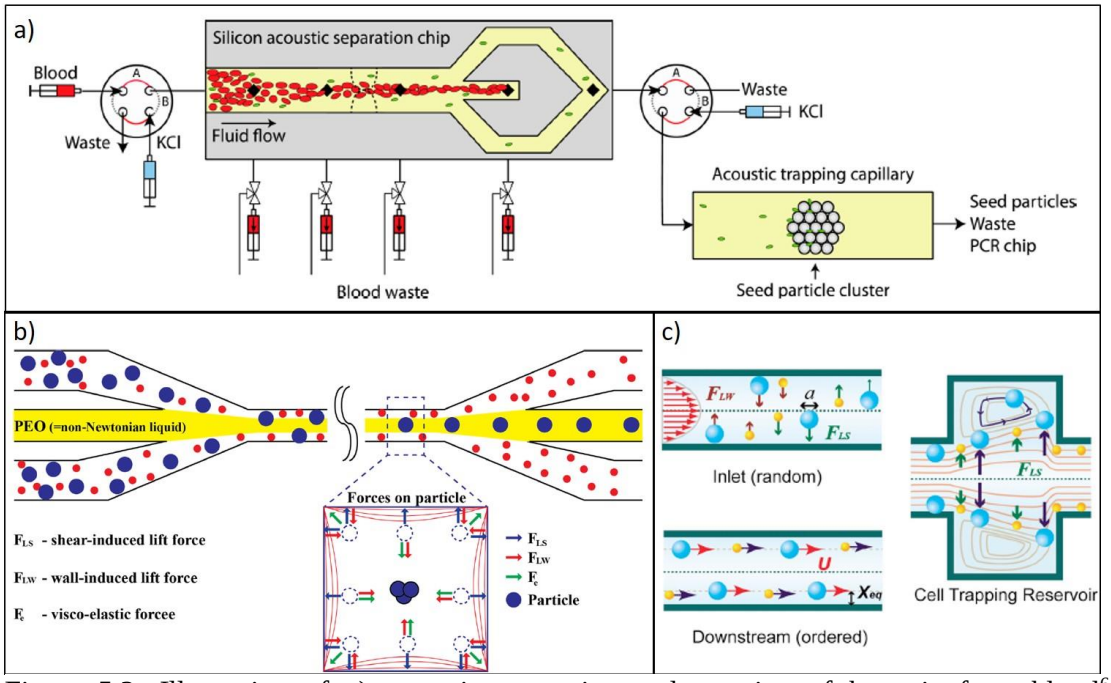

Figure 5.2: Illustration of a) acoustic separation and trapping of bacteria from blood[6] (Reproduced with permission), b) particle separation using elasto-inertial particle focusing[7] (Reproduced under Creative Commons), and c) hydrodynamic focusing and subsequent trapping of large particles in laminar vortices[8] (Reproduced with permission)

Several different approaches to isolate and concentrate pathogens in blood using size based separations have been discussed in the literature. Work by Ohlsson et al. used acoustophoretic plasma generation from blood to isolate bacteria and then used seed particle trapping enrichment and PCR to concentrate and detect them (Figure 5.2a). The authors reported a processing time of 2 hours, a bacteria capture efficiency of 91%, and a limit of detection of 1000 bacteria/mL[6]. Although this study demonstrated excellent capture efficiency and fast processing times, it also required a high concentration of bacteria for detection and faced challenges with scalability. A study by Faridi et al. used elasto-inertial microfluidics for size based separation of bacteria from whole blood (Figure 5.2b). They reported a bacteria capture efficiency of 76% & 73% while operating at flow rates of 30 & 60 µL/min respectively[7]. While this method does successfully isolate bacteria from whole blood, the low flow rates and lack of modularity of their microfluidic system will require more than 30 minutes processing time. Hur et al. demonstrated the selective isolation of large particles and cells using laminar vortices with flow rates at the mL/min scale (Figure 5.2c).

They reported a capture efficiency of 10% and 23% for cells with average diameters of 12.4 μm and 20 μm respectively[8]. While isolating pathogens in side cavities using microvortices is an excellent way to concentrate them, the method outlined by Hur et al. relies upon hydrodynamic forces that scale with the particle diameter to move the particles of interest into the side cavities making it impractical for capturing bacteria (Figure 5.2c). As a result, a more suitable method is needed to concentrate and isolate small pathogens like bacteria.

Here we investigate the efficacy of using dendritic freeze-cast ceramics for diffusion based size-separation. The dendritic morphology consists of a main channel, or primary pore, that has side cavities occurring at regular intervals along the pore wall (Figure 5.3a). Similar to the work by Hur et al., as the fluid flow through the main channel passes over the side cavities it was expected to form microvortices in the side cavities as seen in Figure 5.3b. These microvortices then facilitate the hydrodynamic trapping of small pathogens that diffuse to the side cavities at a faster rate than the large red blood cells. Capturing pathogens via diffusion is an inherently slow process due to the distance traveled by a diffusing particle scaling as $t^{1/2}$ and therefore requires slow fluid velocities to achieve high capture efficiency. Although the slow fluid velocities are at odds with the goal of rapidly isolating pathogens, dendritic freeze-cast ceramics have an advantage in terms of high primary pore density (on the order of 1000s per square centimeter)[9]. The high pore density allows for a low fluid velocity (3.5 to 70 μm/s) in each pore while achieving a fast total flow rate (10 to 200 μL/min). Furthermore, increasing the total volumetric flow rate while maintaining the same fluid velocity in the primary pores only requires an increase in the area of the ceramic. In this

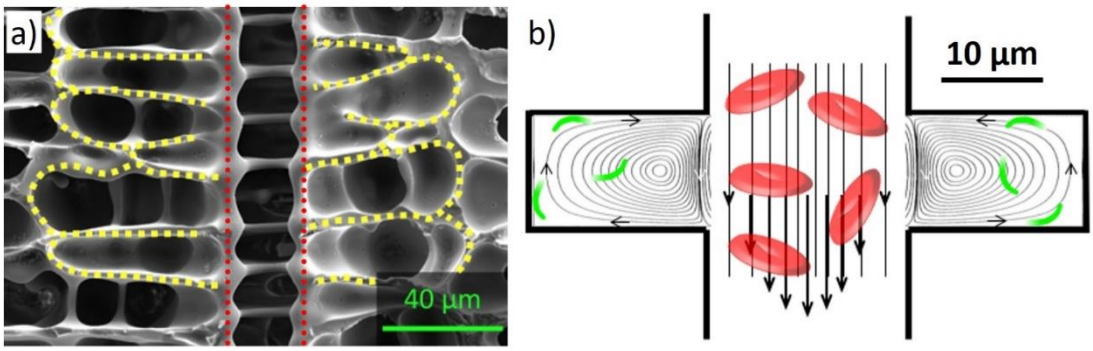

Figure 5.3: a) SEM micrograph of dendritic ceramic in the longitudinal direction, primary pore outlined in red and side cavities outlined in yellow. b) Illustration of fluid flow through dendritic channels with large red blood cells flowing throw primary pores and small pathogens

chapter we use a model system comprising different sizes of polystyrene microparticles (PP) to characterize the performance of two dendritic structures. Then, the capability of dendritic ceramics with different surface functionalities was tested using *E. coli* as model bacteria.

5.2 Experimental Methods

5.2.1 Materials

Cyclohexane, Glycerol, Epichlorohydrin (ECH), 3-Aminopropyltrimethoxysilane (ATMS), Bovine Serum Albumin (BSA), Di(ethylene glycol) diacrylate (EGA), Isopropanol (IPA), Dimethyl sulfoxide (DMSO), and TRIS hydrochloride (TRIS) were purchased from Millipore Sigma. Poly(diallyldimethylammoium chloride) solution [average MW 400 -500 kDa, 20 wt.% in H_2O] was obtained from Sigma-Aldrich. Hyperbranched polyethylenimine (PEI) was procured from Polysciences. Fluorescent polystyrene particles (PP) at a 1 w/v% concentration and with average diameters of 2 μm (λ_{ex} – 510 nm, λ_{em} – 560 nm) and 0.28 μm (λ_{ex} – 590 nm, λ_{em} – 620 nm) were purchased from Spherotech. Polysiloxane (CH3-SiO1.5, Silres® MK Powder) and Geniosil® GF 91 were purchased from Wacker Chemie. NEB turbo strain *E. coli* bacteria expressing the mWasabi fluorescent protein (λ_{ex} – 493 nm, λ_{em} – 509 nm) was provided by L. Xiong. All chemicals and materials were used as received. Buffers were prepared using indicated chemicals and distilled water.

5.2.2 Fabrication & characterization of dendritic freeze cast ceramics

The freeze-casting process of the dendritic ceramic membranes described here were adapted from chapter 7.1 of Dr. Noriaki Arai's thesis[9]. Two different freeze-cast ceramics were fabricated for this study by Dr. Arai and Laura Quinn. For each structure, the preceramic polymer was dissolved in cyclohexane at a concentration of 20 wt.%. Next, the cross-linking agent (Geniosil® GF 91) was added at a concentration of 1 wt.% with respect to the solution. The resulting solution was stirred for 5 minutes prior to the freeze casting process. The first structure (type 1) was freeze-cast using a conventional freeze-casting setup, in which temperature is only controlled on the bottom side of the mold. The solution for the

first structure was frozen at a freezing front velocity of 15 µm/s. The second structure (type 2) was freeze-cast while controlling the temperature gradient across the mold. The freezing front velocity was 15 µm/s and the temperature gradient was maintained at 2.6 K/mm. The sample was then coarsened at 4 ºC for three hours and then it was refrozen (refer to chapter 5 of Dr. Arai's thesis for additional details on freeze-casting procedure)[9]. Once a sample was completely frozen, the sample was sublimated in a freeze drier (VirTis AdVantage 2.0) to remove the solvent crystals. Once the solvent was gone, the polymer scaffold was pyrolyzed in argon at 1100 °C for four hours. The pyrolyzed samples were then cut using a diamond saw into sections with a thickness of 3.2 mm. Pore size of the dendritic ceramics were characterized by mercury intrusion porosimetry (Auto Pore IV, Micromeritics). Following a flow-through experiment, the dendritic ceramic was imaged by SEM (FE SEM – Zeiss 1550 VP) using the procedure outlined in chapter 4, section 4.2.6.1.

5.2.3 Ceramic functionalization

To fabricate ceramics with amine and ethylene glycol functionality, several type 1 membranes were functionalized with a PEI gel layer using the process outlined in chapter 4, section 4.2.4. In summary, the samples were first immersed and incubated in 1 M NaOH for 90 minutes. They were then washed in water before being incubated in a 0.1 M HCl solution for 30 minutes. The samples were then washed in water again, before being dried at 110 ºC for 1 hour. Once dried, they were added to a 2 v% solution of ATMS in isopropanol and incubated for 3 hours at 60 ºC. The samples were then washed thoroughly in water and isopropanol before being cured at 110 ºC for 30 minutes. Following the curing of the aminosilane layer, the PEI gel solution was prepared by dissolving PEI in IPA at a molar ratio of 1:37.4, respectively. Ten minutes before adding the solution to the ceramic, ECH was added to the solution at a molar ratio of 1 mole PEI for 16.5 moles ECH – corresponding to 1.1 ECH molecules for every available amine. The ceramic was completely immersed and then incubated in the IPA/PEI/EHC solution overnight at room temperature. After the overnight incubation, a large excess of DMSO (relative to IPA) was added to the vial and the

resulting solution was heated to 80 ºC for 1 hour to remove leftover reactants and unbound products. The sample was then washed with IPA and dried at room temperature for one hour.

All samples were then incubated at 80 ºC for 1 hour in a 30 mM PEI solution. After one hour, the samples were washed thoroughly with distilled water and dried at 110 ºC for 1 hour. The amine terminated samples were then stored for future use. The ethylene glycol terminated samples were then incubated at room temperature in a 50 mM EGA solution for 1 hour. The samples were then thoroughly washed with distilled water, dried at 110 ºC for 1 hour, and stored for use in the flow-through experiments.

5.2.4 Flow-through experiments

All samples were prepared for the flow-through experiments by being placed in a jar filled with the working fluid. The jar was sealed with a septa cap and then a needle attached to in-house vacuum (25 mmHg) was inserted through the septa and left to incubate overnight. The vacuum-infiltration avoids the formation of air pockets inside the side cavities and infiltrating with the working fluid removes contributions to particle motion from solvent/solute concentration gradients.

A syringe was first filled with the working fluid and then connected to the tubing leading to the sample holder. The syringe pump was set to an infusion rate of 1000 µL/min up until the bottom portion of the sample holder was full. The ceramic sample was then added to the holder and, after ensuring the absence of air bubbles, the holder was sealed. For control experiments the ceramic sample was replaced by a plastic disc with 4 holes that had a total

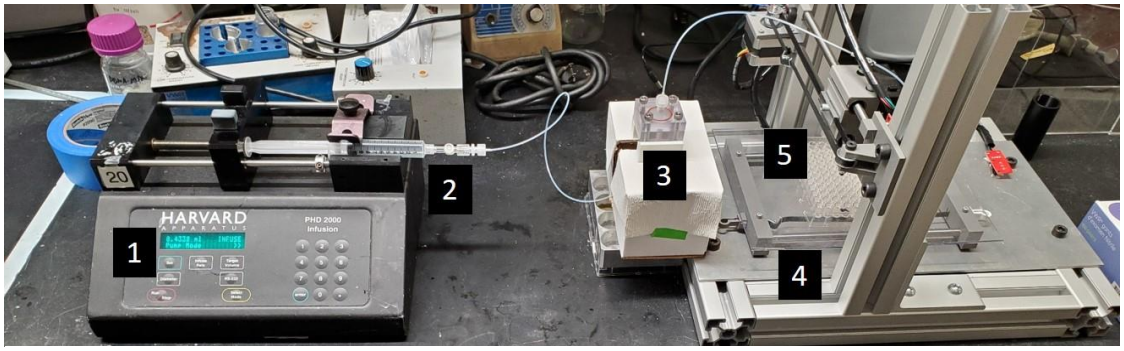

Figure 5.4: A picture of the flow-through experimental setup with: 1. Syringe pump, 2. In-line injection connector, 3. Sample holder, 4. Automated sampler, 5. 96-well collection plate

volume equal to the primary pore volume of a type 1 membrane, unless otherwise noted. Once the working fluid reached the end of the outlet tube, the flow rate was adjusted to the experimental conditions specified below. Upon reaching the experiment-specific flow rate, a 'pulse' of 300 µL (~total volume of primary pores and side cavities) of particle/bacteria suspension was added via the in-line injection connector. Next, twenty-four aliquots of 200 µL were collected in a 96-well plate.

The fluorescence signal of the particles/bacteria in each well was measured using a plate reader (FlexStation3 Microplate Reader, Molecular Devices, LLC). To account for background signal from the working fluid, the average fluorescent signal of two wells filled with 200 µL of the working fluid were subtracted off from all sample signals. A series of wells were also used to prepare a concentration to fluorescence calibration curve.

5.2.4.1 Separation of polystyrene microparticles

Initial flow-through experiments investigated the particle separation capabilities of the different dendritic structures. The working fluid in these experiments was a 15 vol.% glycerol in water mixture prepared as a density matching solvent for the polystyrene microparticles. For the particle suspension, a solvent mixture was prepared by dissolving 300 µL of glycerol in 1660 µL of water. Once the glycerol was fully dissolved, 20 µL of poly(diallyldimethylammonium chloride) solution was added to the glycerol/water solution. The resulting mixture was vortexed for 20 seconds to ensure a homogeneous distribution. The fluorescent PP suspensions were sonicated for 1 minute before adding 20 µL of the 2 µm fluorescent particle suspension. The resulting suspension was mixed via pipetting before adding 20 µL of the 0.28 µm fluorescent particle suspension. The final suspension was vortexed for another 20 seconds prior to use. Each ceramic membrane tested under these conditions was first operated at a flow rate of 10 µL/min for 4.8 mL, then washed with several milliliters of the working fluid, and finally operated again at a flow rate of 40 µL/min.

5.2.4.2 Flow-through experiments with *E. coli*

To model the effects of ceramic surface functionality and blood proteins on capture of bacteria, two solutions with different BSA concentrations were prepared to serve as the working fluid. The first solution consisted of 2 mg/mL BSA in a 50 mM TRIS buffer, which acted as a control. The second solution consisted of 35 mg/mL BSA in 50 mM TRIS buffer, corresponding to the lower end of the human plasma albumin concentration range. Human plasma albumin accounts for approximately 60% of the total human plasma proteins[10].

The bacteria suspension was prepared using a bacteria culture that was grown using the protocol outlined in Appendix C. The culture was centrifuged at 2700 rpm for 5 minutes to pellet the bacteria. The growth media was then removed from the culture tube, and the bacteria were resuspended in the same volume of working fluid using gentle pipetting. Once the bacteria suspension was prepared, the experiment was carried out using an operating fluid flow rate of 50 µL/min.

5.2.4.3 Influence of functionalized ceramics on polystyrene 'capture'

A set of experiments determining the influence of the functionalized ceramics on the 'capture' polystyrene microparticles under the operating conditions from section 5.2.4.2 was pursued using the 35 mg/mL BSA in 50 mM TRIS buffer as the working fluid. The particle

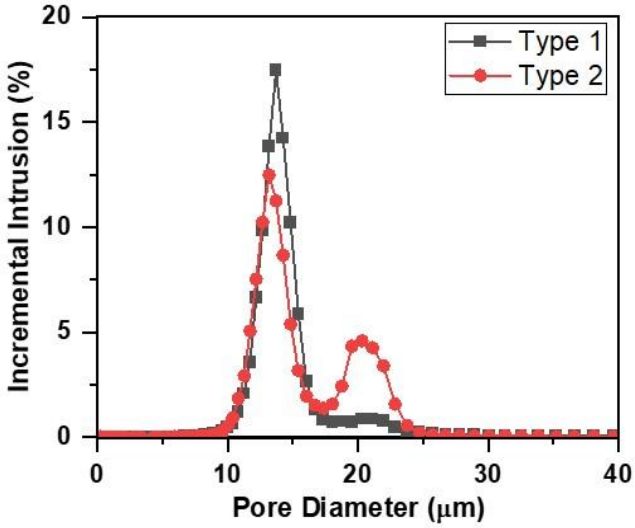

Figure 5.5: Pore size distribution of dendritic ceramics

suspension was prepared by adding 20 µL of the sonicated 2 µm fluorescent particle suspension to a vial containing 1.96 mL of 35 mg/mL BSA in 50 mM TRIS buffer. The resulting suspension was vortexed for 20 seconds. Next, 20 µL of the sonicated 0.28 µm fluorescent particle suspension was added to the vial, and the resulting suspension was vortexed again for 20 seconds. There was no observed settling of the polystyrene microparticles over the course of the experiment (10 hours). Upon completion of the suspensions, the experiment proceeded with an operating fluid flow rate of 50 µL/min.

5.3 Results and discussion

5.3.1 Separation efficiency of different ceramic structures

Figure 5.5 shows the pore size distribution of type 1 and type 2 dendritic ceramics obtained using mercury porosimetry. The type 1 structure reports peaks at ~22 µm and ~14 µm corresponding to the primary pores and side cavities respectively. The area of the peak around 22 µm indicates what percentage of the total porosity stems from the volume of the primary pores. For type 1 the areas are 8% and 92% for the primary pore and side cavity respectively. The primary pore peak for the type 2 structure is also around 22 µm, while the peak corresponding to the side cavities is centered closer to 13 µm. The peak areas are for the main channel and side cavities are 25% and 75% respectively. A summary of the ceramic dimensions and pertinent fluid flow characterization is presented in Table 5.1. Please consult appendix B for additional details on the calculations.

Table 5.2 summarizes the total percentage of pulsed particles obtained in the filtrate for type 1 and type 2 membranes as well as flow through an empty sample holder. The percentage of particles passed through will be used for all data analysis to account for any nonspecific interactions between the added particle/bacteria and the flow-through setup, excluding the ceramic membrane. The empty sample holder reported over 90% of the added particles in the filtrate for both particle sizes and flow rates. Type 1 membranes reported significantly lower passage of particles at the slower flowrate of 10 µL/min for both particle sizes. Interestingly the difference between the particle percentage of 2 µm and 0.28 µm for a

given flow rate was higher at the faster flow rate of 40 µL/min. The type 2 membranes showed a higher passage of particles in comparison to a type 1 membrane operating at the same conditions. The difference in the percentage of 2 µm particles and 0.28 µm particles passing through the ceramic was approximately the same for the two flow rates investigated.

Table 5.1: Summary of ceramic dimensions and fluid characterization for particles in glycerol flow-through

Membrane structure	Type 1		Type 2	
Thickness (mm)	3.2		3.2	
Ceramic diameter (mm)	20		20	
Primary pore 'diameter' (µm)	22		22	
Primary pore Volume%	8		25	
Percent porosity	76		76	
Side cavity 'diameter' (µm)	13		14	
Solution viscosity (mPa*s)	1.65		1.65	
Solution density (g/mL)	1.04		1.04	
Flow rate (µL/min)	10	40	10	40
Average velocity (µm/s)	8.7	35	2.8	11
Residence time (s)	367	92	1150	287
Re	1.2E-4	4.8E-4	3.9E-5	1.6E-4
Pe – 2 µm	1.9E3	7.7E3	6.1E2	2.5E3
Pe – 0.28 µm	1.9E2	7.7E2	61.4	2.5E2

The lower particle flow-through in both membranes at 10 µL/min was expected due to the slower fluid velocity increasing the residence time allowing more particles to diffuse into the side cavities. Similarly, the higher retention of 0.28 µm particles, in comparison to 2 µm particles, was expected due to the faster diffusion of the smaller molecules into the side

Table 5.2: Percentage of 'pulsed' particles in filtrate

Particle size	2 µm		0.28 µm	
Flow rate (µL/min)	10	40	10	40
Empty device	98%	96%	96%	93%
Type 1	29%	58%	24%	41%
Type 2	63%	76%	52%	67%

cavities. In contrast, the higher retention of particles by the type 1 membrane was initially quite surprising due to type 1 membranes having the larger Peclet number. A larger Pe indicates that the particles should have less time to diffuse to the side cavities and therefore there should be a higher percentage of particles collected in the filtrate. The source of the discrepancy between expected and observed behavior became apparent upon inspecting the inlet surface of a type 1 and type 2 ceramic using SEM. Figure 5.6 shows the SEM micrographs of type 1 and type 2 ceramics, in panels a and b respectively, following the particle flow-through experiments. A comparison of the two images reveals that the type 1 membrane has over 200 particles settled on its surface, while the type 2 membrane has less than 50. This indicates that the unexpectedly low passage of particles using the type 1 membrane stems in part from particles settling on the inlet surface rather than being captured in the side cavities. The extent of particles settling on the surface was unexpected due to the efforts to density match the solution and the polystyrene particles. However, the fluid velocities near the inlet surface of the membrane are very slow, which allows time for the polystyrene particles to interact with the ceramic. Both the polystyrene particles and the neat SiOC are hydrophobic, which provides a driving force for them to interact and pull the particles out of suspension. Two methods, examined in the following section, to prevent such

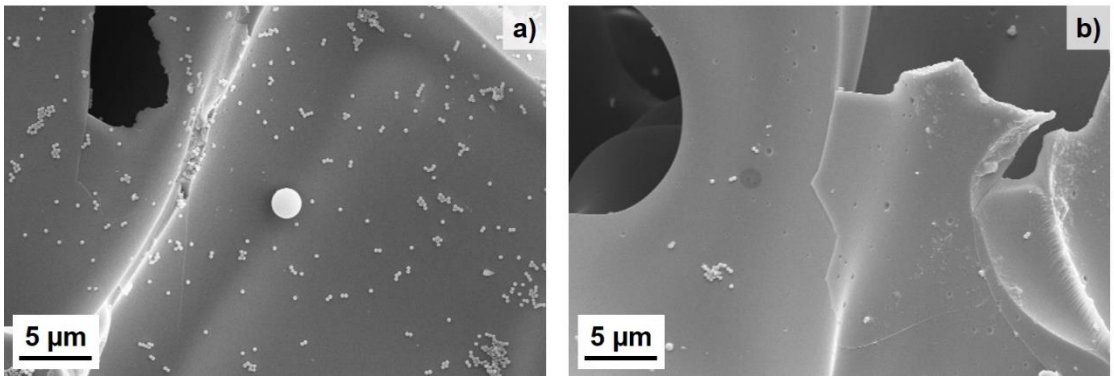

Figure 5.6: SEM micrographs of the inlet surface following a flow-through experiment using polystyrene particles in a) type 1 ceramic and b) type 2 ceramic

interactions are: 1. functionalize the ceramic surface with hydrophilic functional groups. 2. stabilize the particle suspension with proteins.

5.3.2 Influence of functionalized ceramics on *E. coli* capture

At the low BSA concentration (2 mg/mL) only 20% of the bacteria are recovered in the control experiment (a dish with large holes and low surface area (Fig 5.7a) This suggests that 80% of the bacteria adsorb on internal surfaces of the apparatus – unrelated to the porous ceramic. When a ceramic with hydrophobic surface (neat SiOC) is used, the passage of bacteria is reduced by half. Adsorption of the bacteria to the membrane persists when amine functional groups are added and no longer occurs when the pore walls are functionalized with PEG. One method to reduce the adsorption of E. coli to the apparatus is to increase the concentration of BSA. The additional BSA will act as a passivating layer that inhibits the interaction between the bacteria and the apparatus. As a result, when a higher concentration of BSA (35 mg/mL) is used, the fraction of bacteria passing through the apparatus increases to 0.42 (Fig. 5.7b). The PEG terminated ceramic once again demonstrated a performance similar to the control with 36% of the E. coli passing through. Of note is the observation that the fraction of E. coli that passes through the apparatus for the neat and amine terminated ceramics diverge to 0.27 and 0.18 respectively.

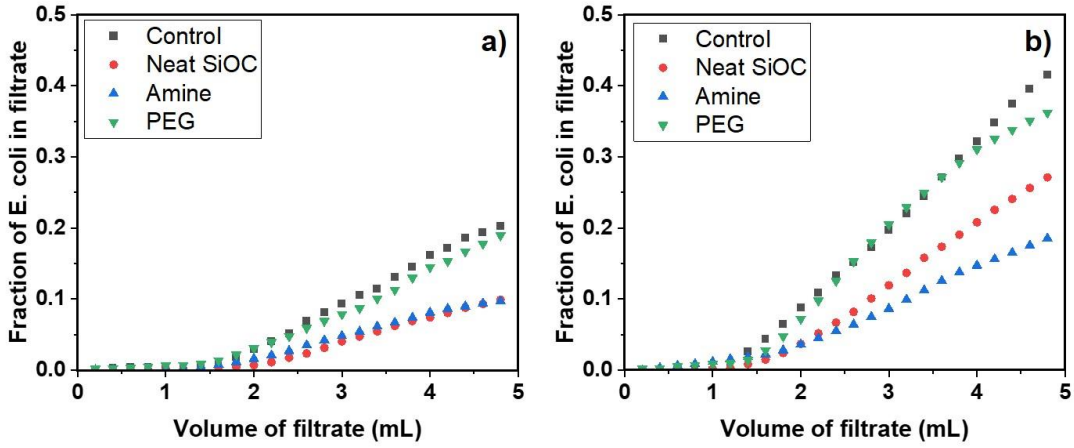

Figure 5.7: Cumulative fraction of 'pulsed' E. coli in the filtrate over 16 membrane volumes when the working fluid is a) 2 mg/mL BSA in 50 mM TRIS buffer and b) 35 mg/mL BSA in 50 mM TRIS buffer.

The difference in bacteria retention between the neat and PEG terminated ceramics was attributed to the hydrophilicity of the ethylene glycol groups. It has been well documented in the field of water purification that having a sufficiently hydrophilic membrane surfaces is critical to avoid bacteria settling on membrane surface and fouling the membrane[11,12]. Similarly, terminating the membrane surface in ethylene glycol groups improves the hydrophilicity which reduces nonspecific binding of bacteria to the membrane surface. The reduced nonspecific binding leads to a larger fraction of added bacteria being collected in the filtrate for the PEG terminated samples. The difference between the two is present in both the low BSA solution and the high BSA solution, which indicates that even at 35 mg/mL BSA there is some nonspecific binding of bacteria to the neat membrane surface.

Both the neat and amine terminated ceramic membranes bind *E. coli*, the former through nonspecific surface interactions and the latter through electrostatic interactions. At low BSA concentrations there is limited interference with the nonspecific binding on the ceramic surface and as a result the retention behavior in the two ceramics is very similar. However, at a BSA concentration of 35 mg/mL, nonspecific binding on the neat ceramic surface is reduced via surface passivation resulting in a higher fraction of the 'pulsed' *E. coli* being collected in the filtrate (from 0.1 to 0.27). In contrast, the amine terminated ceramic shows a smaller increase in the fraction of bacteria in the filtrate (from 0.1 to 0.18). The smaller increase stems from the better binding capabilities of the amine terminated functional layer enabling continued surface-bacteria interactions.

The close behavior of the control (disk with large openings) and PEG terminated porous ceramic at low BSA concentrations was quite surprising. We suspect that the missing *E. coli* are not captured by the PEG terminated ceramic, but are instead nonspecifically bound throughout the flow-through setup. This is supported by the high retention of bacteria by the control, which indicates the *E. coli* nonspecifically bind to the plastic tubing, chamber walls, and perhaps the control disc. Investigating the difference between the PEG terminated sample and the control when using the 35 mg/mL BSA solution provides additional support

for this hypothesis. Namely, if the 'captured' *E. coli* were nonspecifically bound throughout the flow-through device, it would be expected that the cumulative fraction of bacteria in the filtrate for the PEG terminated ceramic and the control would increase by the same amount, which accords with observation (Fig. 5.7b) This disparity was observed in triplicate experiments.

5.3.3 Influence of functionalized ceramic on polystyrene capture

Testing the microparticle suspensions at the higher BSA concentration (35 mg/mL) demonstrated that, in agreement with the observations made when testing bacteria, using the control disc led to the highest fraction of particles collected in the filtrate (Fig 5.8). Interestingly, the fractions of 0.28 µm and 2 µm particles collected were the same at 0.9. The next highest fraction, also in accord with observation from the previous section, was the filtrate from the PEG terminated ceramic. In contrast to the measurements with E. coli, a larger portion of the particles passed through the amine terminated ceramic than the neat

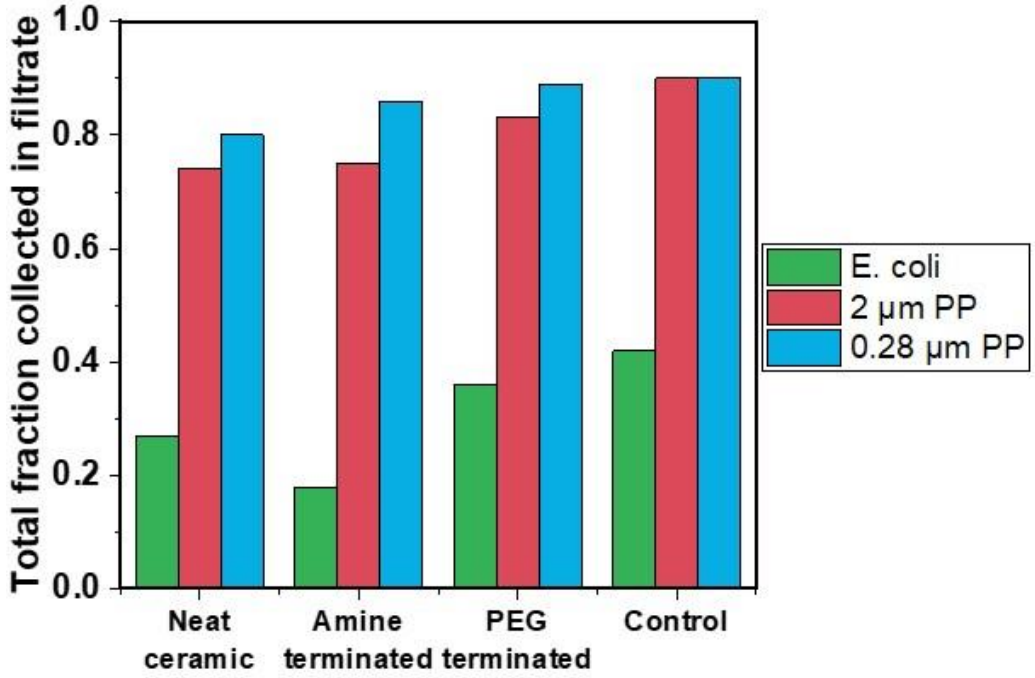

Figure 5.8: Total fraction of added species in filtrate when working fluid is 35 mg/mL BSA in 50 mM TRIS buffer

SiOC. In all tests using a ceramic sample, the fraction of 2 μm particles in the filtrate was lower than 0.28 μm particles. The fraction of particles in the filtrate was higher than the fraction of bacteria for each ceramic as well as the control. The largest difference between the bacteria and the particles was seen in the amine terminated (0.18 versus 0.75/0.86 respectively), while the smallest difference in the fraction collected in the filtrate was exhibited by the control (0.42 – bacteria; 0.9 – 2 & 0.28 μm particles).

The small differences in particle retention between the different ceramics are explained through surface interactions. The neat and amine terminated ceramic have favorable surface interactions with the particles, leading to a lower fraction in the filtrate. The PEG terminated ceramic suppresses surface interaction leading to a higher fraction of particles passing through the pores than the neat or amine terminated. It was expected that the fraction of added 0.28 μm particles in the filtrate would be lower than the 2 μm particles due to differences in diffusion as discussed above. However, the data presented in Figure 5.8 reveals the opposite trend, with the 0.28 μm having a higher concentration in the filtrate. This trend reversal is attributed to the smaller particles being more thoroughly stabilized by the BSA solution, thereby limiting interactions with the sample surface.

Table 5.3: Summary of fluid parameters when using a type 1 ceramic at a flow rate of 50 μL/min.

Fluid velocity (μm/s)	Residence time (s)	Re	Pe – 2 μm particles	Pe – 0.28 μm particles	Pe – E. coli
14	229	9.6E-4	9.6E3	9.6E2	9.6

The large differences in particle and bacteria retention under the same operating conditions have a few key contributions. First, *E. coli* may have a much higher diffusivity than the polystyrene microparticles (100 $\mu m^2/s$ – *E. coli*[13], 1 $\mu m^2/s$ – 0.28 μm[14], 0.1 – 2 μm[14]) depending on the bacterial strain. A higher diffusivity, and lower Pe in Table 5.3, increases the number of bacteria that will diffuse into the side cavities as well as the frequency with which the bacteria comes in contact with the pore wall. Second, the surface functionality of the different ceramics changes how they interact with both the bacteria and the particles. For example, the amine terminated ceramic was designed to bind *E. coli* in a range of BSA

concentrations, but does not have much influence on the polystyrene particles. In contrast, the PEG terminated ceramic was functionalized to push everything away and demonstrates a lower retention of both the bacteria and particles than the neat or amine terminated ceramics. Third, nonspecific binding to the flow-through setup. While it has been demonstrated that the particles have minimal interaction with the flow-through setup (both with and without BSA), further investigation is still needed to determine the contribution of nonspecific binding when working with *E. coli*.

5.4 Conclusions

This study investigated using dendritic ceramic membranes for diffusion-based size separation of polystyrene particles and capture of *E. coli*. It was demonstrated that the ceramic membranes had qualitative size selectivity of the particles, but also exhibited notable interactions with the ceramic surface. The influence of functionalizing the ceramic surface was tested using *E coli*. suspensions in different concentrations of BSA. It was shown that using a PEG terminated layer reduced nonspecific binding to the ceramic surface, while an amine terminated functionalization improved the retention of bacteria. Lastly, a comparison between flow-through experiments of particles and *E. coli* at the same operating conditions demonstrated significant differences in retention consistent with the disparity in diffusivities of the species. Recommendations for future avenues of inquiry are provided in chapter 6.

References

(1) Sepsis https://www.biomerieux.com/en/sepsis (accessed 2021 -08 -26).

(2) Morgenthaler, N. G.; Kostrzewa, M. Rapid Identification of Pathogens in Positive Blood Culture of Patients with Sepsis: Review and Meta-Analysis of the Performance of the Sepsityper Kit. International Journal of Microbiology 2015, 2015, e827416. https://doi.org/10.1155/2015/827416.

(3) Schoepp, N. G.; Khorosheva, E. M.; Schlappi, T. S.; Curtis, M. S.; Humphries, R. M.; Hindler, J. A.; Ismagilov, R. F. Digital Quantification of DNA Replication and Chromosome Segregation Enables Determination of Antimicrobial Susceptibility after Only 15 Minutes of Antibiotic Exposure. Angewandte Chemie International Edition 2016, 55 (33), 9557–9561. https://doi.org/10.1002/anie.201602763.

(4) Afshari, A.; Schrenzel, J.; Ieven, M.; Harbarth, S. Bench-to-Bedside Review: Rapid Molecular Diagnostics for Bloodstream Infection - a New Frontier? Critical Care 2012, 16 (3), 222. https://doi.org/10.1186/cc11202.

(5) Schlappi, T. S.; McCalla, S. E.; Schoepp, N. G.; Ismagilov, R. F. Flow-through Capture and in Situ Amplification Can Enable Rapid Detection of a Few Single Molecules of Nucleic Acids from Several Milliliters of Solution. Anal. Chem. 2016, 88 (15), 7647–7653. https://doi.org/10.1021/acs.analchem.6b01485.

(6) Ohlsson, P.; Evander, M.; Petersson, K.; Mellhammar, L.; Lehmusvuori, A.; Karhunen, U.; Soikkeli, M.; Seppä, T.; Tuunainen, E.; Spangar, A.; von Lode, P.; Rantakokko-Jalava, K.; Otto, G.; Scheding, S.; Soukka, T.; Wittfooth, S.; Laurell, T. Integrated Acoustic Separation, Enrichment, and Microchip Polymerase Chain Reaction Detection of Bacteria from Blood for Rapid Sepsis Diagnostics. Anal. Chem. 2016, 88 (19), 9403–9411. https://pubs.acs.org/doi/abs/10.1021/acs.analchem.6b00323. (Further permissions related to figures reproduced from this article should be directed to ACS journal).

(7) Faridi, M. A.; Ramachandraiah, H.; Banerjee, I.; Ardabili, S.; Zelenin, S.; Russom, A. Elasto-Inertial Microfluidics for Bacteria Separation from Whole Blood for Sepsis Diagnostics. J Nanobiotechnol 2017, 15 (1), 3. https://doi.org/10.1186/s12951-016-0235-4.

(8) Hur, S. C.; Mach, A. J.; Di Carlo, D. High-Throughput Size-Based Rare Cell Enrichment Using Microscale Vortices. Biomicrofluidics 2011, 5 (2), 022206. https://doi.org/10.1063/1.3576780.

(9) Arai, N. Freeze Casting of Ceramics: Pore Design from Solidification Principles. PhD Thesis, California Institute of Technology, 2021.

(10) 5 Human Albumin. Transfus Med Hemother 2009, 36 (6), 399–407.

(11) Mansouri, J.; Harrisson, S.; Chen, V. Strategies for Controlling Biofouling in Membrane Filtration Systems: Challenges and Opportunities. Journal of Materials Chemistry 2010, 20 (22), 4567–4586. https://doi.org/10.1039/B926440J.

(12) Mi, Y.-F.; Xu, G.; Guo, Y.-S.; Wu, B.; An, Q.-F. Development of Antifouling Nanofiltration Membrane with Zwitterionic Functionalized Monomer for Efficient Dye/Salt Selective Separation. Journal of Membrane Science 2020, 601, 117795. https://doi.org/10.1016/j.memsci.2019.117795.

(13) Berg, H. C.; Turner, L. Chemotaxis of Bacteria in Glass Capillary Arrays. Escherichia Coli, Motility, Microchannel Plate, and Light Scattering. Biophysical Journal 1990, 58 (4), 919–930. https://doi.org/10.1016/S0006-3495(90)82436-X.

(14) Squires, T. M.; Quake, S. R. Microfluidics: Fluid Physics at the Nanoliter Scale. Rev. Mod. Phys. 2005, 77 (3), 977–1026. https://doi.org/10.1103/RevModPhys.77.977.

Chapter 6

CONCLUSIONS AND FUTURE WORK

In this chapter we provide suggestions for future work arising from the conclusions drawn in the preceding chapters. The suggestions will be broken up into three sections with the following topics: polymeric membranes, composite membranes, and dendritic ceramic membranes. These topics correspond to the work presented in Chapters 2-3, Chapter 4, and Chapter 5 respectively.

6.1 Mixed-matrix polymeric membranes

The influence of casting conditions on membrane morphology and polymer crystallinity has been well documented in the literature[1,2]. Other studies have investigated the impact of *in situ* generated functional particles on membrane structure[3,4]; however, we have found no mention of how the interplay between functional particles and casting conditions influences membrane morphology and polymer crystallinity. Here the influence of functional particles on membrane morphology under different casting conditions was elucidated using three nonsolvents chosen for their different interactions with PEI and PVDF. It was shown that using a nonsolvent that is indifferent to the PEI particles, IPA, resulted in a membrane with consistent PVDF structure and crystal phase at each PEI concentration. In contrast, using a nonsolvent that strongly swells the PEI microgels, H_2O, led to a shift from spherulitic to lacelike PVDF as well as a change from the α to the β crystal phase with increasing concentrations of PEI. With the mixed NMP:H_2O nonsolvent, a unique globular PVDF morphology was obtained that had a stronger shift to the β-phase with increasing PEI concentration than water cast membranes. While there may be some benefit to continue investigating different nonsolvents for novel membrane morphologies, the future work proposed here focuses on application of the membrane structures disclosed in Chapter 2.

In this work, membranes prepared using IPA as the nonsolvent were identified as being suitable for membrane chromatography due to their open and porous morphology. It

was demonstrated that controlling the crosslink density and crosslinker chemistry was critical to achieving both good protein binding and salt tolerance. Using BSA as a model protein, a maximum static binding capacity of 120 mg/mL in 50 mM TRIS buffer was achieved at a normalized crosslink density of 0.5 with BCAH as crosslinker. Now that the potential of mixed-matrix membranes as a chromatographic material has been exhibited, three avenues for additional research are presented. First, preliminary experiments using a MMM with BCAH as crosslinker, 54 wt.% PEI, and NCD of 0.4 revealed a static binding capacity of 200 mg/mL. This indicates that there is still an opportunity to further optimize the binding capacity of the reported membranes by changing the crosslink density. Second, although the experiments presented in Appendix A.1 provide insight into the PEI polymerization reaction kinetics, the mechanism behind particle formation and the influence of side reactions between PEI and PVDF are not well understood. Developing a better understanding of particle formation would facilitate improved control over particle size and PSD, thereby providing an opportunity to reduce interference between binding sites in the microgel (Fig. 3.3). Third, the primary and secondary amines in the PEI microgels provide opportunities for further functionalization. Reacting the available amines with chlorosulfonic acid would produce sulfonate groups thereby effectively turning the mixed-matrix membrane into a cation exchange membrane (CEX). The resulting CEX material would be useful in protein purification and would target a different subclass of contaminants than the base membrane.

Mixed-matrix membranes with a PVDF skin layer are frequently used for water purification in the literature[3,4]. Of particular interest is a study by Su *et al.* that used the piezoelectric response of PVDF to improve the anti-fouling behavior of a water purification

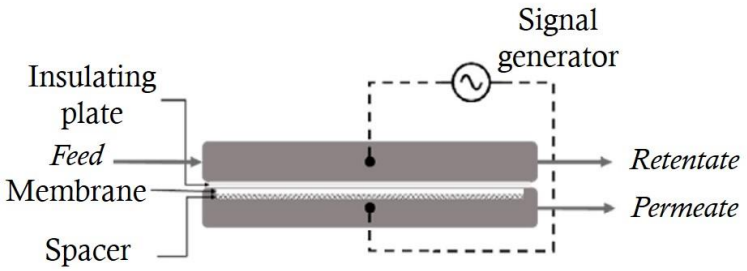

Figure 6.1: Illustration of a cross-flow filtration cell with electrical signaling for piezoresponsive water filtration[5] (Reproduced with permission)

membrane[5]. The study demonstrated higher water flux after poling the samples to align the electric dipoles in PVDF and, interestingly, observed that unpoled samples also exhibited a piezoresponse. PVDF's piezoelectric response stems from the electroactive β crystal phase. Chapter 2 of this thesis shows that β content has a positive correlation with PEI concentration for water cast membranes. Therefore, it is recommended that the flux and fouling behavior of 54 wt.% PEI membranes be studied under conditions similar to those depicted in Figure 6.1. Another course of study is to use the water cast membranes as ultrafiltration supports for a nanofiltration selective coating. The selective coating would be fabricated using interfacial polymerization and would be covalently anchored to the membrane surface via the PEI particles at the skin layer. Through incorporating zwitterionic moieties into the selective coating, the resulting NF membrane would have improved anti-fouling properties[6].

The PVDF crystals in membranes prepared in NMP:H_2O are comprised predominantly of the electroactive β-phase when PEI concentration is 6 wt.% or more. The β crystal phase of PVDF is a well-known ferroelectric and piezoelectric material that recent literature has shown is capable of improving catalytic performance[7]. The key contribution stems from the internal electric field of ferroelectric materials, such as PVDF in the β crystal phase, and the induced electric field in piezoelectric materials that facilitates the transport of charge carriers through the catalytic medium. However, over time internal electric fields tend to decline and any improvement on catalytic performance is lost. One method to maintain the internal electric field is to have an alternating electric field. Precedent for a system with such a field, Figure 6.2, was achieved by mechanically deforming PVDF fibers decorated in catalytic g-C_3N_4 microparticles[8]. Each time the PVDF fiber was mechanically deformed the surface of the fiber in contact with the g-C_3N_4 microparticles would switch charges from positive to negative or vice versa, thereby alternating the electric field. It is important to note that the internal electric field does not need to extend throughout the entirety of the PVDF membrane of fiber, but must be locally oriented to interact with the catalytic material. Although the electric dipoles of the β crystal phase in the NMP:H_2O cast membranes are not oriented throughout the bulk of the membrane, they are most likely oriented locally near the

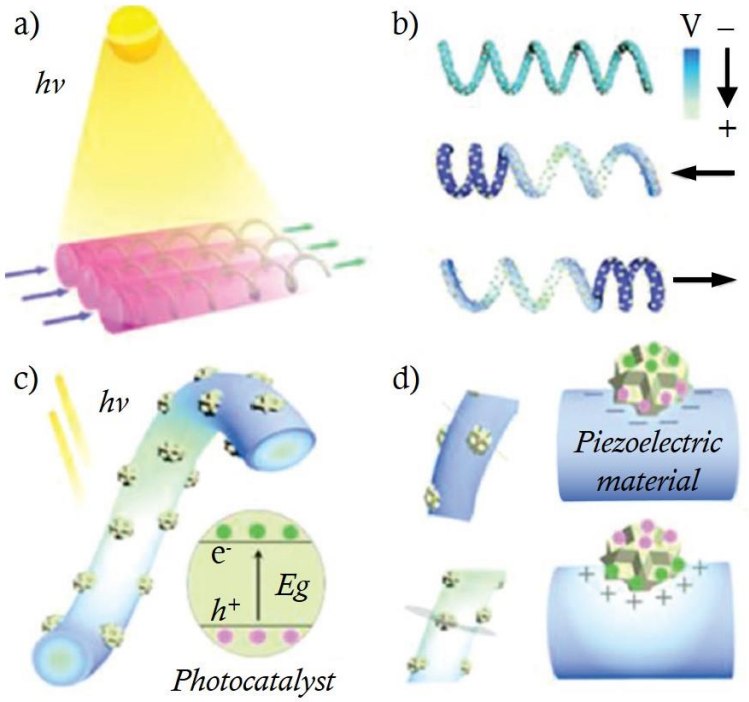

Figure 6.2: Schematic illustration of a) piezoelectric-photocatalytic composite helical microfibers, b) formation of internal electric field, c) gradational piezoelectric piezoelectric potential generated on deformed microfiber, and d) promoted separation of electrons and holes in the presence of piezoelectric potential. (Reproduced with permission)[8]

PEI particles as discussed in Chapter 2. In addition, work by Kotte *et al.* has already shown that mixed-matrix membranes with *in situ* generated polymeric microparticles may act as sorbents and hosts for metals with catalytic properties[9,10]. The inherent internal electric fields of these MMMs combined with their documented capability to host catalytic nanoparticles warrants an investigation of their performance as catalytic membranes.

6.2 Composite membranes

In this work, a novel method was developed to fabricate a composite membrane comprising a ceramic scaffold and polymer matrix. The scaffold and matrix were covalently bonded together to reduce any possibility of channeling due to detachment of the polymer from the ceramic. The resulting composite had a maximum reported static binding capacity of 65 mg/mL in 50 mM TRIS buffer, using a polymer matrix composed of 38 wt.% PEI and

NCD 0.4 (Fig. 4.6b). The same composition was used for dynamic binding experiments, where an average binding capacity of 61 mg/mL in 50 mM TRIS buffer was reported (Fig. 4.8). A natural continuation of the BSA binding experiments is to probe the binding capabilities of the composite in the presence of salt. It is expected that the composite will exhibit similar salt tolerance behavior as that observed in the polymeric membrane (Fig. 3.4); however, further investigations are required to validate this hypothesis.

In addition to characterizing composite salt tolerance, different polymer matrix compositions as well as the relationship between permeability and composite composition should be studied. Part of the motivation to incorporate the polymer matrix into the ceramic scaffold was to enable the use of mechanically unstable compositions that have interesting binding properties. While the polymer matrix compositions used in chapter 4 are mechanically weak, they do not fully capitalize upon the benefits of the ceramic scaffold. To maximize the usefulness of the ceramic scaffold, lower ratios of PVDF to PEI should be investigated. If the polymer matrix begins to lose stability within the ceramic pores, higher molecular weight PVDF (such as HSV900) may be used to support the PEI microgels at the same mass ratio of PVDF to PEI. The permeability of the composite membrane will be influenced by the composition of the polymer matrix. Maintaining a permeability that allows flow at low pressures is a critical requirement for membrane chromatography and is ultimately one of the key benefits over complete pore-filling with a hydrogel (Fig. 4.1c). Therefore, it is necessary to understand the relationship between the polymer dope composition, more specifically the PEI concentration, and the permeability.

6.3 Dendritic ceramic membranes

Flow through experiments with polystyrene microparticles were used to characterize the capture efficiency of dendritic ceramics with different pore configurations. It was shown that ceramics with larger side cavities reported a higher capture efficiency than ceramics with a higher number of main channels. The capture of *E. coli* from BSA solutions using dendritic ceramics with different surface functionalities demonstrated that non-specific binding of the bacteria to the surface could not be ignored when determining the capture efficiency of the

ceramic. A comparison between flow through measurements of *E. coli* and polystyrene microparticles under the same operating conditions showed a higher retention of bacteria regardless of ceramic surface functionality. The higher retention was ascribed to the higher active diffusivity of *E. coli* enabling the movement of the bacteria to the side cavities.

It is recommended that future work with the dendritic ceramic membranes focus on the following three areas for additional inquiry. First, in order to calculate the various dimensionless numbers and fluid properties shown in Appendix B several simplifying assumptions were made about the geometry of the main channel. While the resulting values were useful and provided an initial analysis of the fluid behavior in the main channel, there is still discussion on the validity of assuming formation of microvortices in the side cavities. Modeling a dendritic pore using Computation Fluid Dynamics (CFD) would provide critical insight on the presence of recirculating flow in the side cavities. If microvortices do form, the fluid behavior provided by the CFD simulations will guide the choice of experimental conditions to optimize capture of bacteria. If no microvortices form, the simulations will still provide a better understanding of the velocity profile in the side cavities, thereby guiding choice of channel parameters to improve pathogen capture from complex fluids. In addition, modeling the sample holder to identify the formation of any microvortices that could artificially improve the capture efficiency would provide useful context for the data presented in Chapter 5. Second, using different bacterial strains in the flow through experiments to investigate the role of active diffusivity, strain motility, and surface interactions in bacteria capture. Third, the results presented in Chapter 5 demonstrated the role of surface functionalization on capture efficiency. Additional surface functionalities that improve either the binding of bacteria or rejection of non-pathogens are worthy of additional examination.

In conclusion, the present thesis contributes to membrane technology through the disclosure of a method to control the morphology of mixed-matrix polymeric membranes as well as demonstrating the application of novel synthetic membranes in protein chromatography and separation of pathogens from complex fluids.

References

(1) Bottino, A.; Camera-Roda, G.; Capannelli, G.; Munari, S. The Formation of Microporous Polyvinylidene Difluoride Membranes by Phase Separation. *Journal of membrane science* **1991**, *57* (1), 1–20.

(2) Zuo, D.; Zhu, B.; Cao, J.; Xu, Y. Influence of Alcohol-Based Nonsolvents on the Formation and Morphology of PVDF Membranes in Phase Inversion Process. *Chinese journal of polymer science* **2006**, *24* (03), 281–289.

(3) Rao Kotte, M.; Hwang, T.; Han, J.-I.; Diallo, M. S. A One-Pot Method for the Preparation of Mixed Matrix Polyvinylidene Fluoride Membranes with in Situ Synthesized and PEGylated Polyethyleneimine Particles. *Journal of Membrane Science* **2015**, *474*, 277–287. https://doi.org/10.1016/j.memsci.2014.09.044.

(4) Kotte, M. R.; Cho, M.; Diallo, M. S. A Facile Route to the Preparation of Mixed Matrix Polyvinylidene Fluoride Membranes with In-Situ Generated Polyethyleneimine Particles. *Journal of Membrane Science* **2014**, *450*, 93–102. https://doi.org/10.1016/j.memsci.2013.08.025.

(5) Su, Y. P.; Sim, L. N.; Li, X.; Coster, H. G. L.; Chong, T. H. Anti-Fouling Piezoelectric PVDF Membrane: Effect of Morphology on Dielectric and Piezoelectric Properties. *Journal of Membrane Science* **2021**, *620*, 118818. https://doi.org/10.1016/j.memsci.2020.118818.

(6) Mi, Y.-F.; Xu, G.; Guo, Y.-S.; Wu, B.; An, Q.-F. Development of Antifouling Nanofiltration Membrane with Zwitterionic Functionalized Monomer for Efficient Dye/Salt Selective Separation. *Journal of Membrane Science* **2020**, *601*, 117795. https://doi.org/10.1016/j.memsci.2019.117795.

(7) Liu, Z.; Yu, X.; Li, L. Piezopotential Augmented Photo- and Photoelectro-Catalysis with a Built-in Electric Field. *Chinese Journal of Catalysis* **2020**, *41* (4), 534–549. https://doi.org/10.1016/S1872-2067(19)63431-5.

(8) Dai, B.; Yu, Y.; Chen, Y.; Huang, H.; Lu, C.; Kou, J.; Zhao, Y.; Xu, Z. Construction of Self-Healing Internal Electric Field for Sustainably Enhanced Photocatalysis. *Advanced Functional Materials* **2019**, *29* (16), 1807934. https://doi.org/10.1002/adfm.201807934.

(9) Kotte, M. R.; Kuvarega, A. T.; Talapaneni, S. N.; Cho, M.; Coskun, A.; Diallo, M. S. A Facile and Scalable Route to the Preparation of Catalytic Membranes with in Situ Synthesized Supramolecular Dendrimer Particle Hosts for Pt(0) Nanoparticles Using a Low-Generation PAMAM Dendrimer (G1-NH_2) as Precursor. *ACS Appl. Mater. Interfaces* **2018**, *10* (39), 33238–33251. https://doi.org/10.1021/acsami.8b11351.

(10) Kotte, M. R.; Kuvarega, A. T.; Cho, M.; Mamba, B. B.; Diallo, Mamadou. S. Mixed Matrix PVDF Membranes With in Situ Synthesized PAMAM Dendrimer-Like Particles: A New Class of Sorbents for Cu(II) Recovery from Aqueous Solutions by Ultrafiltration. Environ. Sci. Technol. 2015, 49 (16), 9431–9442. https://doi.org/10.1021/acs.est.5b01594.

Appendix A

SUPPLEMENTARY DATA FOR CHAPTERS 2 & 3

A.1 Chemical compatibility and reaction kinetics

Miscibility and Solubility studies

To better understand the dynamics of particle formation, a series of experiments was performed to determine the miscibility of TEP and DMSO as well as the solubility of PEI, BCAH, and PVDF in mixtures of TEP and DMSO. The solubility of BCAH in water and PEI was also investigated. The stock solutions were prepared in 20 mL scintillation vials and then heated to 80 ºC prior to imaging or formulating any of the subsequent mixtures. All subsequent solutions were prepared in 20 mL scintillation vials and kept on a hotplate at 80 ºC in between imaging, unless otherwise noted. The stock solutions used for these experiments are displayed in Figure A.1 with the corresponding compositions available in Table A.1. Note that Solutions 1-3 are clear and transparent at 80 ºC (Fig A.1) while the DMSO/BCAH solutions (4-6) all have a distinct yellow color. This yellow color is due to the presence of BCAH in the solution.

Solution 1: TEP		Solution 2: TEP + PEI		Solution 3: TEP + PVDF	
Solution 4: DMSO + BCAH (NCD 1)		Solution 5: DMSO + BCAH (NCD 0.5)		Solution 6: DMSO + BCAH (NCD 0.25)	

Figure A.1: Stock solutions used in miscibility and chemical kinetics studies. Provided here as reference for color changes observed during the experiments.

Table A.1: Compositions of the stock solutions provided in mmols and mass (solids) or volume (liquids)

	TEP		PEI		PVDF		DMSO		BCAH	
	mL	mmol	g	mmol	g	mmol	mL	mmol	g	mmol
Solution 2	7	41	1	1.7	-	-	-	-	-	-
Solution 3	7	41	-	-	1.18	3e-3	-	-	-	-
Solution 4	-	-	-	-	-	-	1.6	20	1.24	6.9
Solution 5	-	-	-	-	-	-	1	13	0.62	3.5
Solution 6	-	-	-	-	-	-	0.5	6.4	0.31	1.7

The first experiment probed the solubility of BCAH in the solvents mentioned above at room temperature using a concentration of 4 g BCAH/ 4 mL solvent (Fig. A.2). This concentration is much higher than the 3.1 g BCAH/ 5 mL DMSO used in the membrane fabrication of chapter 3. Figure A.2 displays the solutions at 4 time points corresponding to directly after adding BCAH to the solvent, 4 hours after adding the solvent, and 48 hours after adding the solvent. DMSO displays the best dissolution of BCAH, becoming transparent after 48 hours. Water is the next best solvent for BCAH, demonstrating a little cloudiness after 48 hours. TEP does not appear to dissolve BCAH at all, instead forming an opaque slurry that does not have any noticeable changes after 48 hours. Using PEI as the "solvent" appears to wet the BCAH after 48 hours, but does not dissolve it appreciably. The results from Figure A.2 provide the motivation behind dissolving the BCAH into DMSO to form the crosslinking solution for the membrane synthesis in chapter 3.

	Mixing time		
	0 min	4 hrs	48 hrs
BCAH + H_2O	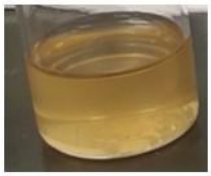		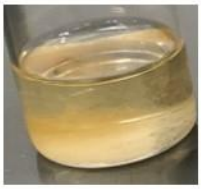
BCAH + DMSO		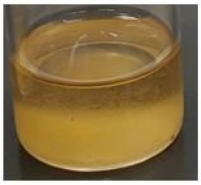	
BCAH + TEP			
BCAH + PEI		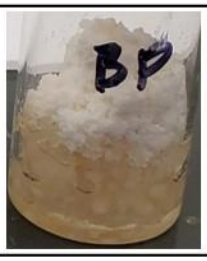	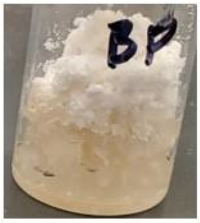

Figure A.2: Solubility of 4 grams of BCAH in 4 mL of indicated solvents over time

Next, the miscibility of TEP and DMSO and solubility of BCAH and PEI in mixed TEP/DMSO solutions were examined. The time resolved pictures are presented in Figure A.3. Upon mixing DMSO and TEP, a homogeneous solution that is transparent to optical inspection was produced indicating they are completely miscible. Next, adding a fully dissolved DMSO/BCAH solution to TEP results in a homogeneous, transparent, and slightly colored solution. This result was somewhat surprising after seeing the behavior of TEP and BCAH in the absence of DMSO. However, no precipitates were formed and the solution was stable at 80 ºC for 4 hours. In the third row of Figure A.3, DMSO was added to a prepared

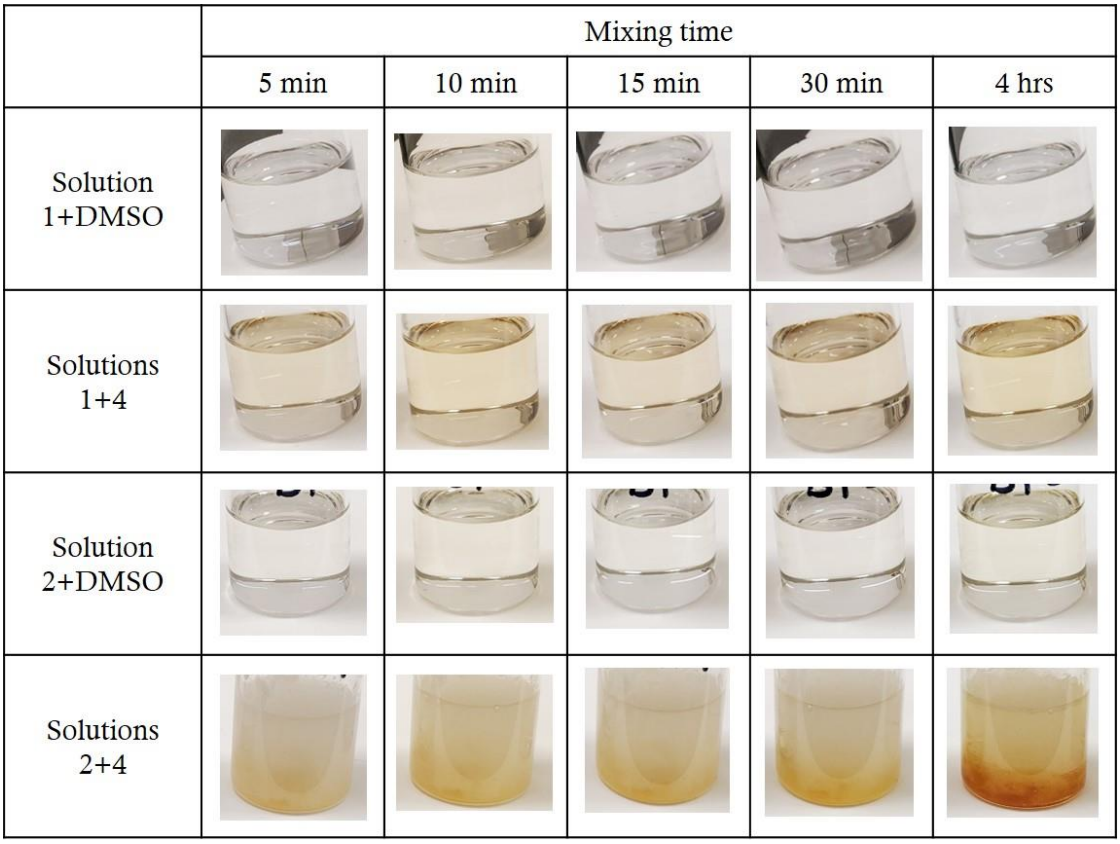

Figure A.3: Miscibility studies of TEP, PEI, DMSO, and BCAH as a function of time

TEP/PEI solution producing a homogeneous and transparent solution. The homogeneity of the solution was expected based off PEI's solubility in both DMSO and TEP at 80 ºC. The fourth row depicts the outcome of adding a fully dissolved DMSO/BCAH solution to a TEP/PEI solution and mixing the resulting solution rapidly. A white precipitate immediately formed upon mixing and over the course of 4 hours turned a light brown. The formation of the precipitate was attributed to an interaction between PEI and BCAH, but there was initially some debate whether the interaction arose from the chemical reaction of the two species or the protonation of PEI. Due to the speed of the precipitation, it was concluded that PEI protonation and its subsequent phase separation from TEP was responsible.

The last set of miscibility experiments investigated the behavior of PVDF dissolved in TEP with different concentrations of DMSO and BCAH. The first row of Figure A.4 shows the solutions after adding DMSO/BCAH and mixing the solution for 30 seconds by

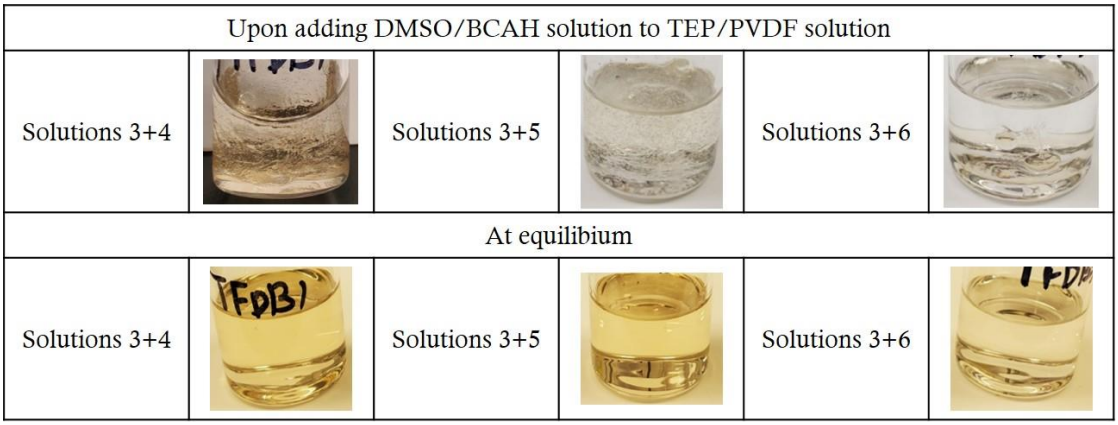

Figure A.4: Vial experiments testing miscibility of DMSO/BCAH solution in TEP/PVDF

holding the vial at a 45º angle and rotating it slowly. Due to the viscosity of the TEP/PVDF solution, the solutions were not homogeneous with visible gradients even after mixing for 30 seconds. The solutions were then incubated at 80 ºC for 1 hour after which they were homogeneous and colored, with the color intensity correlating to the concentration of DMSO/BCAH added. The homogeneity of the solutions was a bit surprising, because it was expected that PVDF would have limited compatibility with the charged BCAH. However, the pictures in Figure A.4 show no signs of cloudiness, droplets, or layer formation indicating that in the absence of PEI there is no driver for phase separation under the experimental conditions outlined in chapter 3.

Reaction Kinetics

Figure A.5a shows time stamp images of mixtures prepared by dropwise addition of different concentrations of DMSO/BCAH to TEP/PEI solutions. Adding the DMSO/BCAH solution dropwise avoids the formation of the precipitate seen in Figure A.3 and instead produce a second phase that settles to the bottom of the vial (Fig. A.5b). Initially the denser phase is comprised of “pillows” of DMSO/BCAH that touch, but do not join together. This phenomenon is especially clear at lower DMSO/BCAH concentrations that allow for a “monolayer” of pillows to form. Indeed, the monolayer is still visible after 10 minutes in Figure A.5c where there are visible boundary lines that correspond to the pillows touching

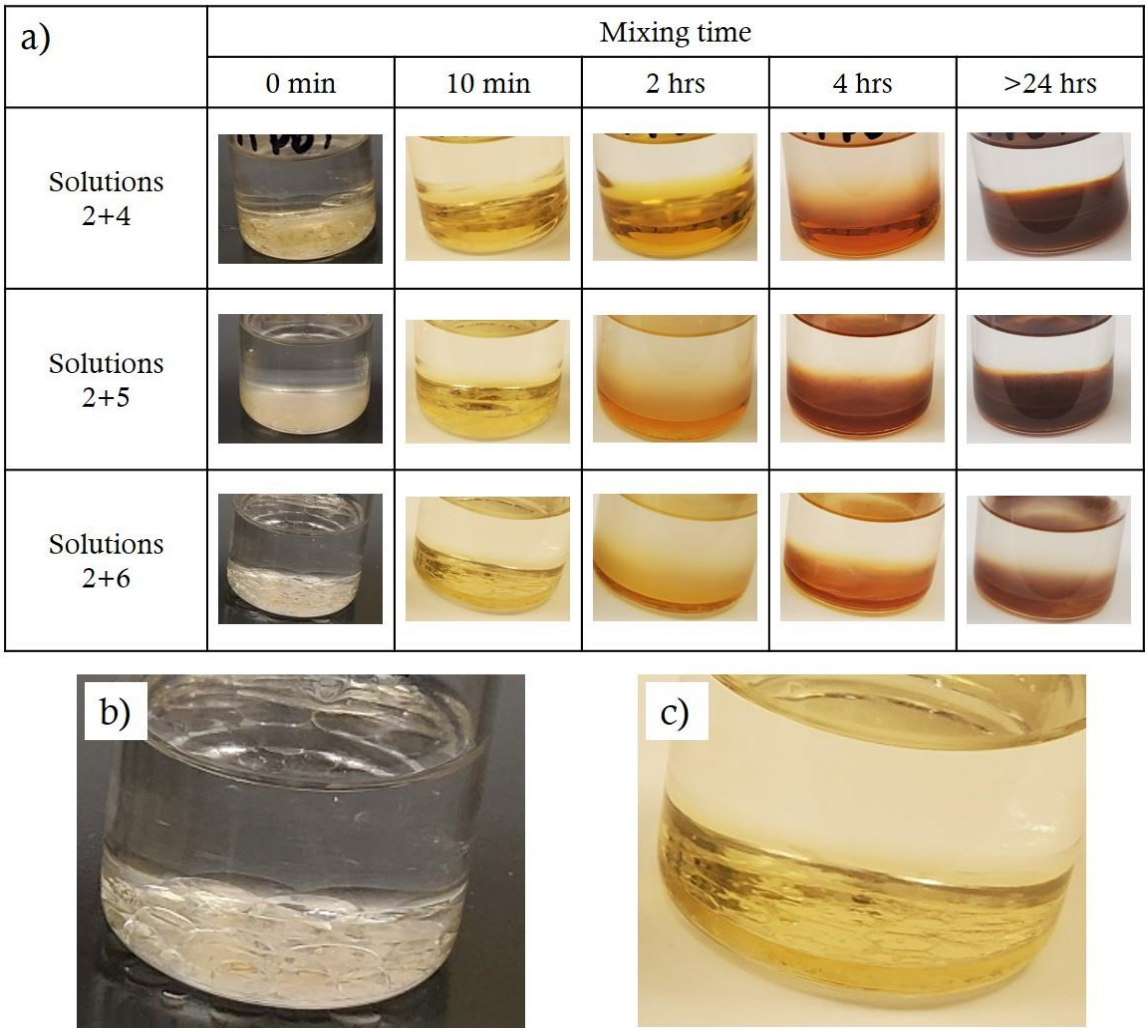

Figure A.5: Reaction kinetic study looking at a) behavior over time of TEP/PEI solutions when DMSO/BCAH solution is added slowly dropwise, b) zoomed in image of solutions 2+6 at 0 min, and c) zoomed in image of solutions 2+6 at 10 min

each other but not blending together into one phase. At higher DMSO/BCAH concentrations the pillows end up piling on top of each other and it is difficult to confirm that the pillows on the bottom do not coalesce after being cut-off from the TEP/PEI solution. The bottom phase continues to change color starting at yellow when t<2 hours, turning to orange-brown for t = 2-4 hours, and finally reaching dark brown at t>24 hours. The continuous color change in the bottom phase and the cloudiness in the top phase are indicative of an ongoing chemical reaction between PEI and BCAH.

Figure A.6 displays a set of vial experiments used to develop a better understanding of the reaction kinetics when using ECH as the crosslinker. The two reactive ends of ECH compromise an epoxide group and a halide group. Two homofunctional crosslinkers, Bis(2-chloroethyl) ether (HH) and 1,4-Butanediol diglycidyl ether (EE), were chosen to model the halide group and epoxide group respectively. To each TEP/PEI solution was added 6.9 mmols of the corresponding crosslinker. The resulting solution was mixed manually prior to placing it on the hotplate at 80 ºC. Within the first five minutes, the HH solution turned cloudy. The ECH solution then turned cloudy between 5 and 10 minutes indicating that amine-halide reaction was responsible for the solution turning cloudy. The cloudiness was ascribed to HCl produced by the amine-halide reaction protonating PEI, which induces a phase separation between the charged PEI and TEP. The HH and ECH solutions began to develop a solid precipitate along the bottom of the vial at 15 minutes, but both solutions remained cloudy with no discernable change in their viscosity over the course of the entire experiment. In contrast, the EE solution that was probing the epoxide amine reaction remained clear with no detectable changes in viscosity over the first 2 hours. Then at 2 hours and 15 minutes the viscosity of the solution slowly started increasing. At 2 hours and 25 minutes the EE solution started to turn cloudy and viscosity started increasing rapidly over

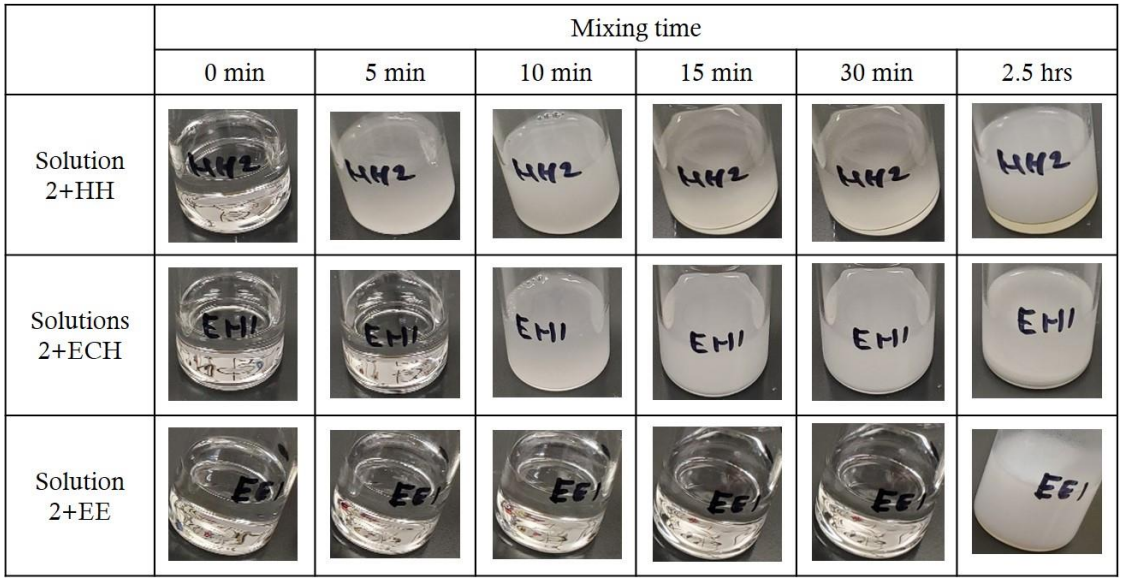

Figure A.6: Probing reaction kinetics of ECH using a molecule with two chloride groups Bis(2-chloroethyl) ether (HH) and a molecule with two epoxide groups 1,4-Butanediol diglycidyl ether (EE). Monitoring cloudiness and viscosity over time.

the course of 5 minutes. At 2 hours and 30 minutes, the EE solution was completely opaque and had gelled to such an extent that it no longer flowed under the influence of gravity. This experiment seems to indicate that although the epoxide reaction may reach completion faster, the governing influence on particle formation are the interactions arising from the halide reaction.

To estimate the extent of reaction when the solutions in Figure A.6 turn cloudy, a TEP/PEI solution at the same concentrations was titrated with 0.12 M HCl in TEP. The HCl was added in aliquots of 83.3 µL corresponding to adding 0.01 mmols of HCl per aliquot. After each aliquot the solution was gently mixed and then placed back on the hot plate to be incubated at 80 ºC. As soon as the solution turned transparent, another aliquot of 0.12 M HCl was added to the vial. This was repeated 6 times for a total of 7 aliquots added to the vial. After the 7th aliquot the solution remained cloudy for more than 10 minutes on the hot plate (Fig. A.7), so it was concluded that the 7th aliquot corresponded to the extent of reaction at 5 minutes when using HH and 10 minutes when ECH is the crosslinker. The 7 aliquots added a total of 0.07 mmols of HCl to the TEP/PEI solution. It is quite interesting that such low concentrations of HCl drive the solution to phase separate, especially considering that concentrated HCl is added to the casting solution before the crosslinker is during a typical membrane fabrication. Based off the observations here, it seems quite likely that the addition of a "catalytic" amount of HCl influences particle formation. In addition, after 24 hours at 80 ºC the titrated solution had once again turned transparent, so another 13 aliquots of 0.12 M HCl were added to the vial and the resulting solution was incubated on the hot plate for 48 hours. After two days the solution had partially separated into two phases seen in the fifth

	mmoles HCl added				
	0	0.01 – just added	0.01 - equilibtrated	0.07	0.2 – after 2 days
Solution 2+HCl		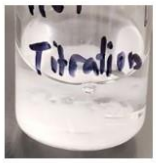	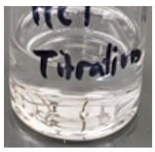	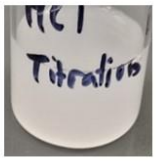	

Figure A.7: Titration of TEP/PEI solution with 0.12 M HCl in TEP

column of Figure A.7 as a yellowish viscous liquid at the bottom of the vial and a semi-cloudy clear liquid.

In regards to the extent of reaction, for every chloride on an ECH or HH molecule that reacts with a primary or secondary amine an HCl molecule is produced. ECH only has one chloride, therefore the 0.07 mmols of HCl added in the titration is equivalent to 0.07 mmols of ECH, or ~1% of the total ECH, having reacted giving an extent of reaction of 0.07 mmols. Each HH has two chloride groups, therefore the titrated 0.07 mmols of HCl results in an extent of reaction equal to 0.035 mmols or 0.05% of the total amount of HH.

A.2 Swelling of polymer matrix in water

Figure A.8 depicts the effects of PEI swelling on one of the polymeric controls from chapter 4. The area of the membrane immediately following casting and after the incubation in the IPA coagulation bath was constant. In contrast, following the membranes incubation in water the area of the polymer matrix had increased by 50%. The increase in area stems from the swelling of the PEI microgels in the presence of water. The extent of swelling achieved by the PEI microgels is determined by the crosslink density and crosslinker chemistry. At lower crosslink densities the gel has more degrees of freedom enabling it to expand and fill the available volume and in some cases even change the morphology of the surrounding material to maximize swelling as seen in Figure A.8. In comparison, the crosslinker chemistry changes the hydrophilicity of the PEI microgels, which influences the extent of swelling at thermodynamic equilibrium.

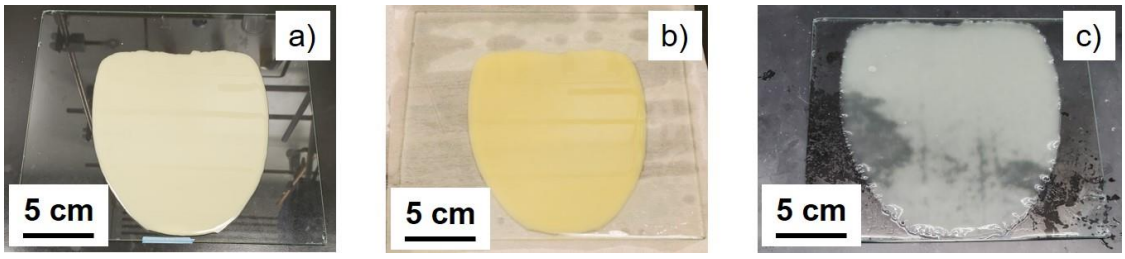

Figure A.8: Polymeric membrane prepared using BCAH at an NCD of 0.5 a) just cast, b) after 2-hour incubation in IPA, c) after overnight incubation in water.

Appendix B

FLUID CALCULATIONS FOR CHAPTER 5

B.1 Key assumptions

Several assumptions and simplifying approximations were made during the treatment of this problem including:

1. The primary pore was approximated as a perfect cylinder with a diameter equal to the average pore size from the porosimetry measurements.
2. The average primary pore size was taken for the characteristic length in calculating the Reynolds and Peclet numbers
3. Particle diffusivities were approximated to be 1 $\mu m^2/s$ and 0.1 $\mu m^2/s$, for the 0.28 μm and 2 μm particles respectively, using values reported in the literature[1].
4. It was assumed that there was no flow separation when the solution entered the sample holder due to the low Reynold's number.
5. The density and viscosity of the 35 mg/mL BSA solution was taken to be the same as water.
6. The bacteria active diffusivity was approximated to be 100 $\mu m^2/s$, based off the reported diffusivity of *E. coli* strains with similar motilities in work by Berg et al.[2]
7. It was assumed that the diffusivities in the 35 mg/mL BSA solution were the same as those in water.

B.2 Ceramic dimensions

Table B.1: Dimensions of type 1 and type 2 dendritic ceramics

Membrane structure	Type 1	Type 2
Thickness (mm)	3.2	3.2
Ceramic diameter (mm)	20	20
Primary pore 'diameter' (μm)	22	22
Primary pore Volume%	8	25
Percent porosity	76	76
Total porous volume (μL)	764	764
Total active area (mm^2)	19	60
Turn over volume (μL)	61	191
Side cavity 'diameter' (μm)	13	14

In Table B.1, the primary pore volume% is the percentage of the total porous volume that is attributed to the primary pores. The total porous volume was determined by multiplying the volume of the ceramic by the percent porosity. The total active area was calculated by multiplying the area of the ceramic by first the percent porosity and then the primary pore volume%. The turn over volume represents the total volume occupied by the primary pores and was obtained by multiplying the total porous volume by the primary pore volume%.

B.3 Particles in glycerol solution

Table B.2: Characterization of fluid flow in experiments using glycerol solution

Membrane structure	Type 1		Type 2	
Flow rate (µL/min)	10	40	10	40
Average velocity (µm/s)	8.7	35	2.8	11
Residence time (s)	367	92	1150	287
Re	1.2E-4	4.8E-4	3.9E-5	1.6E-4
Pe – 2 µm	1.9E3	7.7E3	6.1E2	2.5E3
Pe – 0.28 µm	1.9E2	7.7E2	61.4	2.5E2

The Reynolds number and Pe number were determined using equations B.1 and B.2, wherein ρ is density, U_o is average velocity, L_o is characteristic length, η is shear viscosity, and D is the diffusion constant. The density and viscosity of the glycerol solution were obtained from an online calculator[3] that based the calculation on parameterization in the literature[4]. The average velocity was calculated by dividing the volumetric flow rate by the total active area in Table B.1.

$$Re = \frac{\rho U_o L_o}{\eta} \tag{B.1}$$

$$Pe = \frac{U_o L_o}{D} \tag{B.2}$$

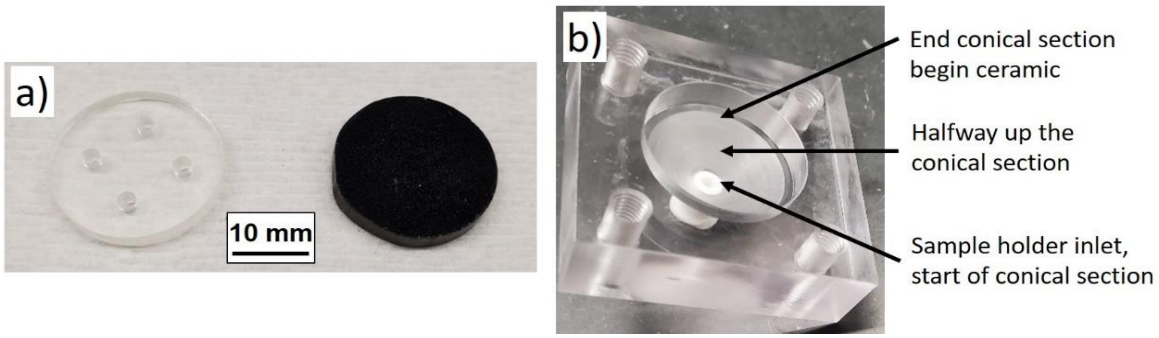

Figure B.1: Pictures of a) control and type 1 ceramic, as well as b) base of sample holder showing conical fluid expansion area.

B.4 Particles and bacteria in 35 mg/mL BSA solution

Panel a of Figure B.1 shows the control disc with 4 holes that are equidistant from the center and separated by 90º as well as a type 1 ceramic membrane. Panel b of Figure B.1 is a picture of the sample holder demonstrating the conical area placed before the ceramic in an effort to allow even distribution of the fluid to the sample. The same picture is also used to indicate the positions inside the sample holder where the fluid flow was characterized in Table B.3. A diffusivity of 0.2 $\mu m^2/s$ was used in the Pe calculation for non-motile bacteria[1] in Table B.3.

Table B.3: Characterization of fluid flow at different points in the flow-through setup at a flow rate of 50 µL/min.

	Inlet/outlet tube	Sample holder inlet	Halfway point	End of conical	Type 1 ceramic	Control
Characteristic Length (mm)	1	5	12.5	20	0.022	2.5
Active area (mm^2)	0.785	19.6	123	314	19	19
Average fluid velocity (µm/s)	1061	42.5	6.8	2.7	43.9	43.9
Re	0.42	0.21	0.085	0.054	9.6e-4	0.11
Pe – 2 µm	4.2E6	2.1E6	8.5E5	5.4E4	9.6E3	1.1E6
Pe – 0.28 µm	4.2E5	2.1E5	8.5E4	5.4E4	9.6E2	1.1E5
Pe – *E. coli*	4.2E3	2.1E3	8.5E2	5.4E2	9.6	1.1E3
Pe – non-motile bacteria	2.1E6	1.1E6	4.3E5	2.7E5	4.8E3	5.5E5

References

(1) Squires, T. M.; Quake, S. R. Microfluidics: Fluid Physics at the Nanoliter Scale. Rev. Mod. Phys. 2005, 77 (3), 977–1026. https://doi.org/10.1103/RevModPhys.77.977.

(2) Berg, H. C.; Turner, L. Chemotaxis of Bacteria in Glass Capillary Arrays. Escherichia Coli, Motility, Microchannel Plate, and Light Scattering. Biophysical Journal 1990, 58 (4), 9s19–930. https://doi.org/10.1016/S0006-3495(90)82436-X.

(3) Calculate density and viscosity of glycerol/water mixtures http://www.met.reading.ac.uk/~sws04cdw/viscosity_calc.html (accessed 2021 -08 -29).

(4) Cheng, N.-S. Formula for the Viscosity of a Glycerol−Water Mixture. Ind. Eng. Chem. Res. 2008, 47 (9), 3285–3288. https://doi.org/10.1021/ie071349z.

Appendix C

CULTURE PROTOCOL FOR *E. COLI*

The information in this Appendix is a summary of the culture protocol designed by Priya Chittur and used by Orland Bateman when preparing bacteria for the flow-through experiments in chapter 5.

C.1 Making solid media

1. This recipe is for "high salt" media.
    a. Tryptone and casein hydrolysate are interchangeable.
2. For 1L of total volume (scale as needed), measure:
    a. a) 10g casein hydrolysate
    b. 5g yeast extract
    c. 10g NaCl
    d. 15g agarose
3. Add 1L of distilled water and lightly mix.
    a. Use Milli-Q water when possible, but DI water is acceptable
4. Make sure that whatever container you're using is only ~80% full. You need free space at the top to prevent overflowing.
    a. For large volumes use a large conical flask
5. Add autoclave tape if desired. Make sure the lid is only loosely placed and not fully sealed. Your bottle will blow up otherwise.
6. Autoclave the sample at high pressure and temperature for 20 minutes
7. While waiting for the autoclave to finish, remove some petri dishes from their cover and place them out on the bench.
8. Pick up media once autoclave cycle is done
9. Once the autoclave is done, leave the media on a bench for 10-15 minutes. If you have a water bath, set it to 50-55 ºC and leave the flask/bottle in that until it reaches 55 ºC
    a. If no water bath is available, leave the media out to cool until it reaches "palm touch" heat
10. At this point, add the ampicillin.

    a. Get the ampicillin stock from the freezer and add 1000x less than the total volume.

11. Pipette 20-25 mL of the media (using large serological pipettes) into each petri dish. Place the lids very loosely on top (only half covered).
12. Once the media has been added to the petri dishes, quickly rinse out the flask before the agar solidifies.
13. Leave the petri dishes for 10-15 minutes to solidify the agar.
14. Once the agar is solidified, stack the petri dishes upside down and place them in a cover
15. Place sideways at 4C – the solid media will be good to use for a month

C.2 Making a streak plate

1. Sterilization work bench and turn on flame (using either Bunsen burner or alcohol candles)
2. Take out a plate from the fridge and leave it at 37 ºC until warm
    a. Usually takes about 30 minutes
3. Take out an *E. coli* glycerol stock solution from the -80 ºC freezer and place it in dry ice to prevent it from thawing
4. Use a sterile pipette tip to scrape off some of the frozen stock and streak it across the plate, without doubling back on areas that have already been streaked.
5. Place the now streaked plate in the incubator upside down and allow it to grow for ~24 hours without shaking until you see colonies.
6. Parafilm the plate and place at 4C to use as new "streak plate stock" for a month.

C.3 Growing bacteria culture

1. Take the streak plate out of the fridge, sanitize the workspace and any pipettes that will be used with 70% ethanol or IPA.
2. Turn on a flame close nearby the working area and leave it on while working (Bunsen burner or alcohol candles).
3. Open the bottle with the liquid LB media and pass the mouth of the bottle over the flame to generate air currents that flow out the bottle.
4. Use a serological pipette to draw about 4 ml of the liquid media and put it into a clean culture tube.
5. Flame the mouth of the liquid LB bottle again and close it.
6. Make sure to add antibiotic to your culture tube. The mWasabi expressing strain is Ampicillin resistant. You can find a 1000x Amp stock in the small freezer.
7. Add 4 uL of 1000x Amp stock for 4 mL of final liquid volume in the culture tube.
    a. Make sure to parafilm the Amp and put it away quickly to avoid degradation

8. Use a sterile pipette tip to pick up a single colony from the plate and drop it into the culture tube.
9. Place the culture tube in the shaker incubator at 37 ºC and 250 rpm for 12-16 hours.
10. Parafilm the streak plate and put it back in the 4C fridge.

C.4 Making liquid media

1. For 1L of total volume (scale as needed), measure:
    a. 10g casein hydrolysate
    b. 5g yeast extract
    c. 10g NaCl
2. Add 1L of distilled water and lightly mix.
    a. Use Milli-Q water when possible, but DI water is acceptable
3. Make sure that whatever container you're using is only ~80% full. You need free space at the top to prevent overflowing.
    a. For large volumes use a large conical flask
4. Add autoclave tape if desired. Make sure the lid is only loosely placed and not fully sealed. Your bottle will blow up otherwise.
5. Autoclave the sample at high pressure and temperature for 20 minutes
6. Once autoclave cycle is complete, store liquid media at room temperature
7. NOTE: Do NOT add antibiotic to this bottle. It reduces the life of both the media and the antibiotic. It's better to add the antibiotic to your small culture tube just before using it.